Institute of Paper Science and Technology

HIGH-INTENSITY DRYING PROCESSES - IMPULSE DRYING

MODELING OF FLUID FLOW AND HEAT TRANSFER IN A CROWN COMPENSATED IMPULSE DRYING PRESS ROLL I. THE LUBRICATION PROBLEM

Project 3595

Report 9

to

U.S. DEPARTMENT OF ENERGY

August 1994

Atlanta, Georgia

INSTITUTE OF PAPER SCIENCE AND TECHNOLOGY PURPOSE AND MISSION STATEMENT

The Institute of Paper Science and Technology is a unique organization whose charitable, educational, and scientific purpose evolves from the singular relationship between the Institute and the pulp and paper industry which has existed since 1929. The purpose of the Institute is fulfilled through three missions, which are:

- to provide high quality students with a multidisciplinary graduate educational experience which is of the highest standard of excellence recognized by the national academic community and which enables them to perform to their maximum potential in a society with a technological base; and
- to sustain an international position of leadership in dynamic scientific research which is participated in by both students and faculty and which is focused on areas of significance to the pulp and paper industry; and
- to contribute to the economic and technical well-being of the nation through innovative educational, informational, and technical services.

ACCREDITATION

The Institute of Paper Science and Technology is accredited by the Commission on Colleges of the Southern Association of Colleges and Schools to award the Master of Science and Doctor of Philosophy degrees.

DOE/CE/40738 - T8
( )
Distribution Category UC-310

HIGH-INTENSITY DRYING PROCESSES - IMPULSE DRYING

Modeling of Fluid Flow and Heat Transfer in a Crown Compensated Impulse Drying Press Roll I. The Lubrication Problem

REPORT 9

By

David Orloff, Barry Hojjatie, and Frederick Bloom

August 1994

Work performed under Contract DE-FG02-85CE40738

The Institute of Paper Science and Technology
Atlanta, Georgia

Project No. 3595

Prepared for:

Stanley F. Sobczynski
Program Manager, EE-233, DOE/OIP
U.S. Department of Energy
Office of Industrial Programs
Conservation and Renewable Energy
Washington, DC 20585

TABLE OF CONTENTS

SUMMARY

We have analyzed the lubrication problem which arises in modeling impulse drying employing a crown compensated roll; the geometry for the associated steady flow problem is constructed and expressions are derived for the relevant velocity fields, mass flow rates, and normal and tangential forces acting on both the bottom surface of an internal hydrostatic shoe and the inside surface of the CC roll.

The bottom surface of the shoe and the inside surface of the roll form a curvilinear channel and are assumed to lie on circles of either equal or different radii; the coordinates of the center of the circle, on which the arc describing the bottom surface of the shoe lies, can be used, in conjunction with the angular "rotation" ψ of the shoe, to define a base lubrication thickness d_0 for an approximate planar-walled channel in which the lubrication problem is posed; the parameters d_0 and ψ are then determined by the solution of a set of equilibrium equations, which for the present problem will consist of a coupled set of three nonlinear, transcendental, algebraic equations. Parameters entering into the equilibrium equations include geometrical design parameters such as the radii of both the shoe and the roll, and the angular opening of the shoe, as well as physical parameters such as the load per unit width of the shoe, exerted along the top surface of the shoe, and the tangential speed of the CC roll which rotates counterclockwise.

The equilibrium equations are, themselves, obtained by balancing horizontal and vertical components of all forces acting on the shoe (including the tangential and normal forces exerted by the lubricating oil on the upper planar walled surface of the convergent wedge-shaped channel which approximates the actual curvilinear channel in a precise geometric manner) and by imposing, as well, balance of moments for all forces.

The lubrication channel is fed by two sets of capillaries which traverse the shoe and enter each side of the channel through recesses cut out of the bottom of the shoe; lubricating oil is

injected through the capillaries on each side of the shoe, to the channel, and the shoe subsequently turns in the clockwise direction as a consequence of the viscosity of the oil, the motion of the roll, and the required balance of forces and moments.

The base thickness d_0 of the (approximate) channel – equivalently, the coordinates of the center of that circle on which the arc describing the bottom surface of the shoe lies – and the angular "rotation" ψ of the shoe, not only serve to completely determine the equilibrium position of the shoe, once the load on the shoe and the speed of the roll are given, but also determine all pressure and velocity fields in the channel and, therefore, all normal and tangential forces which act on the bottom surface of the shoe.

Numerical solutions of the algebraic equilibrium equations have been carried out both for a "small" shoe/roll configuration in which the shoe radius is slightly smaller than the inner roll radius, and for a "large" shoe/roll configuration in which the two radii are machined so as to be approximately equal; the results of these numerical studies are reported in §4. The numerical studies, which are based on the analytical model constructed in this report, indicate that the model can be used effectively to study the variation in channel thickness, deflection of the shoe, net mass flow rate, pressure distributions, and the power required to operate the roll either in terms of the load F (on the shoe) for a fixed tangential speed s (of the roll, where s refers to the speed of the inner surface of the roll) or in terms of s for fixed F; the major results that can be abstracted are as follows:

(i) For the "small" shoe/roll configuration it follows that film thicknesses increase at fixed load with increasing roll speed and at a fixed speed the film thicknesses decrease with increasing load; but, for the "large" shoe/roll configuration we observe that the leading edge thicknesses increase while trailing edge thicknesses decrease with increasing speed at a fixed load and with decreasing loads at a fixed speed.

(ii) The clockwise deflection of the shoe increases with increasing speed at each fixed load and decreases as the load increases at any fixed speed.

(iii) For the small roll/shoe configuration, at a fixed load, the mass flow rate in the entire channel increases with increasing roll speed. The increase being nearly linear at both high and low loads; also for a fixed speed, the net mass flow rate increases with increasing load. For the large roll/shoe configuration, the mass flow rate is relatively insensitive to changes in speed for a fixed load but increases linearly with increasing load at fixed speeds.

(iv) For the small roll/shoe configuration, at a given applied load the mechanical power required to operate the roll increases with roll speed, with the increases being larger and nonlinear at high loads the same being true for increasing load at fixed speeds. However, for the large roll/shoe configuration the power required to operate the roll is relatively insensitive to increases in load at fixed speeds but the power increases nonlinearly with increasing speed at a fixed load.

(v) Over a wide range of applied loads and roll speeds, the pressure distribution along the inside surface of the roll, in the lubrication channel, is constant in the vicinity of each of the two respective sets of recesses, where lubricant enters the channel, and falls off monotonically as one moves from each recess towards the end of the subchannel fed by that recess.

In view of the very prominent fashion that design parameters such as the radii of the shoe and roll and the angular opening of the shoe (as well as physical parameters such as the density and viscosity of the lubricating oil) enter into the expressions for d_0 and ψ, and, thus, into the equilibrium equations, the model can be used to predict, for given applied loads and roll speeds, the effect that specific design changes would have on lubricant thickness, pressure distributions, mass flow rates, lubricant velocity fields, and the mechanical power required to operate the roll; the mathematical model, thus, presents the engineer with what is anticipated to be an extremely effective tool for optimizing specific design factors in the construction of the shoe/roll configuration in impulse drying.

OVERVIEW AND OBJECTIVES

Ongoing research at the Institute of Paper Science and Technology (IPST) has demonstrated the feasibility of using impulse drying to increase productivity, quality and energy efficiency of Linerboard and other heavy weight grades of paper. Plans are in progress for commercializing impulse drying technology through a joint venture between the Institute, Beloit Corporation and the Union Camp Corporation. That commercialization would be supported in part by the U.S. Department of Energy's Office of Industrial Programs.

Much of the Institute's previous research in impulse drying has focused on understanding the details of the process and in demonstrating the benefits of the process to paper machine productivity, physical property improvement and energy savings. With the start of the commercialization phase of the effort, the Institute has additionally focused on mechanical design and materials issues that would increase the likelihood of successful implementation of impulse drying technology.

In 1994 that effort will include the construction and operation of a high speed test stand for the evaluation of the long term durability of various impulse drying press roll coatings. The test stand will be operated at commercial paper machine speeds of 2500 ft/min. It will consist of a roll shell coated with three or more test materials, an induction heating system, and a continuous wet felt that can be loaded against the roll surface to simulate impulse drying. The roll shell will be monitored to detect the onset of roll coating failure and to determine the state of stress at key locations in the roll and roll coating. The test stand will be used to evaluate the long term durability of these roll coatings under commercial impulse drying conditions.

Also during 1994/95 the Institute will develop a finite-element model of a crown-compensated impulse drying press roll. The model will be capable of predicting the temperature and state of stress at any location within the roll as a function of impulse drying operating conditions and roll composition. The results of the model will be compared to the experimental results from the high speed test stand and used to optimize roll design for maximum energy efficiency and component durability.

As a first step in the development of the finite element model, work was carried out in 1994 to determine the stress and heat transfer boundary conditions that would be imposed on a crown-controlled impulse drying press roll. In particular, the present research effort was directed to determining the pressure distribution and heat flux at the interface between the inside surface of the press roll and the internal hydrostatic shoe. This report describes the lubrication part of that problem. A future report will document the heat transfer part of the problem.

In the lubrication work, we are able to predict the velocity field in the lubricating oil between the hydrostatic shoe and the roll shell. Through these calculations, we are then able to predict oil flow rates, power consumption and pressure distribution at the interface.

1. INTRODUCTION

Although energy intensive evaporative drying is currently used to dry paper, research has demonstrated that a significant savings in energy could be realized by implementing the newer impulse drying technology. In figure 1, which is taken from Orloff, Jones and Phelan [1], we show a crown-compensated (CC) extended-nip press which is configured with a ceramic coated press roll. The roll (see figures 1, 2) revolves at high speed, counterclockwise, and is loaded, in the impulse drying mode, by the internal hydrostatic support element. Oil is injected through the hydrostatic support element, i.e., the shoe, so as to produce an oil film between the bottom of the shoe and the inside surface of the roll which provides lubrication and, also, acts as a heat sink for heat lost to the interior of the roll. In the overall process, wet paper sheets transported on felt enter an extended nip at point A, in figure 1, and leave the nip at point C, while the roll itself is heated in a zone from point D to point E so as to achieve a prescribed roll surface temperature at the entrance to the nip at point A.

In this report and the companion report [2] we consider the problem of fluid flow and heat transfer in the channel formed by the (curved) bottom of the internal shoe and the inside surface of the roll. It will be assumed that the arcs describing the bottom of the shoe and the inside surface of the roll lie on circles of radii R_s and R, respectively, where we may have either $R_s=R$ or $R_s<R$. The actual channel, with curved walls, will be approximated by a planar walled convergent channel or wedge. The planar walled channel described above will be formed by inscribing appropriate secant lines within the circles describing the bottom of the shoe and the inside of the roll. A parallel-wall approximation for such a channel had been studied earlier by Orloff [3].

The internal shoe, which is sketched in figure 3, is loaded by an external force F, measured per unit width of the shoe, so that the net load on the shoe is just F times the width w_{sh} of the shoe. The other key variables which enter the mathematical model are p_{sh} (the pressure at the top of the shoe), p_{exit} (the pressure at which the lubricating oil exits each of the two subchannels - for our purposes in this report we will take $p_{exit} = p_{atm}$ (i.e., atmospheric pressure) $\tilde{R}_{eff}$ and $\tilde{l}_{eff}$ (respectively, the effective radius and length of each of the capillaries through which the lubricating oil enters the channel formed by the bottom surface of the shoe and the inside surface of the roll; i.e., see figure 3), Φ (the angle subtended by radii, in the circle describing the shoe, through the endpoints of the arc coincident with the bottom of the shoe), s (the linear speed of the inner surface of the roll, which is assumed to be rotating counterclockwise) and μ and ρ (respectively, the viscosity and density of the lubricating oil). In this initial model it will be assumed that the viscosity μ is constant, but, in work to follow, we must take into account the fact that μ varies with temperature, albeit linearly over the range of temperatures at which it is anticipated that the roll will be operated.

As a consequence of the loading of the internal shoe, the pressure difference $p_{sh} - p_{exit}$, and the counterclockwise motion of the roll, the shoe will be forced downward and will deflect clockwise once the shaft of the shoe has been displaced to the right and the middle rib (see figure 4) at the top of this shaft comes into contact with the wall of the confinement shaft. We note, for future reference, the rubber seals which are present on both sides of the top of the shaft (figures 2 and 4); the primary function of these seals is to prevent (downward) leakage of the pressurized oil at the top of the shaft of the shoe. However, during the motion of the internal hydrostatic shoe, the oil seals which are positioned along the shaft of the shoe are both stretched and compressed and, thus, function as mechanical springs (attached to the shaft of the internal shoe) which constrain the deflection of the shoe; this issue will be dealt with in §3 when we discuss the equilibrium equations.

Concerning the geometry employed in the model, the point $(0, R)$ in figure 5 is the location of the center of the circle describing the inside surface of the roll so that $(0, 0)$ is the point of contact (tangency) between the roll and the paper. At a given tangential speed s of the roll and a given load F on the shoe, the center of the circle describing the bottom surface of the shoe is located at the point $(a, R+b)$ where a, b are to be determined by a set of coupled, nonlinear equilibrium equations. The points E and B lie, respectively, at the centers of the top of the shaft of the shoe and the arc describing the bottom surface of the shoe. The line segments from $(a, R+b)$ to A, B, and C are radii of the shoe of length $R_s \leq R$, while ψ is always the angle between the center line of the shoe (through E, B) and that radius of the circle describing the roll which goes through $(0, R)$ and $(0, 0)$. The lubrication channel (or bearing) is formed by the arcs ABC and $A'B'C'$ and a base lubrication thickness may be measured along the segment BB'. The approximating planar-walled channel (or wedge) will be constructed by using the secant lines through the points A, C and A', C'. There is a slight tapering of the shoe near the endpoints located at A and C which has not been taken into account in the model which is formulated in this report.

When the upper right hand corner of the shaft of the shoe makes contact with the confinement wall (by virtue of the 2nd or middle rib at the top of the shaft of the shoe coming into contact with that wall) the shoe will turn slightly in the clockwise direction (see figure 6) and the point of contact between the rib on the shaft of the shoe and the confinement wall (labeled as point PV in figure 6) will slide up and down that wall without friction. As shown in figure 6 the rib in question protrudes a distance β_r from the shaft of the shoe and is located a distance α_r down from the top of the shaft. In our work in §2 we locate the position of the pivot point PV and indicate that the parameter a (figure 5) is determined entirely in terms of the angle ψ and given geometrical quantities that are associated with the design of the shoe. Also, in the model that is constructed in §2 there will be two primary (independent) variables: the angle ψ and either a base lubrication thickness d_0 (essentially the length of the line segment BB′ in figure 5) or the value of the Y coordinate of the point which locates the center of the circle on which the arc that describes the bottom surface of the shoe lies, i.e. the value of the parameter b (figure 5).

The variables ψ and b (or d_0) must be determined by the physics of the problem, i.e., by enforcing equilibria of forces in both the vertical and horizontal directions as well as balance of moments of forces acting on the internal hydrostatic shoe; the resulting equilibrium equations in §3 turn out to be a system of coupled, nonlinear, transcendental algebraic equations which can be numerically solved by an iterative procedure. Once ψ and d_0 have been determined it is then possible to compute all the geometrical quantities which are needed in order to fix the size and shape of the approximate wedge-shaped channel as well as the pressures $\tilde{p}_R$ and $\tilde{p}_L$ in each of the two sets of recesses, the mass flow rates $\dot{m}_L$ and $\dot{m}_L$ in each subchannel, and the explicit forms of all velocity fields in each of the two subchannels. The velocity fields are two-dimensional and are obtained by imposing the standard lubrication theory assumption (e.g., [4], [5]) of pseudo-plane Couette flow. Expressions for the tangential and normal forces exerted by the lubricating oil both on the bottom surface of the shoe as well as on the inside surface of the roll are reported in the technical summary (Appendix II); these results may, in turn, be used to compute the net drag force acting on the roll and, thus, the work which must be expended to operate the CC roll.

Inasmuch as the equilibrium equations of §3 yield implicit relations for ψ and b of the form

$$\begin{cases} \psi = \psi(F, p_{sh} - p_{exit}, s, R, \phi, R_s, \tilde{R}_{eff}, \tilde{l}_{eff}, \mu, \rho) \\ b = b(F, p_{sh} - p_{exit}, s, R, \phi, R_s, \tilde{R}_{eff}, \tilde{l}_{eff}, \mu, \rho) \end{cases}$$

one may, in principle, study the effect of holding all variables in the parameter space $\mathcal{P}$

$$\mathcal{P} = \{F, p_{sh} - p_{exit}, s, R, \phi, R_s, \tilde{R}_{eff}, \tilde{l}_{eff}, \mu, \rho\}$$

fixed except for one, say, s in order to study how ψ and b vary with the speed of the roll; this same procedure would then yield valuable information on how, e.g., the drag on the roll varies with s if all other elements in the parameter space $\mathcal{P}$ are frozen and one could even consider holding all parameters fixed except for two, e.g., s and F, and repeating the procedure described above. Some numerical results in this direction are present in §4.

In Appendix V we present some results for the 'small' roll-shoe configuration which are based on new information from the Beloit Corporation regarding certain dimensions of the roll and the shoe that were used to produce the experimental data employed in this report. This updated information was not available throughout most of the period during which the research which led to this report was in progress. In general, the use of this updated information in the numerical model produces much better agreement with the experimental data, for the few loads and speeds tested.

In a companion paper [2] we show that having determined ψ and b (or d_0) for a fixed set of values in the parameter space $\mathcal{P}$, so that all velocity fields may be explicitly computed, we are led to a pair of well-posed boundary value problems for the steady-state temperature distributions in each of the two subchannels; the solution of these boundary-value problems then enables us to determine the net heat flow from the roll to the lubricating oil, the net heat flow from the oil to the shoe, and the net heat convected away by the fluid, in terms of the variables in the parameter space.

2 THE GEOMETRICAL MODEL FOR THE LUBRICATION CHANNEL AND THE MOTION OF THE INTERNAL SHOE.

In this section, we begin the work of modeling the lubrication problem occurring in the channel formed by the bottom surface of the internal shoe and the inside surface of the rotating roll; here, and in §3, we will try to hold the density of technical details and equations as low as possible by making ample use of the nomenclature (appendix I), and the technical summary (appendix II), with equations in the technical summary listed as (S1), (S2), etc. We will also refer, quite often, to the figures in appendix III.

As a consequence of the load F applied to the top of the shoe and the tangential speed s of the roll, which turns counterclockwise, the shaft of the shoe will shift to the right until the middle rib at the top of the shaft of the shoe hits the wall of the confinement shaft (figure 4); thereafter, the shoe will turn clockwise through an angle ψ (figure 5) and, also, execute a motion, normal to the plane of the incoming paper, until it achieves an equilibrium position. The equilibrium position may be completely specified by the two variables ψ and $d_0 = \overline{BB'}$ (figure 5).

In lieu of considering the motion of the lubricant in the channel formed by the curved surfaces at the bottom of the shoe and the inside of the roll, we consider the problem of steady flow in the channel formed by the secant line segments (see figure 5) $\overline{AB}, \overline{A'B'}$ and $\overline{BC}, \overline{B'C'}$; the task then is to specify the geometry of this approximate channel in terms of R, R_s, φ, ψ, and d_0, φ being the half-angular opening of the shoe (figure 5).

The arc $\widehat{ABC}$ describing the bottom surface of the shoe lies on the circle $(x-a)^2 + (y-(R+b))^2 = R_s^2$ (figure 5), while the arc $\widehat{A'B'C'}$, which describes the inside surface of the roll, lies on the circle $x^2 + (y-R)^2 = R^2$; either $R = R_s$ or $R > R_s$ and the coordinates of the point $(a, R+b)$ must be determined by the solution of the set of equilibrium equations for each fixed pair (F, s).

To specify the geometry of the approximate planar-walled channel, we must determine the coordinates of the points A, B, C and A', B', C'. To delineate the equilibrium equations, we must also specify the coordinates of the point PV in figures 6 and 7; while the definitions of all the geometric and design variables in figures 6 and 7 should be obvious from the figures themselves, all pertinent variables are also carefully defined in the nomenclature (Appendix I). It may be shown that the equation of the line through points Q, Q^* (figure 7) has the form:

$$y = cot\psi[x - (a + \frac{\hat{l}}{\cos\psi})] + R + b \tag{2.1}$$

while that of the line through $(a, R + b)$ and Q is

$$y = -\tan(\delta + \psi)[x - a] + R + b \tag{2.2}$$

Then (2.1), (2.2) yield for x_Q, the x-coordinate of point Q, figure 7,

$$x_Q = a + \hat{l}/\{\cos\psi[1 + \tan\psi \cdot \tan(\delta + \psi)]\} \tag{2.3}$$

while from figure 7, togther with figure 6,

$$x_Q = l^* - (\beta_r \cos\psi - \alpha_r \sin\psi) \tag{2.4}$$

If we combine (2.3) and (2.4) we are led to an expression for a of the form

$$a = a(\psi; \hat{l}, l^*, \alpha_r, \beta_r, \delta), \tag{2.5}$$

i.e. for a given set of design variables the coordinate a is a function of the angle ψ; the precise relation for a in terms of ψ is given by (S1). For $\psi \approx 0$,

$$a \simeq (l^* - \hat{l}) - \beta_r \cos\psi + \alpha_r \sin\psi \tag{2.6}$$

By virtue of figure 7, $x_{Q'} = x_{PV} = l^*$, while from figure 6

$$y_{PV} = y_Q - (\alpha_r \cos\psi + \beta_r \sin\psi) \tag{2.7}$$

The number y_Q may be computed using (2.2) and (2.3) and then y_{PV} is given by (2.7); the exact expression for y_{PV} is given in (S2).

The points A, B, C and A', B', C' are, by virtue of figure 5, the points of intersection of the lines $L_{\mathcal{L}}, L_C$ and L_R with the arcs $\widehat{ABC}$ and $\widehat{A'B'C'}$ describing, respectively, the bottom surface of the shoe and the inside surface of the roll. It is not difficult to show that these lines have the form:

$$\left\{\begin{array}{lll} L_{\mathcal{L}}: & y = m_{\mathcal{L}}(x-a) + (R+b); & m_{\mathcal{L}} = \cot(\varphi + \psi) \qquad (2.8a) \\ L_C: & y = m_C(x-a) + (R+b); & m_C = \cot\psi \qquad (2.8b) \\ L_R: & y = m_R(x-a) + (R+B); & m_R = \cot(\psi - \varphi) \qquad (2.8c) \end{array}\right.$$

Combining (2.8a,b,c) with the equations of the circles on which the arcs $\widehat{ABC}$ and $\widehat{A'B'C'}$ lie, we are led to the expressions in (S3), (S4), and (S6) for the coordinates of the points A, B, C, and A', B', C'. A base lubrication thickness d_0 may then be defined by (figure 5)

$$d_0 = \overline{BB'} \equiv \sqrt{(x_B - x_{B'})^2 + (y_B - y_{B'})^2} \tag{2.9}$$

Referring to the sketch in figure 8, we have two choices: we may either stay with our initial premise of using an approximation based on the line segments $\overline{AB}$ and $\overline{BC}$ for the bottom surface of the shoe, and $\overline{A'B'}, \overline{B'C'}$ for the inside surface of the roll or we may start by taking the somewhat simpler route of using $\overline{AC}$ to approximate the (curved) bottom surface of the shoe and $\overline{A'C'}$ to approximate the (curved) inside surface of the roll; for ψ small it is expected that there will be only small quantitative differences between the two approaches and, thus, in this first model we opt for the latter approximation.

If θ_1 = the angle between the positive x-axis and the direction of $\overline{A'C'}$ while θ_2 = the angle between the positive x-axis and the direction of $\overline{AC}$ then

$$\begin{cases} m_u = \text{slope}\overline{AC} \equiv \tan\theta_2 \\ m_l = \text{slope}\overline{A'C'} \equiv \tan\theta_1 \end{cases} \tag{2.10}$$

In all cases of physical interest we will have $\theta_1 < 0, \theta_2 < 0$ with $|\theta_2| > |\theta_1|$ so that

$$\beta \equiv \theta_1 - \theta_2 = |\theta_2| - |\theta_1| > 0 \tag{2.11}$$

Computing $\tan\theta_1 = (y_{C'} - y_{A'})/(x_{C'} - x_{A'})$ and $\tan\theta_2 = (y_C - y_A)/(x_C - x_A)$ we are led to the expression in (S3) for θ_1 while it easily follows from (S4) that $\theta_2 = -\psi$. We then have, by (2.11), that

$$\beta = \tan^{-1}\left[\frac{\tan\theta_1 + \tan\psi}{1 - \tan\theta_1 \tan\psi}\right] \tag{2.12}$$

We now refer back to figure 8 and consider the wedge shaped quadrilateral formed by the points A', A, C, and C'; if we rotate this quadrilateral by rotating the line through $\overline{A'C'}$ a total of θ_1° counterclockwise, until it is coincident with the direction of the positive x-axis, we obtain the approximating lubrication channel depicted in figure 9 where the 'base' lubrication thickness has been taken to be d_0 as given by (2.9).

If we consider separately the left and right subchannels associated with the wedge-shaped channel depicted in figure 9, then we have the situation detailed in figures 10a,b. In figure

10a, L_c is the (approximate) distance from point B, figure 5, to the beginning of the recess on the right-hand side of the shoe, L_{rec} the distance to the end of this recess, as measured along the projection of the bottom surface of the shoe, and $L_T = R_s\varphi$ the distance to the end of the shoe; the quantities l_c, l_β, and L_β are the projections, respectively, of L_c, L_{rec}, and L_T on the direction of the line through $\overline{B'C'}$. In figure 10b, so as to not have to deal with negative values of x, we show the left-hand subchannel as rotated π radians about the vertical axis in the plane. Thus the thickness in the right-hand subchannel is given by

$$d_R(x) = d_0 - x\tan\beta, 0 \leq x \leq L_\beta \tag{2.13}$$

while that in the left-hand subchannel is given by

$$d_{\mathcal{L}}(x) = d_0 + x\tan\beta, 0 \leq x \leq L_\beta \tag{2.14}$$

3 PHYSICAL MODELING OF THE LUBRICATION PROBLEM: THE EQUILIBRIUM EQUATIONS.

We begin by analyzing the steady flow problem in the right-hand subchannel (figure 10a). Letting $\bar{p}_R(x), l_\beta \leq x \leq L_\beta$ denote the pressure in this subchannel to the right of the recesses and $\bar{u}_R(x,y)$ the corresponding velocity field, our basic assumption is that of standard lubrication theory [4],[5], namely, in a neighborhood of any point $x, l_\beta \leq x \leq L_\beta$,

$$\bar{u}_R(x,y) = \frac{1}{2\mu}\bar{C}_R(x)y(d_R(x)-y) + s(1-yd_R^{-1}(x)) \tag{3.1}$$

with $\bar{C}_R(x) = -\bar{p}_{R'}(x)$ the negative of the pressure gradient. The velocity field $\bar{u}_R(x,y)$ satisfies $\bar{u}_R(x,0) = s, \bar{u}_R(x, d_R(x)) = 0$ for all $x, l_\beta \leq x \leq L_\beta$. Based on (3.1), the mass flow rate/unit depth in the right-hand channel is

$$\dot{m}_R = \rho\int_0^{d_R(x)} \bar{u}_R(x,y)dy \equiv \frac{1}{12\mu}\rho\bar{C}_R(x)d_R^3(x) + \frac{1}{2}\rho s d_R(x) \tag{3.2}$$

and for $\dot{m}_R$ to be independent of x we must have, for $l_\beta \leq x \leq L_\beta$

$$\bar{p}_{R'}(x) = 6\mu(sd_R^{-2}(x) - \frac{2}{\rho}\dot{m}_R d_R^{-3}(x)) \tag{3.3}$$

Integrating (3.3) from $x = l_\beta$ to $x = L_\beta$ and setting $\bar{p}_R(l_\beta) = \tilde{p}_R$ (the constant pressure in the right-hand channel recesses) we obtain

$$\bar{p}_R(x) - \tilde{p}_R = \frac{6\mu}{\tan\beta}[s(d_R^{-1}(x) - d_R^{-1}(l_\beta)) - \frac{\dot{m}_R}{\rho}(d_R^{-2}(x) - d_R^{-2}(l_\beta))] \tag{3.4}$$

If we take $\bar{p}_R(L_\beta) = p_{exit} \equiv p_{atm}$ then with $\triangle p_R = p_{atm} - \tilde{p}_R$, setting $x = L_\beta$ in (3.4) yields

$$\triangle p_R = \frac{6\mu}{\tan\beta}[s(d_R^{-1}(L_\beta) - d_R^{-1}(l_\beta)) - \frac{\dot{m}_R}{\rho}(d_R^{-2}(L_\beta) - d_R^{-2}(l_\beta))] \tag{3.5}$$

Equation (3.5) may be solved for $\frac{\dot{m}_R}{\rho}$ in which case

$$\frac{\dot{m}_R}{\rho} = s\lambda_R - \triangle p_R \cdot \frac{\tan\beta}{6\mu}\delta_R \tag{3.6}$$

with the parameters λ_R, δ_R as in appendix I (nomenclature: geometrical parameters).

In an analogous manner, for the left-hand subchannel (figure 10b) the velocity field $\bar{u}_{\mathcal{L}}(x,y), l_\beta \le x \le L_\beta$ is given by (S10), (S11), the pressure distribution is

$$\bar{p}_{\mathcal{L}}(x) - \tilde{p}_{\mathcal{L}} = \frac{6\mu}{\tan\beta}[s(d_{\mathcal{L}}^{-1}(x) - d_{\mathcal{L}}^{-1}(l_\beta)) + \frac{\dot{m}_{\mathcal{L}}}{\rho}(d_{\mathcal{L}}^{-2}(x) - d_{\mathcal{L}}^{-2}(l_\beta))] \tag{3.7}$$

the pressure drop $\Delta p_{\mathcal{L}} = p_{atm} - \tilde{p}_{\mathcal{L}}$ is given by (S12) and the volume flow rate/unit depth in the left-hand subchannel is expressed in (S14) with $\lambda_{\mathcal{L}}$ and $\delta_{\mathcal{L}}$ as given appendix I; in (S14), $\Delta p^{\mathcal{L}} = -\Delta p_{\mathcal{L}}$. Of course, we will always have $\Delta p^R = \tilde{p}_R - p_{atm} > 0$ and $\Delta p^{\mathcal{L}} = \tilde{p}_{\mathcal{L}} - p_{atm} > 0$.

We now relate the mass flow rates per unit depth of the channels, i.e., $\dot{m}_R$ and $\dot{m}_{\mathcal{L}}$, to the roll speed s and the difference $p_{sh} - p_{atm}$. Let w_{sh} stand for the width of the shoe (i.e., the depth of the channel) and let n_c denote the number of capillaries which feed lubricant into each of the two subchannels. Assuming Hagen-Poiseuille flow in the capillaries, which are idealized to be circular cylindrical tubes of length $\tilde{l}_{eff}$ and radius $\tilde{R}_{eff}$, the volume flow rate through any one of the n_c capillaries which feed lubricant into the right-hand subchannel is

$$\dot{q}_c^R = \pi \tilde{R}_{eff}^4 (p_{sh} - \tilde{p}_R)/8\mu\tilde{l}_{eff} \tag{3.8}$$

The volume flow rate through all n_c capillaries which supply lubricant to the right-hand subchannel is, then

$$\dot{q}_c^{R,net} \equiv \frac{n_c \pi \tilde{R}_{eff}^4}{8\mu\tilde{l}_{eff}}(p_{sh} - \tilde{p}_R) = \left(\frac{\dot{m}_R}{\rho}\right) w_{sh} \tag{3.9}$$

Equation (3.9) yields the two relations

$$\tilde{p}_R = p_{sh} - \left(\frac{w_{sh}}{n_c}\right)\frac{8\mu\tilde{l}_{eff}}{\pi\tilde{R}_{eff}^4}\cdot\frac{\dot{m}_R}{\rho} \tag{3.10}$$

and

$$\frac{\dot{m}_R}{\rho} = \left(\frac{n_c}{w_{sh}}\right)\frac{\pi\tilde{R}_{eff}^4}{8\mu\tilde{l}_{eff}}(p_{sh} - \tilde{p}_R) \tag{3.11}$$

From (3.6), however, we obtain

$$\tilde{p}_R = p_{atm} + \frac{6\mu}{(\tan\beta)\delta_R}\left[\frac{\dot{m}_R}{\rho} - s\lambda_R\right] \tag{3.12}$$

so if we set the two expressions for $\tilde{p}_R$ in (3.10) and (3.11) equal to each other there results the following relation for $\dfrac{\dot{m}_R}{\rho}$:

$$\frac{\dot{m}_R}{\rho} = \frac{(p_{sh} - p_{atm}) + \frac{6\mu s}{\tan\beta}(\frac{\lambda_R}{\delta_R})}{\left[\frac{6\mu}{(\tan\beta)\delta_R} + (\frac{w_{sh}}{n_c})\frac{8\mu\tilde{l}_{eff}}{\pi\tilde{R}^4_{eff}}\right]} \tag{3.13}$$

For the left-hand subchannel a similar analysis yields the results delineated in (S16) and (S18).

We now want to compute the normal and tangential forces exerted by the lubricant, in both the right and left-hand subchannels, on the bottom surface of the shoe and the inside surface of the roll; the resulting expressions will then be used to set up the equilibrium equations which serve to determine ψ and d_0 in terms of the other parameters in the model. To compute all the pertinent normal and tangential forces one must derive expressions not only for $\bar{u}_R(x, y)$ and $\bar{u}_{\mathcal{L}}(x, y), l_\beta \leq x \leq L_\beta$, but also for the velocity fields in the channel in the regions between the two sets of recesses and in the regions beneath each of the two sets of recesses.

The normal forces exerted on the roll (shell) in those regions of the right and left-hand subchannels which lie, respectively, between the end of the sets of recesses in the right-hand subchannel and the end of that subchannel and between the beginning of the left-hand subchannel and the point where the set of recesses in the left-hand subchannel begin, namely, $\bar{N}^R_{sl}$ and $\bar{N}^{\mathcal{L}}_{sl}$, are computed as

$$\bar{N}^R_{sl} = \int_{l_\beta}^{L_\beta} (\bar{p}_R(x) - \tilde{p}_R)dx \tag{3.14}$$

and

$$\bar{N}^{\mathcal{L}}_{sl} = \int_{l_\beta}^{L_\beta} (\bar{p}_{\mathcal{L}}(x) - \tilde{p}_{\mathcal{L}})dx \tag{3.15}$$

If we substitute (3.4) into (3.14), and (3.7) into (3.15) and employ $d_R(x) = d_0 - x\tan\beta, d_{\mathcal{L}}(x) = d_0 + \tan\beta$ in the respective integrals, we are led to the algebraic expressions (S19) for $\bar{N}^R_{sl} = -\bar{N}^R_{sh}$, and (S21) for $\bar{N}^{\mathcal{L}}_{sl} = -\bar{N}^{\mathcal{L}}_{sh}$, where $\bar{N}^R_{sh}, \bar{N}^{\mathcal{L}}_{sh}$ are the normal forces exerted on the bottom surface of the shoe by the lubricant in the regions described above.

In both the right and left-hand subchannels, we must also take into account the normal forces exerted by the lubricant, in the regions beneath the respective set of recesses, on the inside surfaces of those recesses and the corresponding domains along the inside surface of the roll (see figure 4). Looking at figure 4 we easily see that these normal forces are given by

$$\begin{cases} \tilde{N}^{R}_{sh} & = -\tilde{N}^{R}_{sl} \quad \equiv \tilde{p}_{R} \cdot w_{rec} \\ \\ \tilde{N}^{\mathcal{L}}_{sh} & = -\tilde{N}^{\mathcal{L}}_{sl} \quad \equiv \tilde{p}_{\mathcal{L}} \cdot w_{rec} \end{cases} \tag{3.16}$$

To compute the normal forces acting on both the bottom surface of the shoe and the inside surface of the roll, in that region of the entire lubrication channel which lies between the two sets of recesses, we must have the pressure distribution in that region; experimental data supports the conclusion that (over a wide range of loads F and speeds s) the pressure field $p_c(x), -l_c \leq x \leq l_c$, in the region of the channel between the two sets of recesses, is simply a linear interpolation of the constant pressures $\tilde{p}_{\mathcal{L}}$ and $\tilde{p}_R$ in those respective sets of recesses. Thus, for the pressure in this 'center' subchannel of the entire lubrication channel we take

$$p_c(x) = \left(\frac{\tilde{p}_R - \tilde{p}_{\mathcal{L}}}{2l_c}\right) x + \left(\frac{\tilde{p}_R + \tilde{p}_{\mathcal{L}}}{2}\right), -l_c \leq x \leq l_c \tag{3.17}$$

The situation corresponding to (3.17) is sketched in figure 11. Using (3.17) we may easily compute, with $\bar{p} = p_c(0) \equiv \frac{1}{2}(\tilde{p}_R + \tilde{p}_{\mathcal{L}})$, that

$$\overset{c\,R}{N}_{sh} \equiv \int_0^{l_c} (p_c(x) - \bar{p})dx = \left(\frac{\tilde{p}_R - \tilde{p}_{\mathcal{L}}}{4}\right) l_c = -\overset{c\,R}{N}_{sl} \tag{3.18}$$

and also,

$$\overset{c\,\mathcal{L}}{N}_{sh} \equiv \int_{-l_c}^{0} (p_c(x) - \tilde{p}_{\mathcal{L}})dx = \left(\frac{\tilde{p}_R - \tilde{p}_{\mathcal{L}}}{4}\right) l_c = -\overset{c\,R}{N}_{sl} \tag{3.19}$$

For the total normal force on that part of the bottom surface of the shoe which bounds this 'center' channel we have

$$\overset{c}{N}_{sh} \equiv \overset{c\,R}{N}_{sh} + \overset{c\,\mathcal{L}}{N}_{sh} = \frac{1}{2}(\tilde{p}_R - \tilde{p}_{\mathcal{L}})l_c \tag{3.20}$$

For the tangential forces acting on the bottom surface of the shoe in the regions described above, where $\bar{N}^{R}_{sh}$ and $\bar{N}^{\mathcal{L}}_{sh}$ are the corresponding normal forces, we have

$$\bar{\mathcal{T}}^{R}_{sh} = -\mu \int_{l_\beta}^{L_\beta} \left(\frac{\partial \bar{u}_R}{\partial y}(x,y) \mid y = d_R(x)\right) dx \tag{3.21}$$

and

$$\bar{\mathcal{T}}^{\mathcal{L}}_{sh} = -\mu \int_{l_\beta}^{L_\beta} \left(\frac{\partial \bar{u}_{\mathcal{L}}}{\partial y}(x,y) \mid y = d_{\mathcal{L}}(x)\right) dx \tag{3.22}$$

respectively. Using (S7) in (3.21), and (S10) in (3.22) we are led, directly, to the expression (S26) for $\bar{\mathcal{T}}_{sh}^{R}$ and the expression (S28) for $\bar{\mathcal{T}}_{sh}^{\mathcal{L}}$. In an analogous fashion, the corresponding tangential forces along the inside surface of the roll are computed from the integrals

$$\bar{\mathcal{T}}_{sl}^{R} = -\mu \int_{l_\beta}^{L_\beta} \left(\frac{\partial \bar{u}_R}{\partial y}(x,y) \mid y = 0 \right) dx \tag{3.23}$$

and

$$\bar{\mathcal{T}}_{sl}^{\mathcal{L}} = -\mu \int_{l_\beta}^{L_\beta} \left(\frac{\partial \bar{u}_{\mathcal{L}}}{\partial y}(x,y) \mid y = 0 \right) dx \tag{3.24}$$

Employing (S7) in (3.23) and (S10) in (3.24) we find for $\bar{\mathcal{T}}_{sl}^{R}$ the expression (S27) and for $\bar{\mathcal{T}}_{sl}^{\mathcal{L}}$ the expression (S29). We remark that the expressions we have derived for $\bar{\mathcal{T}}_{sh}^{\mathcal{L}}$ and $\bar{\mathcal{T}}_{sl}^{\mathcal{L}}$ (as well as the expression for the velocity field $\bar{u}_{\mathcal{L}}(x,y)$) have been computed from the point of view of an observer who views the left-hand subchannel from right to left; care must, therefore, be exercised in combining expressions which are valid in the two distinct subchannels.

It should be clear that, with the obvious notation, the tangential forces $\tilde{\mathcal{T}}_{sh}^{R} = \tilde{\mathcal{T}}_{sh}^{\mathcal{L}} = 0$. To compute the tangential forces exerted by the lubricant on those portions of the inside surface of the roll which lie below the two different sets of recesses, we note that as $p_R(x) = \tilde{p}_R, l_c \le x \le l_\beta$, and $p_{\mathcal{L}}(x) = \tilde{p}_{\mathcal{L}}, l_c \le x \le l_\beta$, we have for the velocity fields under the respective sets of recesses

$$\begin{cases} u_R^{rec} = s(1 - y d_R^{-1}(x)), l_c \le x \le l_\beta \\ u_{\mathcal{L}}^{rec} = -s(1 - y d_{\mathcal{L}}^{-1}(x)), l_c \le x \le l_\beta \end{cases} \tag{3.25}$$

with $u_{\mathcal{L}}^{rec}$ computed from the viewpoint of an observer who views the left-hand subchannel from right to left. Using the velocity fields in (3.25) we easily compute that

$$\tilde{\mathcal{T}}_{sl}^{R} \equiv -\mu \int_{l_c}^{l_\beta} \left(\frac{\partial u_R^{rec}}{\partial y} \mid y = 0 \right) dx = \frac{\mu s}{\tan \beta} \ln \left[\frac{d_R(l_c)}{d_R(l_\beta)} \right] \tag{3.26}$$

and

$$\tilde{\mathcal{T}}_{sl}^{\mathcal{L}} \equiv -\mu \int_{l_c}^{l_\beta} \left(\frac{\partial u_{\mathcal{L}}^{rec}}{\partial y} \mid y = 0 \right) dx = \frac{-\mu s}{\tan \beta} \ln \left[\frac{d_{\mathcal{L}}(l_\beta)}{d_{\mathcal{L}}(l_c)} \right] \tag{3.27}$$

For the velocity fields in the 'center' subchannel we have, in the right-hand portion of that subchannel

$$u_R^c(x,y) = \frac{-p_c'(x)}{2\mu} y(d_R(x) - y) + s(1 - y d_R^{-1}(x)), \tag{3.28}$$

for $0 \leq x \leq l_c$. Using (3.17) in (3.28) we find that

$$\overset{c\,R}{\mathcal{T}}_{sh} \equiv -\mu \int_0^{lc} \left(\frac{\partial u_R^c}{\partial y} \mid y = d_R(x) \right) dx \tag{3.29}$$

is given by (S38) while

$$\overset{c\,R}{\mathcal{T}}_{sl} \equiv -\mu \int_0^{l_c} \left(\frac{\partial u_R^c}{\partial y} \mid y = 0 \right) dx \tag{3.30}$$

is given by (S41). In an analogous fashion,

$$u_{\mathcal{L}}^c(x,y) = \frac{-p_c'(x)}{2\mu} y(d_{\mathcal{L}}(x) - y) - s(1 - y d_{\mathcal{L}}^{-1}(x)), \tag{3.31}$$

for $0 \leq x \leq l_c$, so employing (3.17) in (3.31) we find that

$$\overset{c\,\mathcal{L}}{\mathcal{T}}_{sh} \equiv -\mu \int_0^{l_c} \left(\frac{\partial u_{\mathcal{L}}^c}{\partial y} \mid y = d_{\mathcal{L}}(x) \right) dx \tag{3.32}$$

is given by (S39) while

$$\overset{c\,\mathcal{L}}{\mathcal{T}}_{sl} \equiv -\mu \int_0^{l_c} \left(\frac{\partial u_{\mathcal{L}}^c}{\partial y} \mid y = 0 \right) dx \tag{3.33}$$

is given by (S42).

Remarks: By using the same observer to compute both u_R^c and $u_{\mathcal{L}}^c$ it is an easy exercise to show that (3.28), (3.31), and (3.17) may be combined so as to yield

$$u^c(x,y) = \left(\frac{\tilde{p}_{\mathcal{L}} - \tilde{p}_R}{4\mu l_c} \right) y(d(x) - y) + s(1 - y d^{-1}(x)), \tag{3.34}$$

$-l_c \leq x \leq l_c, d(x) = d_0 - x \tan\beta$, as the expression for the velocity field everywhere in the 'center' subchannel. From either (S38) and (S39) or, directly, from (3.34), we have

$$\overset{c}{\mathcal{T}}_{sh} = \overset{c\,R}{\mathcal{T}}_{sh} + \overset{c\,\mathcal{L}}{\mathcal{T}}_{sh} = \left(\frac{\tilde{p}_{\mathcal{L}} - \tilde{p}_R}{2} \right) d_0 + \frac{\mu s}{\tan\beta} \ln \left[\frac{d(-l_c)}{d(l_c)} \right] \tag{3.35}$$

In a similar manner, from either (S41) and (S42) or, directly, from (3.34)

$$\overset{c}{\mathcal{T}}_{sl} = \overset{c\,R}{\mathcal{T}}_{sl} + \overset{c\,\mathcal{L}}{\mathcal{T}}_{sl} = \left(\frac{\tilde{p}_R - \tilde{p}_{\mathcal{L}}}{2} \right) d_0 + \frac{\mu s}{\tan\beta} \ln \left[\frac{d(-l_c)}{d(l_c)} \right] \tag{3.36}$$

and we observe that, in view of (3.34) and (3.35),

$$\overset{c}{\mathcal{T}}_{sl} + \overset{c}{\mathcal{T}}_{sh} = \frac{2\mu s}{\tan\beta} \ln \left[\frac{d(-l_c)}{d(l_c)} \right] \tag{3.37}$$

so that $\overset{c}{\mathcal{T}}_{sl} \neq -\overset{c}{\mathcal{T}}_{sh}$ for $s \neq 0$.

Remarks: In order to compute the horsepower which must be expended to turn the roll, at a given tangential speed, and a given load on the shoe, we must compute the net tangential force acting on the roll from the point of view of one fixed observer. This net tangential force $\mathcal{T}_{sl}^{net}$ may be obtained by adding together the sum of (S27), (S33), and (S41) with negative one times the sum of (S29), (S34) and (S42); the result is easily computed to be that which is given by the expression in S(44).

Remarks: The pressure distributions in those portions of the lubrication channel which lie to the right of the recesses in the right-hand subchannel, and to the left of the recesses in the left-hand subchannel, are given respectively by (3.4) and (3.7). Using (3.4) we have

$$\bar{p}_{R'}(x) = d_R^{-3}(x)[6\mu s d_R(x) - \frac{12\mu \dot{m}_R}{\rho}] \tag{3.38}$$

and

$$\bar{p}_{R''}(x) = 12\mu \tan\beta d_R^{-4}(x)[s d_R(x) - \frac{3\dot{m}_R}{\rho}] \tag{3.39}$$

Thus, the graph of $\bar{p}_R(x), l_\beta \leq x \leq L_\beta$, has a critical point on the interval (l_β, L_β) if and only if there is a point $x_{crit}, l_\beta < x_{crit} < L_\beta$, with $\bar{p}'(x_{crit}) = 0$. From (3.38), the only candidate for x_{crit} is

$$x_{crit} = \frac{1}{\tan\beta}[d_0 - \frac{2\dot{m}_R}{\rho s}] \tag{3.40}$$

in which case

$$d_R(x_{crit}) = \frac{2\dot{m}_R}{\rho s} \tag{3.41}$$

On the other hand, if x_{crit} as given by (3.40) does not belong to the interval (l_β, L_β), then the graph of $\bar{p}_R(x)$ must be strictly monotone decreasing on this interval, i.e., $\bar{p}'_R(x) < 0, l_\beta < x < L_\beta$. From (3.38), $\bar{p}'_R(x) < 0, l_\beta < x < L_\beta$, implies that, also, $d_R(x) < 2\dot{m}_R/\rho s$ for $l_\beta < x < L_\beta$. But, by (3.39), if $d_R(x) < 2\dot{m}_R/\rho s$, for $l_\beta < x < L_\beta$, then $\bar{p}''_R(x) < -12\mu \tan\beta(\frac{\dot{m}_R}{\rho})d_R^{-4}(x) < 0$, for $l_\beta < x < L_\beta$. Thus if $\bar{p}_R(x)$ has no critical point in (l_β, L_β) then not only is the graph of $\bar{p}_R(x)$ monotone decreasing on this interval but it is also strictly concave down. In an entirely analogous fashion one may show that if the corresponding pressure field in the left-hand subchannel has no critical point on its interval of definition, as we move from left to right in the left-hand subchannel, then the graph of that pressure field is not only strictly monotone increasing but is everywhere concave up; the absence of critical points for the graphs of $\bar{p}_R(x)$ and $\bar{p}_L(x)$ would thus lead one to expect a graph of the overall pressure field which resembles figure 12 and that this is, indeed, the case will be confirmed in the next section.

There remains for us, in this section, the task of delineating the coupled nonlinear system of (algebraic) equilibrium equations which serve to determine the variables d_0 and ψ (that fix the position of the shoe) in terms of the load F (applied at the top of the shaft of the shoe) the tangential speed s of the roll, the pressure drop $p_{sh} - p_{atm}$, the geometry of the shoe, and the properties of the lubricant. Our equilibrium equations will be three in number: an equation expressing balance of forces in the vertical direction, an equation expressing balance of forces in the horizontal direction, and an equation expressing balance of moments of forces. In figure 13 we show yet another sketch of the shoe with the relevant forces that are acting on it; in figure 14 we have sketched the bottom surface of the shoe as it appears with respect to the rectilinear approximations introduced in figure 8. In figures 15a,b and 16a,b respectively, we show the resolution of the various forces acting on the bottom surface of the shoe, in the right and left-hand subchannels, into vertical and horizontal components.

The equation expressing balance of moments of forces for the internal shoe will be constructed by taking moments with respect to the point B (figure 13). In figures 15a and 16a the points $R_i, i = 1,2,3$ and $L_i, i = 1,2,3$ denote the points of application of the normal forces in question (which act on the bottom surface of the shoe) for the purpose of computing the corresponding moments of force. All tangential forces acting on the bottom surface of the shoe act along the approximating secant line segments $\overline{AB}$ and $\overline{BC}$ (through point B) and have, therefore, no net moment with respect to B. Comparing figures 15a and 16a with, respectively, figures 10a and 10b, we see that the moment arms for the normal forces acting along the bottom surface of the shoe have the following lengths:

$$\begin{cases} \overline{BR_1} = \frac{1}{2}L_c = \overline{BL_1} \\ \\ \overline{BR_3} = \frac{1}{2}(L_{rec} + L_T) = \overline{BL_3} \end{cases}$$

Also, from figures 15a, 16a, and 13, $\overline{BR_2} = d_{rec} = \overline{BL_2}$ where d_{rec} is the distance from the middle of the inside of the recesses (left or right) to the center line through the middle of the shoe.

Using the expressions for (x_C, y_C) in (S4) and those for (x_B, y_B) in (S6) we find that η_R (figure 14) satisfies

$$\tan \eta_R = \frac{\cos\psi - \cos(\varphi - \psi)}{\sin(\varphi - \psi) - \sin\psi} \tag{3.42}$$

using the expression for (x_A, y_A) in (S4) leads to the following result for angle $\eta_{\mathcal{L}}$ (figure 14):

$$\tan \eta_{\mathcal{L}} = \frac{\cos\psi - \cos(\varphi + \psi)}{\sin(\varphi + \psi) - \sin\psi} \tag{3.43}$$

Using figures 15a,b and 16a,b it is then a straightforward exercise to show that the sum of all vertical components of all forces (normal and tangential), acting on the bottom surface of the shoe is given by (S47), while the sum of all the corresponding horizontal components is given by (S48). In (S47) a (+) sign denotes forces which act in the direction of the positive y axis, while in (S48) a (+) sign denotes forces which act in the direction of the positive x-axis.

Besides the normal and tangential forces which act along the bottom surface of the shoe, there are several other forces which act on the internal hydrostatic shoe and, thus, affect its equilibrium configurations; these forces are as follows:

(i) the load F applied at the top of the shaft of the shoe which has a vertical component $V_F = -F\cos\psi$ and a horizontal component $H_F = -F\sin\psi$

(ii) the weight of the shoe W, which acts, of course, downward at the location of the centroid (CT) of the shoe so that $V_W = -W$ and $H_W = 0$.

(iii) the restorative forces exerted by stretched and compressed rubber seals and/or springs located, respectively, on the left and right-hand sides of the shaft of the shoe (figure 1b and figure 4); these are each stretched/compressed an amount equal to one-half the difference between the width of the confinement shaft and the width of the shaft of the shoe, i.e., through a distance $\bar{l} = l^* - \hat{l}$ (figure 7). If we assume that the resultant forces act only in the horizontal direction, and that the rubber seals in question can be modeled as mechanical springs with stiffness k_s, then the net horizontal force exerted by stretching and compressing these rubber seals is $H_s = -2k_s\bar{l}$

(iv) finally, as a result of all the forces acting on the shoe, a horizontal reaction force H_{PV} is exerted at the pivot point PV (figure 13).

Using (S47), (S48), (S49), (S50), and (S51), the equations expressing equilibrium in the horizontal and vertical directions take the form

$$H_{sh} + H_F + H_s - H_{PV} = 0 \tag{3.44}$$

and

$$V_{sh} + V_F + V_W = 0 \tag{3.45}$$

As of the writing of this report, accurate data concerning the location of and effective spring constants for all springs and/or seals, which are located along the shaft of the shoe had not been received; in the numerical computations which form the basis for the results presented in §4, therefore, H_s has been set equal to zero both in equation (3.43) and in equation (3.46).

For the equation expressing balance of moments of forces, we note that, within the secant line approximation that has been used, if we take moments with respect to point B on the bottom surface of the shoe (figure 13) there will be no net contribution from the tangential forces acting along the bottom of the shoe as these forces, in the secant line approximation, act along the line segments $\overline{AB}$ and $\overline{BC}$ which go through point B. Denoting moments which tend to turn the shoe clockwise with a plus (+) sign, and those which tend to turn the shoe counterclockwise with a minus (−) sign, we find that the net moment exerted by the normal forces which act either inside the recesses or along the bottom surface of the shoe is given by (S54). Next, if we set $\tilde{d} = \{$ distance between point B and the centroid CT of a cross section of the shoe$\}$ then the length of segment $\overline{BG} = \tilde{d}\sin\psi$ (figure 13) so the weight of the shoe contributes a moment equal to $M_W = W\tilde{d}\sin\psi$. As the load F applied to the shoe acts along the line through $\overline{BE}$, its net moment M_F with respect to point B is zero.

Finally, we recall that the pivot point PV has coordinates (l^*, y_{PV}) with respect to $(0,0)$ where y_{PV} is given by (S2). By virtue of figure 13, the moment arm for the horizontal reaction force H_{PV} has length equal to $d_{PV} = y_{PV} - y_B$, and is easily shown to be given by (S57), so that the corresponding moment of H_{PV} with respect to point B (figure 13) is $M_{PV} = -H_{PV} \cdot d_{PV}$. The complete equation expressing balance of moments of forces for the internal shoe has, therefore, the form

$$M_{sh} + M_W + M_{PV} = 0 \tag{3.46}$$

with the individual moments M_{sh}, M_W, and M_{PV} given, respectively, by (S54), (S55), and (S56). The full set of equilibrium equations for the internal shoe now consists of (3.44), (3.45), and (3.46); this system of three coupled, nonlinear, algebraic transcendental equations may easily be reduced to a system of two coupled equations by solving for H_{PV} from (3.44) and using the resulting expression in (S56) and, then, (3.46). We remark that the system (3.44), (3.45), and (3.46) is an algebraic system of the form

$$\begin{cases} \mathcal{G}_H(F, s, p_{sh} - p_{atm}, R, \phi, R_s, \tilde{R}_{eff}, \tilde{l}_{eff}, \mu, \rho; b, \psi) = 0 \\ \mathcal{G}_V(F, s, p_{sh} - p_{atm}, R, \phi, R_s, \tilde{R}_{eff}, \tilde{l}_{eff}, \mu, \rho; b, \psi) = 0 \\ \mathcal{G}_M(F, s, p_{sh} - p_{atm}, R, \phi, R_s, \tilde{R}_{eff}, \tilde{l}_{eff}, \mu, \rho; b, \psi) = 0 \end{cases} \tag{3.47}$$

which, for fixed values in the parameter space,

$$\mathcal{P} = \left\{F, s, p_{sh} - p_{atm}, R, \phi, R_s, \tilde{R}_{eff}, \tilde{l}_{eff}, \mu, \rho\right\} \tag{3.48}$$

serve to determine the 'deflection' ψ and the parameter b (and, thus, the base thicknesses d_0 of the lubrication channel). Once ψ and d_0 have been determined, for the same fixed values in the parameter space $\mathcal{P}$ we may compute explicit values for $\dot{m}_R, \dot{m}_{\mathcal{L}}, \tilde{p}_R, \tilde{p}_{\mathcal{L}}, \beta$, and the leading and trailing edge thicknesses $d_{\mathcal{L}}(l_\beta)$ and $d_R(l_\beta)$, respectively. We may also compute, explicitly, expressions for all the various velocity fields in the channel (this will be done in the follow-up paper [2] in the course of treating the heat transfer problem in the lubrication channel) as well as for all the normal and tangential forces which act along the bottom surface of the shoe, inside the recesses, and along the inside surface of the roll. From the computation of the net tangential and normal forces exerted, e.g., on the inside surface of the roll, one may readily compute both the horsepower required in order to operate the roll (for given values in the parameter space $\mathcal{P}$) and the drag coefficient

$$c_D^{sl} = \frac{\sum \text{tangential forces on the roll}}{\sum \text{normal forces on the roll}}$$

Some typical numerical computations for two CC roll-internal shoe configurations are presented in §4: one for which $R \neq R_s$ and one in which $R = R_s$; we focus, in particular, on holding all of the variables in $\mathcal{P}$ fixed except for one, e.g., F or s, and study the effect on the mass flow rate, the recess pressure, leading and trailing edge (as well as 'average') thicknesses in the channel, the angle of the deflection of the shoe, the drag coefficient for the roll, the horsepower which must be expended to turn the roll, and the pressure distribution along the inside surface of the roll.

4 SOME NUMERICAL RESULTS FOR CC ROLLS

a. Computational Methods

A FORTRAN computer program was developed (using the Microsoft® FORTRAN compiler, version 5.1, on a 486 IBM-PC compatible microcomputer) to numerically solve the reduced system of two equations for the two unknown variables, b and ψ. These two equations were obtained from the three original equilibrium equations after direct substitution of the expression for H_{PV} into the equation corresponding to balance of moment of forces, and elimination of the equilibrium equation for the horizontal components of forces. As the system of equations is highly non-linear, and strongly coupled in terms of b, ψ, and other variables, and because these parameters are associated with several other transcendental algebraic equations, an iterative scheme was employed to obtain the solutions. To solve the non-linear equations, a specific subroutine (DNEQNF) from the IMSL™ mathematical subroutine library, version 2.0 [6] was called by the FORTRAN program. This subroutine employs a modified Powell hybrid algorithm (a variation of the Newton's method) which uses a finite-difference approximation to the Jacobian matrix. For the analysis performed in this study, the Jacobian is a 2x2 matrix which is obtained by moving all the terms in each of the two equilibrium equations (3.47) to one side, and taking their derivatives with respect to each of the unknown variables d_o and ψ. While the determination of an exact Jacobian is possible, it is a formidable task; thus, it was decided to use a numerical, approach. A finite difference method was used to estimate the Jacobian, using double precision for all real variables, and taking precautions to avoid large step sizes or increasing residuals. For each operating condition, appropriate initial guesses for b and ψ were introduced and the stopping criterion for iteration was taken to be that point at which the sum of the squares of the residual values corresponding to each equation was small (e.g., $<10^{-3}$).

In the computer model, viscosity and density data for the oil were assumed to be 56 centipoise and 873 Kg/m^3, respectively (typical of an ISO 150 mobil oil at a temperature of 57°C). These properties correspond to the lubricant employed in the experiments conducted by the Beloit corporation for the small roll/shoe configuration [7]. Since the speed of the roll, and the load applied to the top of the shoe, are two of the most important input parameters which can be controlled by an operator, for specific design conditions, all the calculated values were obtained as a function of these two parameters. Shown in Table 1 are the input values of the outer surface roll speed and applied load in U.S. Engineering Units and their equivalent values in International System (SI) units. A calculation was performed for selected outer surface roll speed and load combinations (Table 1) for two roll/shoe configurations with different dimensions. One shoe/roll system was analyzed for applied loads in the range 35-175 KN/m (200-1000 PLI), and roll speed of 305-914 m/min (1000-3000 ft/min), the other one was subjected to applied loads between 175-1751 KN/m (1000-10,000 PLI), and outer surface roll speeds of 305-1067 m/min (1000-3500 ft/min).

b. Results and Discussion for a CC Roll with $R_s \neq R$

In this section the results for a shoe/roll configuration in which the radius of the shoe (R_s) is 171.32 mm (6.745 in) and the inside radius of the roll (R) is 171.45 mm (6.750 in) will be presented. For the sake of simplicity, throughout this section, this shoe/roll configuration is identified by 'small' or '$R_s \neq R$'. In the next section, the results for another shoe/roll configuration (with a roll inside radius of 508.13 mm or 20.005 in) in which the shoe and the roll are machined to the same radius ($R_s = R$) will be presented. This system will be identified by the labels 'large' or '$R_s = R$'. The small roll is subjected to outer surface roll speeds of 305-914 m/min (1000-3000 ft/min) and applied loads of 35-175 KN/m (200-1000 PLI).

Shown in figure 17 are the lubricant film thicknesses at the leading edge vs. the roll speed for various applied loads in the range 35-175 KN/m (200-1000 PLI). The leading edge corresponds to the point at the end of the left-hand recess. For a constant load, the lubricant film thickness increases with the roll speed because of the hydrodynamic effect of the lubricant which increases the magnitude of the normal force exerted by the fluid on the bottom surface of the shoe. This increase in the lubrication film thickness is more rapid at relatively lower applied loads. Similar qualitative results were obtained for the lubricant film thickness at the trailing edge (figure 18). The trailing edge corresponds to the point at the end of the right-hand recess. As expected, a smaller lubrication thickness corresponds to the operation of the roll at a higher load and smaller speed. Under the influence of an external load applied to the top of the shoe, and the normal and tangential forces exerted by the lubricant on the bottom of the shoe, the hydrostatic shoe is free to rotate about a pivot point on the confinement wall and to move up or down along the confinement wall at that pivot point (see figure 6). If the shoe experiences only a clockwise rotation and no vertical motion, then at the leading edge the channel becomes more divergent, and its thickness will increase with speed, while at the trailing edge the channel becomes more convergent and its thickness will decrease with speed. However, an upward motion of the shoe causes both the leading edge and trailing edge thicknesses to increase simultaneously. The increase in the leading edge and the trailing edge thicknesses with speed (figures 17-18) indicates that in addition to its clockwise rotation, the 'small' shoe is also subjected to an upward motion. However, as the roll speed increases, the influence of the clockwise rotation becomes relatively smaller than that of the vertical motion.

Shown in figures 19-21 are a comparison between the lubricant thicknesses predicted by the IPST model and those measured by the Beloit Corporation for the roll speeds of 305, 610 and 914 m/min (1000, 2000, and 3000 ft/min). It is important to indicate that throughout this section, the results from the model for the 'small' roll/shoe configuration correspond to an inner roll radius of 6.75", while the experimental data, we learned later on from Beloit Corporation, correspond to an inner radius of 6.76". A more relevant comparison with experimental data obtained by Beloit, for some operating conditions may be found in Appendix V, which was written after the bulk of this report had been completed. The model and experiment both indicate that lubricant thicknesses increase with speed and decrease with load. Also, both results demonstrate that variations in film thickness decrease at higher applied loads. Based on these qualitative agreements between the model and the experiment it can be concluded that the operation of the roll at higher loads results in higher stability for the internal shoe with respect to variation in roll speed. It should be emphasized that in the computer model, the influence of the physical constraints associated with a spring or rubber seal, which is placed in the rib at the pivot point (figure 4), has not been considered because spring constants were not available. It is not known whether the horizontal reaction force associated with this spring/seal has any major influence on the magnitude of the angle of deflection (ψ). However, it appears that over-prediction of the angle of rotation by the model, has resulted in an over-prediction of the leading edge thickness and an under-prediction of the trailing edge thickness as compared with experimental measurements. In general, there was better agreement between the model and experiment for the average values of the leading edge and trailing edge thicknesses (figures 22-24). Work is underway to generate additional data from the model that correspond to the same roll geometric conditions as the experimental data. For these conditions, much better agreement between the model and experimental data was obtained (see Appendix V).

We show in figures 25 and 26, the angle of rotation of the shoe (ψ) as a function of load for constant speeds, and as a function of speed for constant loads, respectively. A positive value for ψ corresponds to a clockwise rotation of the shoe. These figures indicate that for all the operating conditions analyzed in this study, the shoe rotates in a clockwise direction. The greatest clockwise rotation of the shoe corresponds to the operating condition with the smallest applied load (35 KN/m), and the largest roll speed (914 m/min). For a constant roll speed, as the applied load is increased, the angle of rotation is decreased (figure 25). However, at a fixed roll speed and higher applied loads the curves become flatter which indicates that under these conditions, the hydrostatic shoe becomes more stable with respect to variation in applied loads. For a fixed load, as the roll speed increases, the normal and tangential forces exerted by the lubricant on the bottom surface of the shoe are increased in such a way that they result in an increase in the clockwise rotation of the shoe. When the applied load is small (e.g., 35 KN/m), the angle of rotation increases more rapidly with the speed of the roll. At a higher load (e.g., 175 KN/m), the forces exerted by the fluid on the shoe are not large enough to overcome the force applied to the top of the shoe, thus, they result in a smaller clockwise rotation. No experimental data is available for the angle of rotation. However, as indicated earlier, it appears that these calculated values are generally higher than the actual rotation of the shoe. Incorporation of additional details in the computer model for the 'small' roll/shoe configuration (e.g., more geometric refinements, and consideration of the tapering of the shoe, spring constant, and temperature dependant viscosity, etc.) is expected to reduce the magnitude of these calculated values.

Shown in figure 27 are the mass flow rates of the lubricant in the left-hand and right-hand channels as a function of applied load for three outer surface roll speeds. Because of the clockwise rotation of the shoe, the left-hand channel becomes more divergent and its thickness becomes larger than that of the right-hand channel. Therefore, the lubricant flow rate in that channel is larger as compared with the right-hand channel. As the applied load is increased, because of the increase in the pressure gradient across the channel, more flow is passed through the left-hand channel. However, the lubricant flow rate in the right-hand channel is relatively insensitive to variation in applied loads, and the influence of the roll speed on the mass flow rate in that channel is greater as compared to that in the left-hand channel. For a fixed roll speed, an increase in applied load will influence the lubricant mass flow rates through two mechanisms: on one hand it will produce a thinner channel and thus will create more resistance to the flow of the lubricant. On the other hand, an increase in the applied load will result in a greater pressure gradient across the channel which will result in an increase in fluid motion. The amount of lubricant passing through each capillary is strongly influenced by the pressures at the top of the shoe and in the recess. As will be shown in the graphs referenced below, an increase in applied load will result in a much greater increase in the pressure in the right-hand recess than that in the left-hand recess. Therefore, for a fixed load, the pressure gradient across the left-hand capillaries will be greater than that across the right-hand capillaries. This will result in a greater flow of lubricant through the left-hand channel. As the speed of the roll is increased, the viscous nature of the lubricant will drag part of the lubricant from the left-hand channel toward the right-hand channel.

We show in figure 28 the lubricant total volumetric flow rate vs. roll speed for each applied load. The flow rate increases with speed and applied load because of an increase in the thickness of each channel and an increase in the pressure gradient, respectively. However, as this figure indicates, the influence of the applied load on the flow of lubricant is much greater than that of the roll speed. The influence of the speed of the roll on the fluid flow rate is the same for all applied loads. Shown in figures 29-31 are a comparison between the lubricant volumetric flow rates predicted by the IPST model and those measured by the Beloit Corporation for the outer surface roll speeds of 305, 610, and 914 m/min, respectively. In general, very good agreement between the model and experimental data were obtained for higher applied loads. The reason for the sudden changes in the slope of the curves for the experimental data associated with the roll speeds of 305 m/min and 914 m/min is not known. However, viscous fluid flow measurements, in general, are associated with experimental errors which may vary in magnitude depending on the type of flow measuring device. In the analytical model, the lubricant flow rate through each capillary tube was calculated using the Hagen-Poiseuille equation which generally applies to tubes with a large length-to-diameter ratio, e.g., $l_{cap}/2R_{cap} = 100$ or higher [8]. In this equation, the flow rate through a capillary is a function of l_{cap}/R_{cap}^4. Since there were variations in the diameter at some locations along the length of each capillary, an appropriate effective radius and effective length were introduced by obtaining the total volume of each capillary tube.

We show in figures 32 and 33 the lubricant recess pressures in the left-hand and right-hand channels as a function of roll speed and applied load, respectively. Figure 32 indicates that an increase in roll speed from 305 to 914 m/min results in a negligible increase in the left-hand recess pressure, and only a small decrease in the right-hand recess pressure. Therefore, the influence of roll speed on the lubricant flow rate through the left-hand channel was negligible (figure 27), and its influence on the total flow rate was small (figure 28). As explained earlier, for a fixed roll speed, an increase in applied load resulted in a much greater increase in the right hand recess pressure as compared with the left hand recess pressure (figure 33). Therefore, under these conditions the left-hand capillaries (which are associated with a greater increase in pressure gradient) will experience a larger mass flow rate (see figure 27).

Shown in figures 34a-36b are lubricant pressure distributions along the length of the left-hand, and right-hand channels at various roll speeds. The mathematical expressions for the pressure distributions along the length of the right-hand and left-hand channels are given in equations (3.4) and (3.7), respectively. These equations were employed to determine the lubricant pressure distribution along the channels for the 'large' shoe/roll configuration. For the small shoe/roll configuration, the pressure distribution in the left-hand channel was obtained directly from equation (3.7). However, because of the under-prediction of the trailing edge thickness for the 'small' shoe, which is associated with a lack of information about the pertinent spring constant, and because of the strong sensitivity of the pressure in the right-hand channel with respect to trailing edge thickness, equation (3.4) could not be used directly for determination of the pressure distribution at this region. Based on the behavior of the fluid pressure along the left-hand channel for the 'small' shoe, a quadratic pressure distribution was considered along the right-hand channel using prescribed boundary conditions at the end of the recess ($P=P_R$), and at the end of the channel ($P=P_{atm}$). Also, a fixed percentage of the pressure drop was assumed, at the mid-point between the end of the right recess and the end of the right-hand channel.

In general, the shape of the pressure curves for the right-hand channels were concave downward, and those for the left-hand channel were concave upward. In other words, the pressure drop near the recess at the right-hand channel was smaller than that of the left-hand channel. As the magnitude of applied load increases, the nonlinearity in the pressure distribution in both channels increases. Shown in figure 37 are the roll drag coefficient vs. roll speed at each applied load. This coefficient was calculated from the ratio of total shear force exerted by the lubricating oil to the inner surface of the roll divided by the total normal force applied to the roll. This figure indicates that the roll drag coefficient increases with roll speed for a constant applied load, and decreases with applied load for a fixed roll speed.

We show in figure 38 a comparison between the predicted and measured values of the mechanical power required to operate the roll vs. load for three fixed roll speeds. As indicated earlier, the inner radius of the roll, in the model was considered to be 6.75", while, in the experiment it was 6.76". A more relevant comparison between the mechanical power predicted from the model and measured by Beloit Corporation may be found in Appendix V. The power was obtained from the product of the net shear force on the roll, and the inner surface roll speed. In general, the predicted values from the model were greater than the measured values. Again, it is expected that refinement of the model (e.g., by incorporation of additional geometric details, the tapering of the shoe, the spring constant, and a temperature dependent viscosity) will reduce the shoe's rotation, and thus, will reduce the total shear force exerted by the fluid on the roll; this reduction of net shear force will cut down the calculated values of the mechanical power. For this roll/shoe configuration, the power increased with load at a constant roll speed, and increased with speed at a constant applied load (figure 39). Figures 38 and 39 show that the slopes of the power curves become greater at both higher roll speeds and applied loads.

C. Results and Discussion for a CC Roll with $R_s = R$

Shown in figures 40-60 are the results of the analytical model for the 'large' shoe in which the roll and the shoe are machined to the same radius of 508.13 mm ($R_s = R = 20.005$ in). This shoe was subjected to loads in the range of 175-1751 KN/m (1000-10,000 PLI) and roll speeds of 305-1067 m/min (1000-3500 ft/min). With only minor exceptions, the qualitative results obtained for the 'large' shoe were similar to those of the 'small' shoe. Therefore, for the sake of conciseness, only those results that are qualitatively different from the small shoe will be discussed in this section. As shown in figure 41, for a fixed load, the lubrication film thickness at the trailing edge decreases with an increase in roll speed. This indicates that for the 'large' shoe, as the roll speed increases, the influence of the rotation of the shoe on the thickness of the lubricant becomes relatively greater than that of its vertical motion. This was not observed in the results for the 'small' shoe (see figure 18). Similar to the results for the 'small' shoe, lubricant thickness and angle of rotation data indicate that operation of the large roll at higher loads will result in higher stability for the hydrostatic shoe with respect to variation in roll speed.

While for the small roll, the mass flow rate passing through the left-hand channel was much greater than that of the right-hand channel (figure 27), for the large roll, a negligible difference between the two flows was observed (figures 44-47). This similarity between the flow magnitudes occurs, because for the large roll at a fixed speed, there is a small difference between the recess pressures in the left-hand and right-hand channels (see figures 50-53). However, for the 'small' shoe, the recess pressure in the right-hand channel was generally much greater than that in the left-hand channel; for a fixed applied load and roll speed, this results in a smaller pressure drop across the capillaries of the right-hand channel as compared with those of the left-hand channel, thus allowing more flow of lubricant into the left-hand channel (see figure 27).

In general, for the 'large' shoe subjected to a fixed load, the speed of the roll has no major effect on the lubricant flow rate (figure 48). However, for the 'small' roll at a fixed applied load, an increase in roll speed resulted in a small increase in the lubricant flow rate (figure 28). Generally, the nonlinearity in the pressure distributions along each channel were higher for the 'large' shoe as compared with the 'small' shoe (figures 34a-36b). We show in figures 54-57, the lubricant pressure distributions along the length of both channels for each applied load and each roll speed. In general, speed of the roll had only small influence on the pressure distribution. Note that at the region between the leading edge and trailing edge, for all the operating conditions, the pressure exerted by the lubricant on the inner surface of the roll is slightly higher at the right-hand recess as compared with the left-hand recess. The pressure distribution at this region has a significant effect in water removal during the wet pressing of paper. Since the machine direction width of the piston for the 'large' shoe was chosen to be 152.2 mm (5.994"), the corresponding magnitude of the pressures applied to the top of the shoe will be in the range of 2.3-11.5 MPa (for the applied loads of 350-1751 KN/m). Therefore, based on the results shown in figures 54-57, in general, the ratio of the average recess pressure divided by the pressure applied to the top of the shoe was approximately 0.6 for all the operating conditions. For the 'small' roll/shoe configuration, the predicted mechanical power required to operate the roll increases with applied load and roll speed, and the rate of increase was generally higher at higher applied loads and roll speeds. However, for the 'large' roll/shoe, operating at a fixed roll speed, the power was relatively insensitive to changes in applied load.

This indicates that variation in applied loads does not change the magnitude of net shear force which is exerted by the lubricant to the inner surface of the roll. At higher loads this corresponds to insensitivity of the angle of rotation of the shoe with respect to variations in applied loads. At any fixed load, the mechanical power required to operate this roll increased nonlinearly with increasing speed.

Previously referenced figures corresponding to lubrication film thickness and angle of rotation for each roll/shoe configuration analyzed in this study indicate that operating such press rolls at higher loads will result in a more stable hydrostatic shoe, one in which the position of the shoe becomes relatively independent of the variation in the roll speed. Figures 38 and 39 show that operation of the 'small' roll at a high speed and high load requires a significantly higher power as compared with its operation at a moderate speed and load; however, the results corresponding to mechanical power, for the large roll (figure 60) indicate that this roll/shoe configuration can be operated at a higher load without any significant increase in mechanical power. Also, under these operating conditions, based on the results for the film thickness (figures 40-41), and angle of rotation (figures 42-43), the hydrostatic shoe will be in a more stable configuration.

It is important to emphasize that the results of this study were based on an analytical model in which the curved-wall channels were approximated by planar-wall channels, and no consideration was given to the tapering at the bottom surface of the shoe. Also, the viscosity and density of the lubricating oil were assumed to be constant. Some of the qualitative differences between the results for the 'small' shoe/roll as compared with those of the 'large' shoe/roll configuration may be associated with a higher sensitivity of the 'small' roll to the effect of these assumptions. Because the 'large' shoe has a much higher diameter, and is subjected to much larger applied loads as compared with the 'small' shoe, the influence of the geometric approximation of the channel, and the reaction force from the spring/seal, on the qualitative results obtained for this shoe, is expected to be insignificant as compared with those for the 'small' roll. Further research is needed to explore major differences between the behavior of 'small' shoe/roll and 'large' shoe/roll, and to determine the optimal performance of each press roll under various operating conditions.

5 CONCLUSIONS

1. In general, the results predicted from the analytical model agreed well with the experimental data obtained from the Beloit Corporation for the 'small' shoe/roll configuration. Additional comparisons between the results predicted from the model and those obtained from experimental measurements, based on new information from Beloit Corporation regarding certain dimensions associated with the 'small' roll/shoe configuration, is provided in Appendix V.

2. The model indicated that, for both shoe/roll configurations, operation of the rolls at relatively higher loads will result in greater stability for the shoe with respect to variations in roll speed. While for the 'large' roll/shoe configuration, the mechanical power required to operate the roll is relatively insensitive to an increase in applied load, for the 'small' roll/shoe configuration, the required power increases significantly with an increase in applied load.

3. The results of this study indicate that this analytical model can be used effectively to predict the influence of specific design and physical parameters on the performance of the press roll, and to determine its optimal performance under various operating conditions.

4. Work is under way to refine the present model, and to develop additional analytical models to predict heat transfer, and temperature characteristics associated with these press rolls. The pressure distribution predicted from the refined model will be incorporated in a finite element model to determine the thermal stress distribution within the roll ceramic coating, for various design and operating conditions.

REFERENCES

1. Orloff, D.I., Jones, G.L., and P.S. Phelan, "The Effects of Heating Mode and Internal Roll Temperature on Roll Durability and Efficiency of Impulse Drying," HTD-vol 193, Fundamentals of Heat Transfer in Porous Media. ASME 1992, 141-155.

2. Bloom, F., Hojjatie, B., and D. Orloff, "Modeling of Fluid Flow and Heat Transfer in a Crown Compensated Roll I: The Heat Transfer Problem," IPST Tech. Rep. 9, forthcoming.

3. Orloff, D.I., Unpublished Notes, Institute of Paper Science and Technology; Atlanta, Georgia.

4. Schlichting, H., *Boundary Layer Theory*, McGraw-Hill, 1960.

5. Batchelor, G.K., *An Introduction to Fluid Dynamics*, Cambridge University Press, 1990.

6. IMSLTM Math/Library, Fortran Subroutines for Mathematical Applications, version 2.0, User's Manual, Visual NumericsTM, Houston, TX 1991.

7. Beloit Corporation, Research and Development Center, Rockton, Illinois.

8. Rowe, W.B., Hydrostatic and Hybrid Bearing Design, Cambridge University Press, 1983.

Acknowledgements

The work reported here was supported by member companies of the IPST and by the U.S. Department of Energy, Office of Industrial Programs, through Grant No. DE-FG02-8SCE40738. Their support is gratefully acknowledged. The authors wish to acknowledge the Beloit Corporation for providing the experimental data used in this report as well as for valuable discussions with David Lang, Paul Monroe, and Rajendra Deshpande, of the Beloit Research and Development Center, on the subject matter of this report.

APPENDIX I: NOMENCLATURE

Design Parameters

Φ - angular opening of the shoe

$\phi = \frac{1}{2}\Phi$

w_{sh} - width (depth) of the shoe

n_c - number of capillaries on each side of the shoe

l_{sh} - length of the shaft of the shoe

$\hat{l} = \frac{1}{2}l_{sh}$

l^* - half-width (length) of the confinement shaft

$\tilde{l}_{eff}$ - effective length of a capillary

$\tilde{R}_{eff}$ - effective radius of a capillary

w_{rec} - width (length) of the inside of a recess

α_r - distance of the middle rib on the shaft of the shoe from the top of the shaft (measured to the middle of that rib)

β_r - distance that the middle rib protrudes beyond the neighboring ribs

R_s - radius of the shoe

R - radius of the roll

H_s - height of the shoe

$\delta = \tan^{-1}\left(\frac{R_s - H_s}{\hat{l}}\right)$

L_c - distance (measured along the bottom surface of the shoe) from the midpoint on the bottom surface to the beginning of the recess

L_{rec} - distance (measured along the bottom surface of the shoe) from the midpoint on the bottom surface to the end of the recess

$L_T = R_s \cdot \varphi$

$\tilde{d}$ - distance from the centroid of a cross section of the shoe to the middle of the arc describing the bottom surface of the shoe

Geometrical Parameters

ψ - angle between the center line through the shoe and the vertical direction

$(a, R+b)$ - location of the center of the circle that the arc forming the bottom surface of the shoe lies on

d_0 - depth of the lubrication channel along the line through $(a, R+b)$ and the point at the middle of the arc forming the bottom surface of the shoe

PV - location of the pivot point for the shoe along the wall of the confinement shaft

$m_{\mathcal{L}} = \cot(\varphi + \psi)$

$m_C = \cot \psi$

$m_R = \cot(\psi - \varphi)$

θ_1 - angle between the positive x-axis and the secant line (segment) joining the endpoints of the lubrication channel along its bottom wall (arc)

θ_2 - angle between the positive x-axis and the secant line (segment) joining the endpoints of the lubrication channel along its upper wall (arc)

$\beta = \theta_1 - \theta_2$ - angular deviation between the (secant) line segments forming the upper and lower walls of the approximating lubrication channel (wedge)

η_R - angle between the positive x-axis and the secant line (segment) joining the point at the middle of the bottom surface (arc) of the shoe with the endpoint of that arc on the right-hand side of the shoe

$\eta_{\mathcal{L}}$ - angle between the negative x-axis and the secant line (segment) joining the point at the middle of the bottom surface (arc) of the shoe with the endpoint of that arc on the left-hand side of the shoe

$(d_R(x) = d_0 - x\tan\beta)$ - thickness of the approximating lubrication channel (wedge) x units to the right of the middle of that channel

$(d_{\mathcal{L}}(x) = d_0 + x\tan\beta)$ - thickness of the approximating lubrication channel (wedge) x units to the left of the middle of that channel

d_{PV} - vertical distance of the pivot point PV above the point in the middle of the arc describing the surface of the shoe

$l_c = L_c \cos\beta$

$l_\beta = L_{rec}\cos\beta$

$L_\beta = L_T \cos\beta$

$d_R(l_\beta)$ - trailing edge thickness in the approximating lubrication channel (wedge)

$d_{\mathcal{L}}(l_\beta)$ - leading edge thickness in the approximating lubrication channel (wedge)

$$\lambda_R = \frac{d_R(l_\beta)d_R(L_\beta)}{d_R(l_\beta) + d_R(L_\beta)}$$

$$\delta_R = \frac{d_R^2(l_\beta)d_R^2(L_\beta)}{d_R^2(l_\beta) - d_R^2(L_\beta)}$$

$$\lambda_{\mathcal{L}} = \frac{d_{\mathcal{L}}(l_\beta)d_{\mathcal{L}}(L_\beta)}{d_{\mathcal{L}}(l_\beta) + d_{\mathcal{L}}(L_\beta)}$$

$$\delta_{\mathcal{L}} = \frac{d_{\mathcal{L}}^2(l_\beta)d_{\mathcal{L}}^2(L_\beta)}{d_{\mathcal{L}}^2(l_\beta) - d_{\mathcal{L}}^2(L_\beta)}$$

Physical Parameters

μ - viscosity of the lubricant (at a given temperature)

ρ - density of the lubricant (at a given temperature)

s - (tangential) speed of the inner surface of the roll

F - load applied to the top of the shaft of the shoe

$\tilde{p}_R$ - pressure in the right-hand recess

$\tilde{p}_{\mathcal{L}}$ - pressure in the left-hand recess

p_{sh} - pressure exerted at the top of the shaft of the shoe

$p_{exit}(\equiv p_{atm})$ - exit pressure of the lubricant at the left and right-hand ends of the lubrication channel

$\bar{p}_R(x)$ - pressure field in the (approximate) right-hand channel, $l_\beta \leq x \leq L_\beta$

$\bar{p}_{\mathcal{L}}(x)$ - pressure field in the (approximate) left-hand channel, $l_\beta \leq x \leq L_\beta$

$\bar{C}_R(x) = -\bar{p}'_R(x)$

$\bar{C}_{\mathcal{L}}(x) = -\bar{p}'_{\mathcal{L}}(x)$

$\bar{u}_R(x, y)$ - velocity field in the (approximate) right-hand channel, $l_\beta \leq x \leq L_\beta$

$\bar{u}_{\mathcal{L}}(x, y)$ - velocity field in the (approximate) left-hand channel, $l_\beta \leq x \leq L_\beta$

$\dot{m}_R$ - mass flow rate/unit depth in the right-hand channel

$\dot{m}_{\mathcal{L}}$ - mass flow rate/unit depth in the left-hand channel

$\triangle p_R = \bar{p}_R(L_\beta) - \tilde{p}_R \equiv p_{atm} - \tilde{p}_R$

$(\triangle p^R = -\triangle p_R)$

$\triangle p_{\mathcal{L}} = p_{\mathcal{L}}(L_\beta) - \bar{p}_{\mathcal{L}} \equiv p_{atm} - \bar{p}_{\mathcal{L}}$

$(\triangle p^{\mathcal{L}} = -\triangle p_{\mathcal{L}})$

$\dot{q}_c^R$ - volume flow rate through any one of the n_c capillaries feeding lubricant into the right-hand subchannel

$\dot{q}_c^{R,net}$ - net volume flow rate through the capillaries feeding lubricant into the right-hand subchannel

$\dot{q}_c^{\mathcal{L}}, \dot{q}_c^{\mathcal{L},net}$ - same as for $\dot{q}_c^R, \dot{q}_c^{R,net}$, but for the left-hand subchannel

$u_R^c(x,y)$ - the velocity field in the right-hand subchannel for $0 \leq x \leq l_c$

$u_{\mathcal{L}}^c(x,y)$ - the velocity field in the left-hand subchannel for $0 \leq x \leq l_c$

$u^c(x,y)$ - velocity field in the lubrication channel for $-l_c \leq x \leq l_c$

$p_c(x)$ - pressure field in the lubrication channel for $-l_c \leq x \leq l_c$

$C_R^c(x) = -p_c'(x), 0 \leq x \leq l_c$

$C_{\mathcal{L}}^c(x) = -p_c'(x), -l_c \leq x \leq 0$

$u_R^{rec}(x,y)$ - velocity field in the right-hand subchannel beneath the right-hand recess

$u_{\mathcal{L}}^{rec}(x,y)$ - velocity field in the left-hand subchannel beneath the left-hand recess

$\bar{N}_{sh}^R$ - normal force exerted by the lubricant on the bottom surface of the shoe to the right of the right-hand recess

$\bar{N}_{sl}^R$ - normal force exerted by the lubricant on the inside surface of the roll (lying in the channel) to the right of the right-hand recess

$\tilde{N}_{sh}^R$ - normal force exerted by the lubricant on the inside surface of the right-hand recess

$\tilde{N}_{sl}^R$ - normal force exerted by the lubricant on the inside surface of that part of the roll lying beneath the right-hand recess

$\overset{c}{N}{}^{R}_{sh}$ - normal force exerted by the lubricant on the bottom surface of the shoe between the middle of the shoe and the beginning of the right-hand recess

$\overset{c}{N}{}^{R}_{sl}$ - normal force exerted by the lubricant on the inside surface of that part of the roll lying beneath the middle of the shoe and the beginning of the right-hand recess

$\bar{N}^{\mathcal{L}}_{sh}$ - same as $\bar{N}^{R}_{sh}$, but to the left of the left-hand recess

$\bar{N}^{\mathcal{L}}_{sl}$ - same as $\bar{N}^{R}_{sl}$, but to the left of the left-hand recess

$\tilde{N}^{\mathcal{L}}_{sh}$ - same as $\tilde{N}^{R}_{sh}$, but on the inside surfaces of the left-hand recess

$\tilde{N}^{\mathcal{L}}_{sl}$ - same as $\tilde{N}^{R}_{sl}$, but beneath the left-hand recess

$\overset{c}{N}{}^{\mathcal{L}}_{sh}$ - same as $\overset{c}{N}{}^{R}_{sh}$, but between the middle of the shoe and the beginning of the left-hand recess

$\overset{c}{N}{}^{\mathcal{L}}_{sl}$ - same as $\overset{c}{N}{}^{R}_{sl}$, but beneath the middle of the shoe and the beginning of the left-hand recess

$\bar{\mathcal{T}}^{R}_{sh}$ - tangential force exerted by the lubricant on the bottom surface of the shoe to the right of the right-hand recess

$\bar{\mathcal{T}}^{R}_{sl}$ - tangential force exerted by the lubricant on that part of the inside surface of the roll (lying in the channel) to the right of the right-hand recess

$\tilde{\mathcal{T}}^{R}_{sl}$ - tangential force exerted by the lubricant on that part of the inside surface of the roll lying beneath the right-hand recess

$\overset{c}{\mathcal{T}}{}^{R}_{sh}$ - tangential force exerted by the lubricant on the bottom surface of the shoe between the middle of the shoe and the beginning of the right-hand recess

$\overset{c}{\mathcal{T}}{}^{R}_{sl}$ - tangential force exerted by the lubricant on that part of the inside surface of the roll lying beneath the middle of the shoe and the beginning of the right-hand recess

$\bar{\mathcal{T}}^{\mathcal{L}}_{sh}$ - same as $\bar{\mathcal{T}}^{R}_{sh}$, but to the left of the left-hand recess

$\bar{\mathcal{T}}^{\mathcal{L}}_{sl}$ - same as $\bar{\mathcal{T}}^{R}_{sl}$, but to the left of the left-hand recess

$\tilde{\mathcal{T}}_{sl}^{\mathcal{L}}$ - same as $\tilde{\mathcal{T}}_{sl}^{R}$, but beneath the left-hand recess

$\overset{c}{\mathcal{T}}{}_{sh}^{\mathcal{L}}$ - same as $\overset{c}{\mathcal{T}}{}_{sh}^{R}$, but between the middle of the shoe and the beginning of the left-hand recess

$\overset{c}{\mathcal{T}}{}_{sl}^{\mathcal{L}}$ - same as $\overset{c}{\mathcal{T}}{}_{sl}^{R}$, but between the middle of the shoe and the beginning of the left-hand recess

V_{sh} - sum of the vertical components of all forces acting on the bottom surface of the shoe

H_{sh} - sum of the horizontal components of all forces acting on the bottom surface of the shoe

V_F - vertical component of the load F

H_F - horizontal component of the load F

V_W - vertical component of the weight W of the shoe

H_W - horizontal component of the weight W of the shoe

k_s - 'equivalent' spring constant for the rubber seals along the shaft of the shoe

H_s - horizontal force which results from compressing/stretching the rubber seals located along the shaft of the shoe

H_{PV} - horizontal reaction force of the confinement wall at the pivot point

M_{sh} - moment of all forces acting along the bottom surface of the shoe

M_W - moment of the weight of the shoe

M_{PV} - moment of the horizontal reaction force at the pivot point for the shoe along the wall of the confinement shaft

$\mathcal{P}$ - physical/geometrical/design parameter space for the equilibrium equations

c_D^{sl} - drag coefficient for the roll

APPENDIX II: TECHNICAL SUMMARY

(S1) $$a = l^* - \beta_r \cos\psi + \alpha_r \sin\psi - \frac{\hat{l}}{\cos\psi(1+\tan\psi\tan(\delta+\psi))}$$

(S2) $$\begin{cases} x_{PV} = l^* \\ y_{PV} = (R+b) - \alpha_r\cos\psi - \beta_r\sin\psi - \tan(\delta+\psi)\left[\dfrac{\hat{l}}{\cos\psi(1+\tan\psi\tan(\delta+\psi))}\right] \end{cases}$$

(S3) $$\begin{cases} \theta_1 = \tan^{-1}\left(\dfrac{y_{C'} - y_{A'}}{x_{C'} - x_{A'}}\right) \\ \begin{cases} x_{A'} = \dfrac{1}{(1+m_{\mathcal{L}}^2)}\left[m_{\mathcal{L}}^2 a - m_{\mathcal{L}} b - \sqrt{R^2(1+m_{\mathcal{L}}^2) - (b - m_{\mathcal{L}} a)^2}\right] \\ x_{C'} = \dfrac{1}{(1+m_R^2)}\left[m_R^2 a - m_R b + \sqrt{R^2(1+m_R^2) - (b - m_R a)^2}\right] \end{cases} \\ \begin{cases} y_{A'} = m_{\mathcal{L}}(x_{A'} - a) + R + b \\ y_{C'} = m_R(x_{C'} - a) + R + b \end{cases} \end{cases}$$

(S4) $$\begin{cases} x_A = a - R_s\sin(\varphi+\psi), y_A = (R+b) - R_s\cos(\varphi+\psi) \\ x_C = a + R_s\sin(\varphi-\psi), y_C = (R+b) - R_s\cos(\varphi-\psi) \end{cases}$$

(S5) $\beta = \theta_1 - \theta_2 \equiv \theta_1 + \psi \quad (\theta_2 = -\psi)$

(S6) $$\begin{cases} d_0 = \sqrt{(y_B - y_{B'})^2 + (x_B - x_{B'})^2} \\ \begin{cases} x_B &= a - R_s\sin\psi \\ x_{B'} &= \dfrac{1}{(1+m_C^2)}\left[m_C^2 a - m_C b - \sqrt{R^2(1+m_C^2) - (b - m_C a)^2}\right] \end{cases} \\ \begin{cases} y_B &= R + b - R_s\cos\psi \\ y_{B'} &= m_C(x_{B'} - a) + R + b \end{cases} \end{cases}$$

(S7) $$\bar{u}_R(x,y) = \frac{\bar{C}_R(x)}{2\mu} y(d_R(x) - y) + s(1 - y d_R^{-1}(x))$$

$$\text{(S8)} \qquad \bar{C}_R(x) = -6\mu\left(\frac{s}{d_R^2(x)} - \frac{2\dot{m}_R}{\rho d_R^3(x)}\right)$$

$$\text{(S9)} \qquad \triangle p_R = \frac{6\mu}{\tan\beta}\left[s\left(\frac{1}{d_R(L_\beta)} - \frac{1}{d_R(l_\beta)}\right) - \frac{\dot{m}_R}{\rho}\left(\frac{1}{d_R^2(L_\beta)} - \frac{1}{d_R^2(l_\beta)}\right)\right]$$

$$\text{(S10)} \qquad \bar{u}_{\mathcal{L}}(x,y) = \frac{\bar{C}_{\mathcal{L}}(x)}{2\mu}y(d_{\mathcal{L}}(x) - y) - s(1 - yd_{\mathcal{L}}^{-1}(x))$$

$$\text{(S11)} \qquad \bar{C}_{\mathcal{L}}(x) = 6\mu\left(\frac{2\dot{m}_{\mathcal{L}}}{\rho d_{\mathcal{L}}^3(x)} + \frac{s}{d_{\mathcal{L}}^2(x)}\right)$$

$$\text{(S12)} \qquad \triangle p_{\mathcal{L}} = \frac{6\mu}{\tan\beta}\left[s\left(\frac{1}{d_{\mathcal{L}}(L_\beta)} - \frac{1}{d_{\mathcal{L}}(l_\beta)}\right) + \frac{\dot{m}_{\mathcal{L}}}{\rho}\left(\frac{1}{d_{\mathcal{L}}^2(L_\beta)} - \frac{1}{d_{\mathcal{L}}^2(l_\beta)}\right)\right]$$

$$\text{(S13)} \qquad \frac{\dot{m}_R}{\rho} = s\lambda_R + \frac{\tan\beta}{6\mu}\delta_R\triangle p^R$$

$$\text{(S14)} \qquad \frac{\dot{m}_{\mathcal{L}}}{\rho} = -s\lambda_{\mathcal{L}} - \frac{\tan\beta}{6\mu}\delta_{\mathcal{L}}\triangle p^{\mathcal{L}}$$

$$\text{(S15)} \qquad \tilde{p}_R = p_{sh} - \left(\frac{w_{sh}}{n_c}\right)\frac{8\mu\tilde{l}_{eff}}{\pi\tilde{R}_{eff}^4}\left(\frac{\dot{m}_R}{\rho}\right) = p_{atm} + \frac{6\mu}{(\tan\beta)\delta_R}\left[\frac{\dot{m}_R}{\rho} - s\lambda_R\right]$$

$$\text{(S16)} \qquad \tilde{p}_{\mathcal{L}} = p_{sh} - \left(\frac{w_{sh}}{n_c}\right)\frac{8\mu\tilde{l}_{eff}}{\pi\tilde{R}_{eff}^4}\left(\frac{\dot{m}_{\mathcal{L}}}{\rho}\right) = p_{atm} - \frac{6\mu}{(\tan\beta)\delta_{\mathcal{L}}}(s\lambda_{\mathcal{L}} + \frac{\dot{m}_{\mathcal{L}}}{\rho})$$

$$\text{(S17)} \qquad \frac{\dot{m}_R}{\rho} = \frac{(p_{sh} - p_{atm}) + \frac{6\mu s}{\tan\beta}(\frac{\lambda_R}{\delta_R})}{\left[\frac{6\mu}{(\tan\beta)\delta_R} + \left(\frac{w_{sh}}{n_c}\right)\frac{8\mu\tilde{l}_{eff}}{\pi\tilde{R}_{eff}^4}\right]}$$

(S18) $$\frac{\dot{m}_{\mathcal{L}}}{\rho} = \frac{(p_{sh} - p_{atm}) + \frac{6\mu s}{\tan\beta}(\frac{\lambda_{\mathcal{L}}}{\delta_{\mathcal{L}}})}{\left[\left(\frac{w_{sh}}{n_c}\right)\frac{8\mu\tilde{l}_{eff}}{\pi\tilde{R}^4_{eff}} - \frac{6\mu}{(\tan\beta)\delta_{\mathcal{L}}}\right]}$$

(S19) $$\tilde{N}^R_{sh} = \frac{6\mu s}{\tan^2\beta}\ln\left[\frac{d_R(L_\beta)}{d_R(l_\beta)}\right] + \frac{6\mu s}{\tan\beta}\cdot\frac{(L_\beta - l_\beta)}{d_R(l_\beta)} - \frac{6\mu}{\tan^2\beta}\left(\frac{\dot{m}_R}{\rho}\right)\left[\frac{1}{d_R(l_\beta)} - \frac{1}{d_R(L_\beta)}\right]$$
$$-\frac{6\mu}{\tan\beta}\left(\frac{\dot{m}_R}{\rho}\right)\frac{(L_\beta - l_\beta)}{d^2_R(l_\beta)} = -\tilde{N}^R_{sl}$$

(S20) $$\tilde{N}^R_{sh} = -\tilde{N}^R_{sl} \equiv \tilde{p}_R \cdot w_{rec}$$

(S21) $$\tilde{N}^{\mathcal{L}}_{sh} = -\frac{6\mu s}{\tan^2\beta}\ln\left[\frac{d_{\mathcal{L}}(L_\beta)}{d_{\mathcal{L}}(l_\beta)}\right] + \frac{6\mu s}{\tan\beta}\cdot\frac{(L_\beta - l_\beta)}{d_{\mathcal{L}}(l_\beta)} + \frac{6\mu}{\tan^2 p}\left(\frac{\dot{m}_{\mathcal{L}}}{\rho}\right)\left[\frac{1}{d_{\mathcal{L}}(L_\beta)} - \frac{1}{d_{\mathcal{L}}(l_\beta)}\right]$$
$$+\frac{6\mu}{\tan\beta}\left(\frac{\dot{m}_{\mathcal{L}}}{\rho}\right)\frac{(L_\beta - l_\beta)}{d^2_{\mathcal{L}}(l_\beta)} = -\tilde{N}^{\mathcal{L}}_{sl}$$

(S22) $$\tilde{N}^{\mathcal{L}}_{sh} = -\tilde{N}^{\mathcal{L}}_{sl} \equiv \tilde{p}_{\mathcal{L}} \cdot w_{rec}$$

(S23) $$p_c(x) = \left(\frac{\tilde{p}_R - \tilde{p}_{\mathcal{L}}}{2l_c}\right)x + \left(\frac{\tilde{p}_R + \tilde{p}_{\mathcal{L}}}{2}\right), -l_c \leq x \leq l_c$$

(S24) $$\overset{c}{N}{}^{R}_{sh} = \left(\frac{\tilde{p}_R - \tilde{p}_{\mathcal{L}}}{4}\right)l_c = -\overset{c}{N}{}^{R}_{sl}$$

(S25) $$\overset{c}{N}{}^{\mathcal{L}}_{sh} = \left(\frac{\tilde{p}_R - \tilde{p}_{\mathcal{L}}}{4}\right)l_c = -\overset{c}{N}{}^{\mathcal{L}}_{sl}$$

(S26) $$\tilde{T}^R_{sl} = \frac{6\mu}{\tan\beta}\left(\frac{\dot{m}_R}{\rho}\right)\left[\frac{1}{d_R(L_\beta)} - \frac{1}{d_R(l_\beta)}\right] + \frac{2\mu s}{\tan\beta}\ln\left[\frac{d_R(L_\beta)}{d_R(l_\beta)}\right]$$

(S27) $$\tilde{\mathcal{T}}_{sl}^{R} = \frac{6\mu}{\tan\beta}\left(\frac{\dot{m}_R}{\rho}\right)\left[\frac{1}{d_R(l_\beta)} - \frac{1}{d_R(L_\beta)}\right] + \frac{4\mu s}{\tan\beta}\ln\left[\frac{d_R(l_\beta)}{d_R(L_\beta)}\right]$$

(S28) $$\tilde{\mathcal{T}}_{sh}^{\mathcal{L}} = \frac{6\mu}{\tan\beta}\left(\frac{\dot{m}_\mathcal{L}}{\rho}\right)\left[\frac{1}{d_\mathcal{L}(l_\beta)} - \frac{1}{d_\mathcal{L}(L_\beta)}\right] + \frac{2\mu s}{\tan\beta}\ln\left[\frac{d_\mathcal{L}(L_\beta)}{d_\mathcal{L}(l_\beta)}\right]$$

(S29) $$\tilde{\mathcal{T}}_{sl}^{\mathcal{L}} = \frac{6\mu}{\tan\beta}\left(\frac{\dot{m}_\mathcal{L}}{\rho}\right)\left[\frac{1}{d_\mathcal{L}(L_\beta)} - \frac{1}{d_\mathcal{L}(l_\beta)}\right] + \frac{4\mu s}{\tan\beta}\ln\left[\frac{d_\mathcal{L}(l_\beta)}{d_\mathcal{L}(L_\beta)}\right]$$

(S30) $$\tilde{\mathcal{T}}_{sh}^{R} = \tilde{\mathcal{T}}_{sh}^{\mathcal{L}} = 0$$

(S31) $$u_R^{rec} = s(1 - y d_R^{-1}(x)), l_c \leq x \leq l_\beta$$

(S32) $$u_\mathcal{L}^{rec} = -s(1 - y d_\mathcal{L}^{-1}(x)), l_c \leq x \leq l_\beta$$

(S33) $$\tilde{\mathcal{T}}_{sl}^{R} = \frac{\mu s}{\tan\beta}\ln\left[\frac{d_R(l_c)}{d_R(l_\beta)}\right]$$

(S34) $$\tilde{\mathcal{T}}_{sl}^{\mathcal{L}} = \frac{\mu s}{\tan\beta}\ln\left[\frac{d_\mathcal{L}(l_\beta)}{d_\mathcal{L}(l_c)}\right]$$

(S35) $$u_R^c(x,y) = \left(\frac{\tilde{p}_\mathcal{L} - \tilde{p}_R}{4\mu l_c}\right) y(d_R(x) - y) + s(1 - y d_R^{-1}(x)), 0 \leq x \leq l_c$$

(S36) $$u_\mathcal{L}^c(x,y) = \left(\frac{\tilde{p}_R - \tilde{p}_\mathcal{L}}{4\mu l_c}\right) y(d_\mathcal{L}(x) - y) - s(1 - y d_\mathcal{L}^{-1}(x)), 0 \leq x \leq l_c$$

(S37) $$\begin{cases} u^c(x,y) = \left(\dfrac{\tilde{p}_\mathcal{L} - \tilde{p}_R}{4\mu l_c}\right) y(d_R(x) - y) + s(1 - y d^{-1}(x)), -l_c \leq x \leq l_c \\ d(x) = d_0 - x\tan\beta \end{cases}$$

$$\text{(S38)}\qquad \overset{c}{\mathcal{T}}{}^{R}_{sh} = \frac{\mu s}{\tan\beta}\ln\left[\frac{d_0}{d_R(l_c)}\right] - \left(\frac{\tilde{p}_R - \tilde{p}_{\mathcal{L}}}{4l_c}\right)(d_0 l_c - \frac{l_c^2}{2}\tan\beta)$$

$$\text{(S39)}\qquad \overset{c}{\mathcal{T}}{}^{\mathcal{L}}_{sh} = -\frac{\mu s}{\tan\beta}\ln\left[\frac{d_{\mathcal{L}}(l_c)}{d_0}\right] - \left(\frac{\tilde{p}_R - \tilde{p}_{\mathcal{L}}}{4l_c}\right)(d_0 l_c - \frac{l_c^2}{2}\tan\beta)$$

$$\text{(S40)}\qquad \overset{c}{\mathcal{T}}_{sh} = \overset{c}{\mathcal{T}}{}^{R}_{sh} + \overset{c}{\mathcal{T}}{}^{\mathcal{L}}_{sh} \equiv \left(\frac{\tilde{p}_{\mathcal{L}} - \tilde{p}_R}{2}\right) d_0 + \frac{\mu s}{\tan\beta}\ln\left[\frac{d_R(-l_c)}{d_R(l_c)}\right]$$

$$\text{(S41)}\qquad \overset{c}{\mathcal{T}}{}^{R}_{sl} = \frac{1}{4l_c}(\tilde{p}_R - \tilde{p}_{\mathcal{L}})[d_0 l_c - \frac{l_c^2}{2}\tan\beta] - \frac{\mu s}{\tan\beta}\ln\left[\frac{d_R(l_c)}{d_0}\right]$$

$$\text{(S42)}\qquad \overset{c}{\mathcal{T}}{}^{\mathcal{L}}_{sl} = -\frac{1}{4l_c}(\tilde{p}_R - \tilde{p}_{\mathcal{L}})[d_0 l_c + \frac{l_c^2}{2}\tan\beta] - \frac{\mu s}{\tan\beta}\ln\left[\frac{d_{\mathcal{L}}(l_c)}{d_0}\right]$$

$$\text{(S43)}\qquad \overset{c}{\mathcal{T}}_{sl} = \overset{c}{\mathcal{T}}{}^{R}_{sl} + \overset{c}{\mathcal{T}}{}^{\mathcal{L}}_{sl} \equiv \tfrac{1}{2}(\tilde{p}_R - \tilde{p}_{\mathcal{L}})d_0 + \frac{\mu s}{\tan\beta}\ln\left[\frac{d_R(-l_c)}{d_R(l_c)}\right]$$

$$\text{(S44)}\qquad \mathcal{T}_{sl}^{net} = \frac{6\mu}{\tan\beta}\left(\frac{\dot{m}_R}{\rho}\right)\left[\frac{1}{d_R(l_\beta)} - \frac{1}{d_R(L_\beta)}\right] + \frac{6\mu}{\tan\beta}\left(\frac{\dot{m}_{\mathcal{L}}}{\rho}\right)\left[\frac{1}{d_{\mathcal{L}}(l_\beta)} - \frac{1}{d_{\mathcal{L}}(L_\beta)}\right]$$
$$+\frac{4\mu s}{\tan\beta}\left(\ln\left[\frac{d_R(l_\beta)}{d_R(L_\beta)}\right] + \ln\left[\frac{d_{\mathcal{L}}(L_\beta)}{d_{\mathcal{L}}(l_\beta)}\right]\right) + \frac{\mu s}{\tan\beta}\left(\ln\left[\frac{d_R(l_c)}{d_R(l_\beta)}\right] + \ln\left[\frac{d_{\mathcal{L}}(l_\beta)}{d_{\mathcal{L}}(l_c)}\right]\right)$$
$$+\tfrac{1}{2l_c}(\tilde{p}_R - \tilde{p}_{\mathcal{L}})d_0 l_c + \frac{\mu s}{\tan\beta}\ln\left[\frac{d_R(-l_c)}{d_R(l_c)}\right]$$

$$\text{(S45)}\qquad \tan\eta_R = \frac{\cos\psi - \cos(\varphi - \psi)}{\sin(\varphi - \psi) + \sin\psi}$$

$$\text{(S46)}\qquad \tan\eta_{\mathcal{L}} = \frac{\cos\psi - \cos(\varphi - \psi)}{\sin(\varphi - \psi) - \sin\psi}$$

(S47) $$V_{sh} = \bar{N}^R_{sh}\cos\eta_R + \tilde{N}^R_{sh}\cos\psi + \overset{c}{N}{}^R_{sh}\cos\eta_R + \bar{T}^R_{sh}\sin\eta_R + \overset{c}{T}{}^R_{sh}\sin\eta_R + \bar{N}^{\mathcal{L}}_{sh}\cos\eta_{\mathcal{L}} + \tilde{N}^{\mathcal{L}}_{sh}\cos\psi + \overset{c}{N}{}^{\mathcal{L}}_{sh}\cos\eta_{\mathcal{L}} - \bar{T}^{\mathcal{L}}_{sh}\sin\eta_{\mathcal{L}} - \overset{c}{T}{}^{\mathcal{L}}_{sh}\sin\eta_{\mathcal{L}}$$

(S48) $$H_{sh} = -\bar{N}^R_{sh}\sin\eta_R + \tilde{N}^R_{sh}\sin\psi - \overset{c}{N}{}^R_{sh}\sin\eta_R + \bar{T}^R_{sh}\cos\eta_R + \overset{c}{T}{}^R_{sh}\cos\eta_R + \bar{N}^{\mathcal{L}}_{sh}\sin\eta_{\mathcal{L}} - \tilde{N}^{\mathcal{L}}_{sh}\sin\psi + \overset{c}{N}{}^{\mathcal{L}}_{sh}\sin\eta_{\mathcal{L}} + \bar{T}^{\mathcal{L}}_{sh}\cos\eta_{\mathcal{L}} + \overset{c}{T}{}^{\mathcal{L}}_{sh}\cos\eta_{\mathcal{L}}$$

(S49) $$V_F = -F\cos\psi, H_F = -F\sin\psi$$

(S50) $$V_W = -W, H_W = 0$$

(S51) $$H_s = -2k_s(l^* - \hat{l})$$

(S52) $$H_{sh} + H_F + H_s - H_{PV} = 0$$

(S53) $$V_{sh} + V_F + V_W = 0$$

(S54) $$M_{sh} = \tfrac{1}{2}(L_{rec} + L_T)(\bar{N}^{\mathcal{L}}_{sh} - \bar{N}^R_{sh}) + d_{rec}(\tilde{N}^{\mathcal{L}}_{sh} - \tilde{N}^R_{sh}) + \tfrac{1}{2}L_c(\overset{c}{N}{}^{\mathcal{L}}_{sh} - \overset{c}{N}{}^R_{sh})$$

(S55) $$M_W = W\tilde{d}\sin\psi$$

(S56) $$M_{PV} = -H_{PV}\cdot d_{PV}$$

(S57) $$d_{PV} = R_s\cos\psi - \alpha\cos\psi - \beta\sin\psi - \tan(\delta+\psi)\left\{\frac{\hat{l}}{\cos\psi(1+\tan\psi\cdot\tan(\delta+\psi))}\right\}$$

(S58) $$M_{sh} + M_W + M_{PV} = 0$$

(S59) $$\mathcal{P} = \{F, s, p_{sh} - p_{atm}, R, \phi, R_s, \tilde{R}_{eff}, \tilde{l}_{eff}; \mu, \rho\}$$

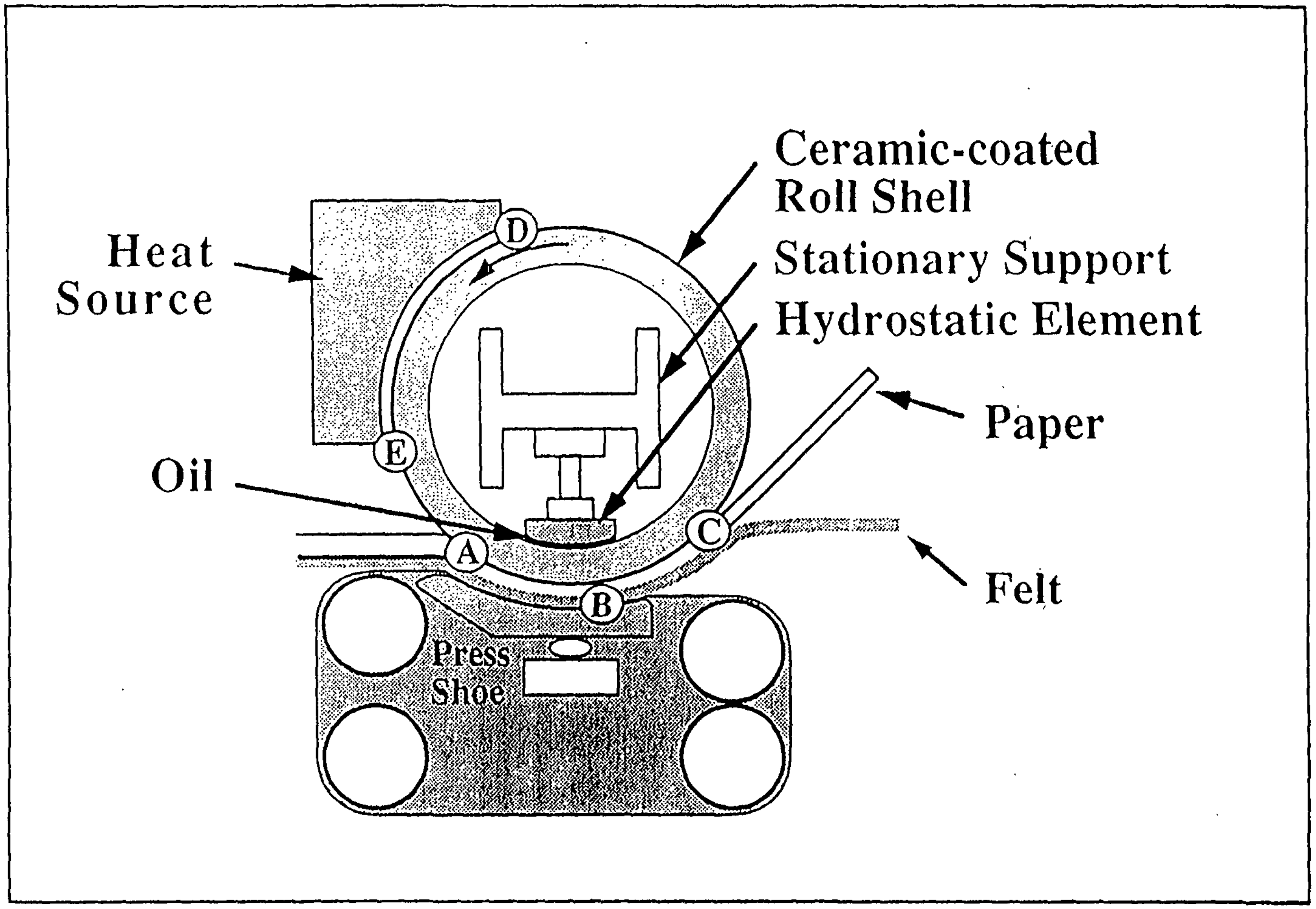

Figure 1 . The Crown Compensated Impulse Drying Press Roll (not shown to scale).

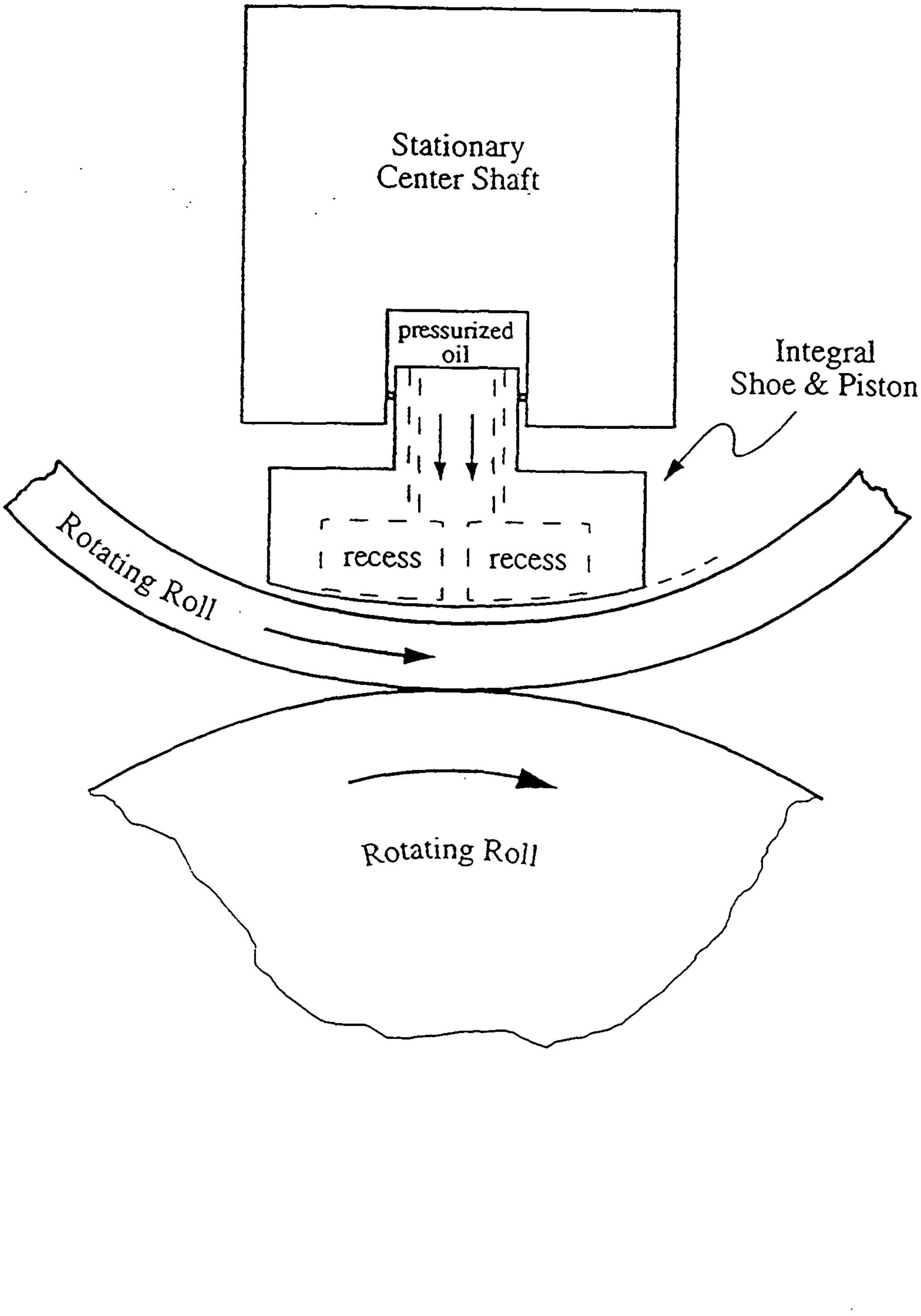

Figure 2. Cross sectional view of the shoe and the rotating shell.

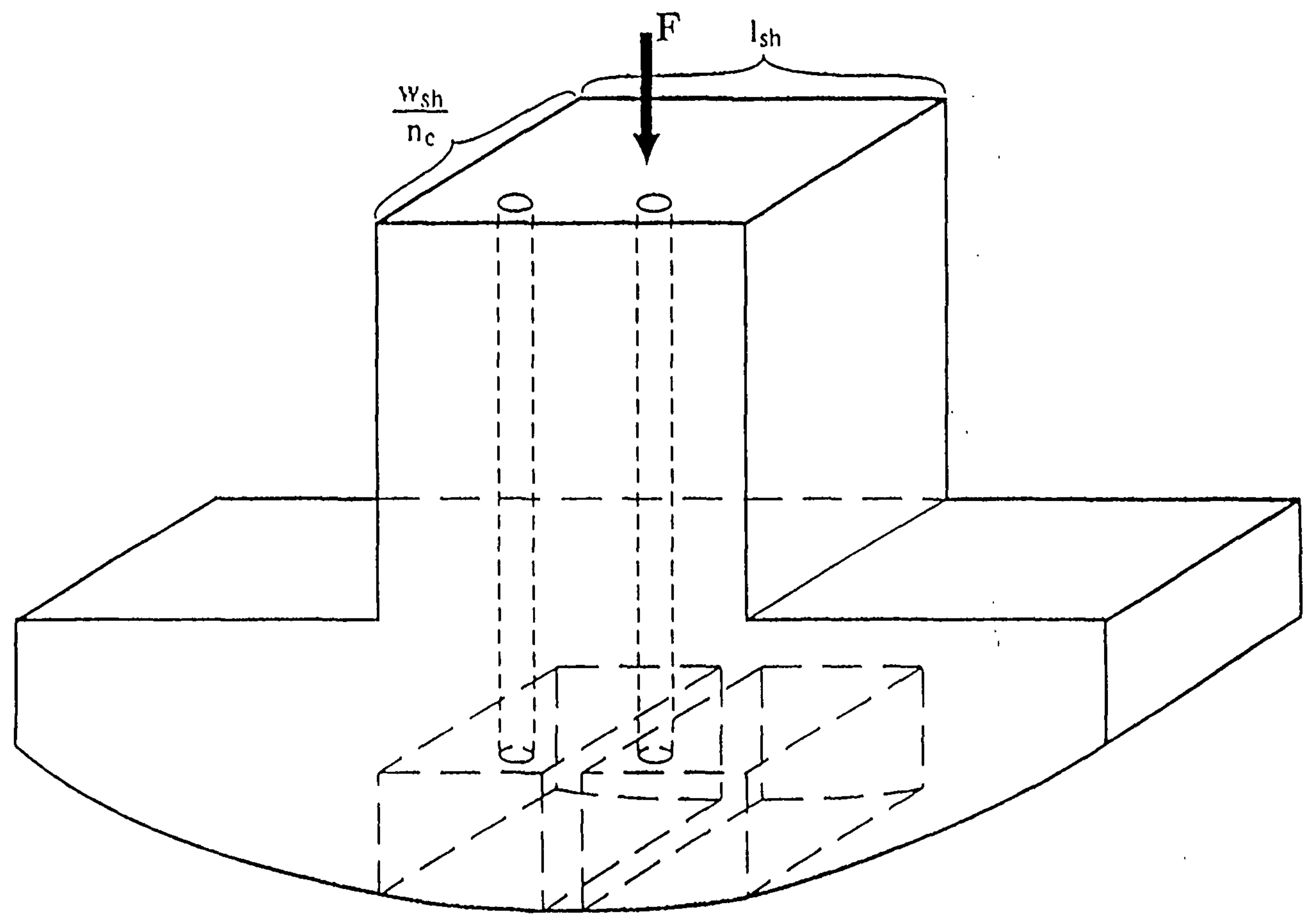

Figure 3.Shoe cross section depicting capillaries entering the recesses (not shown to scale.)

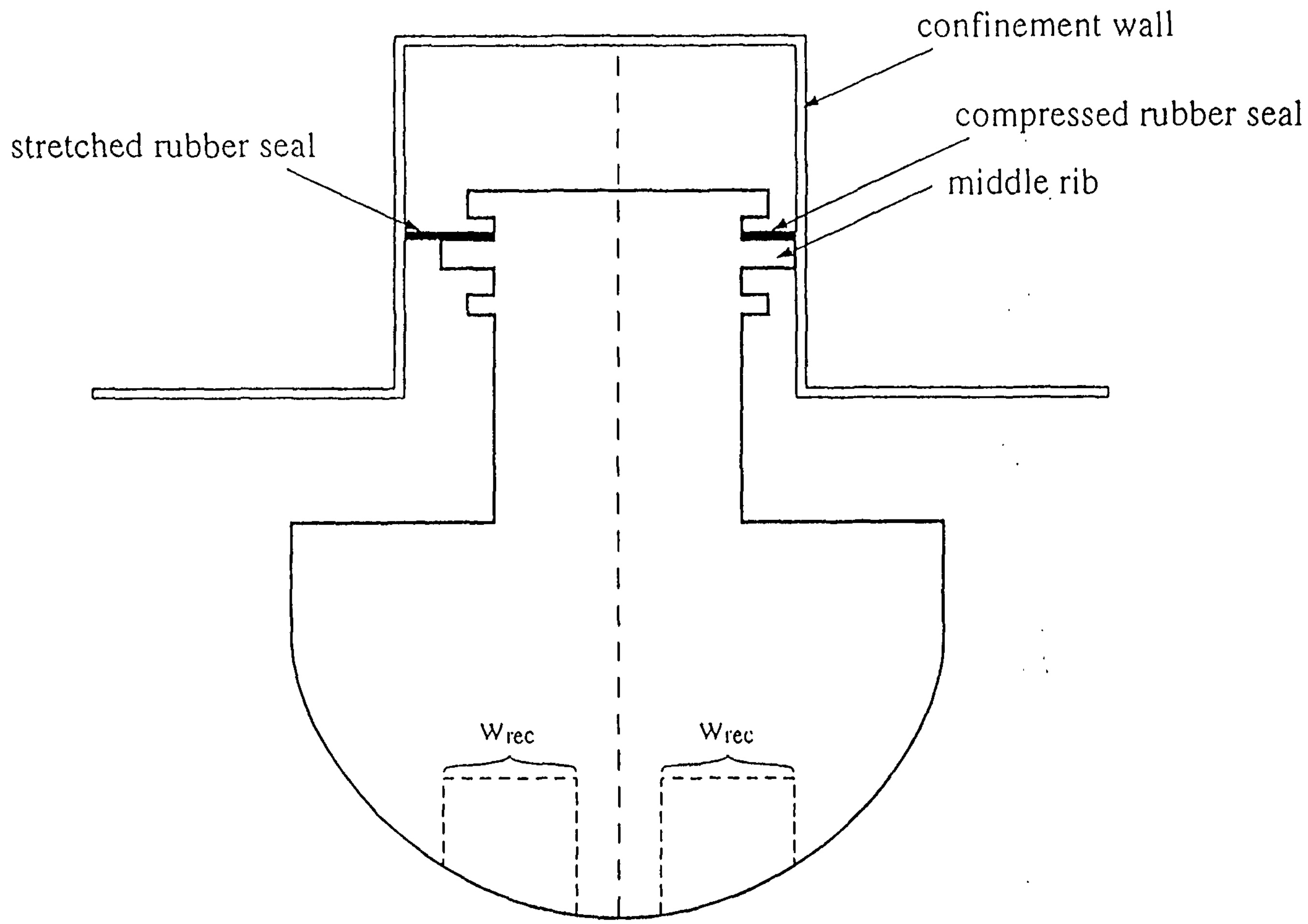

Figure 4. Contact between the shaft of the hydrostatic shoe and the wall of the confinement.

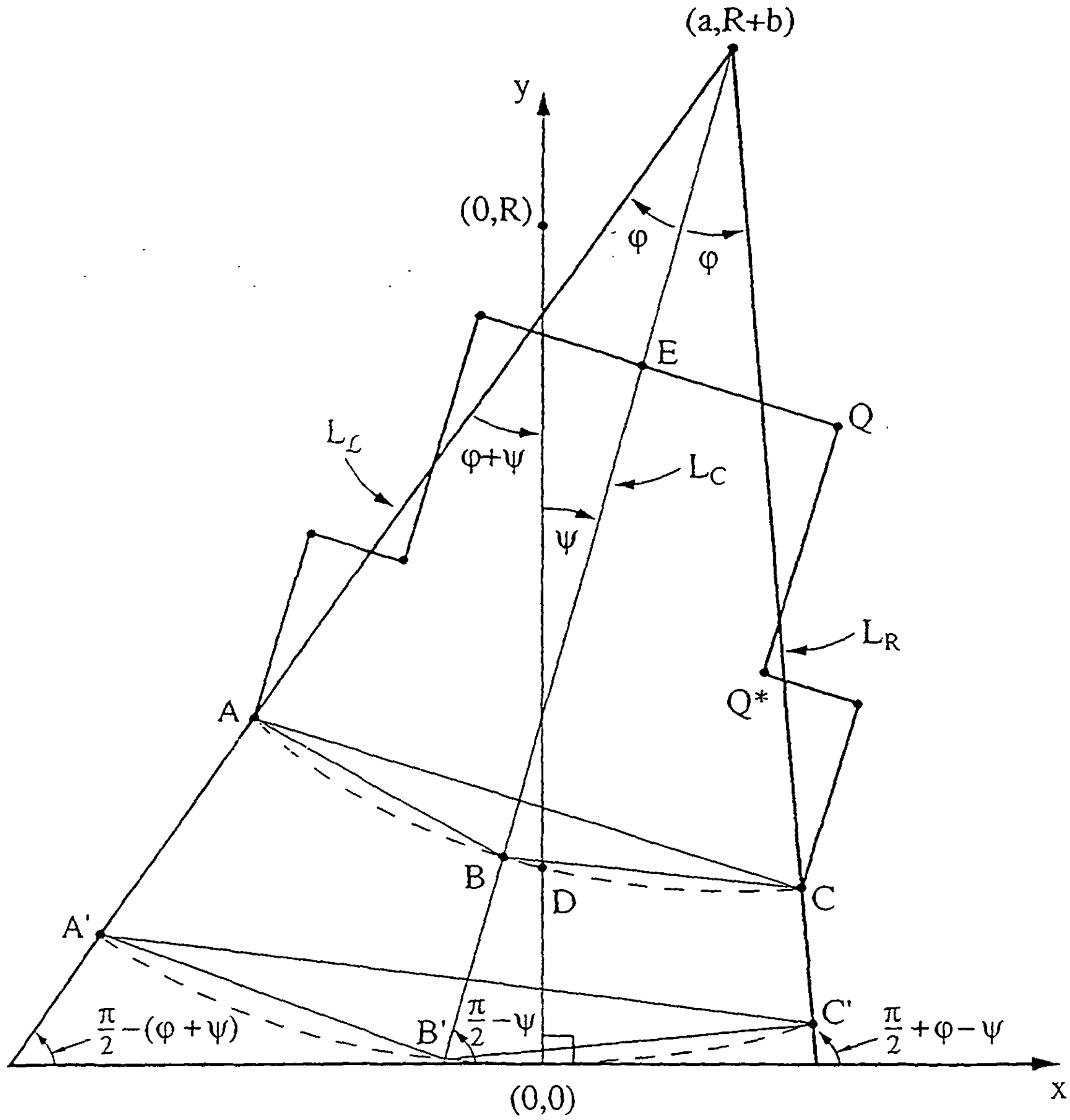

Figure 5. Motion of the hydrostatic shoe.

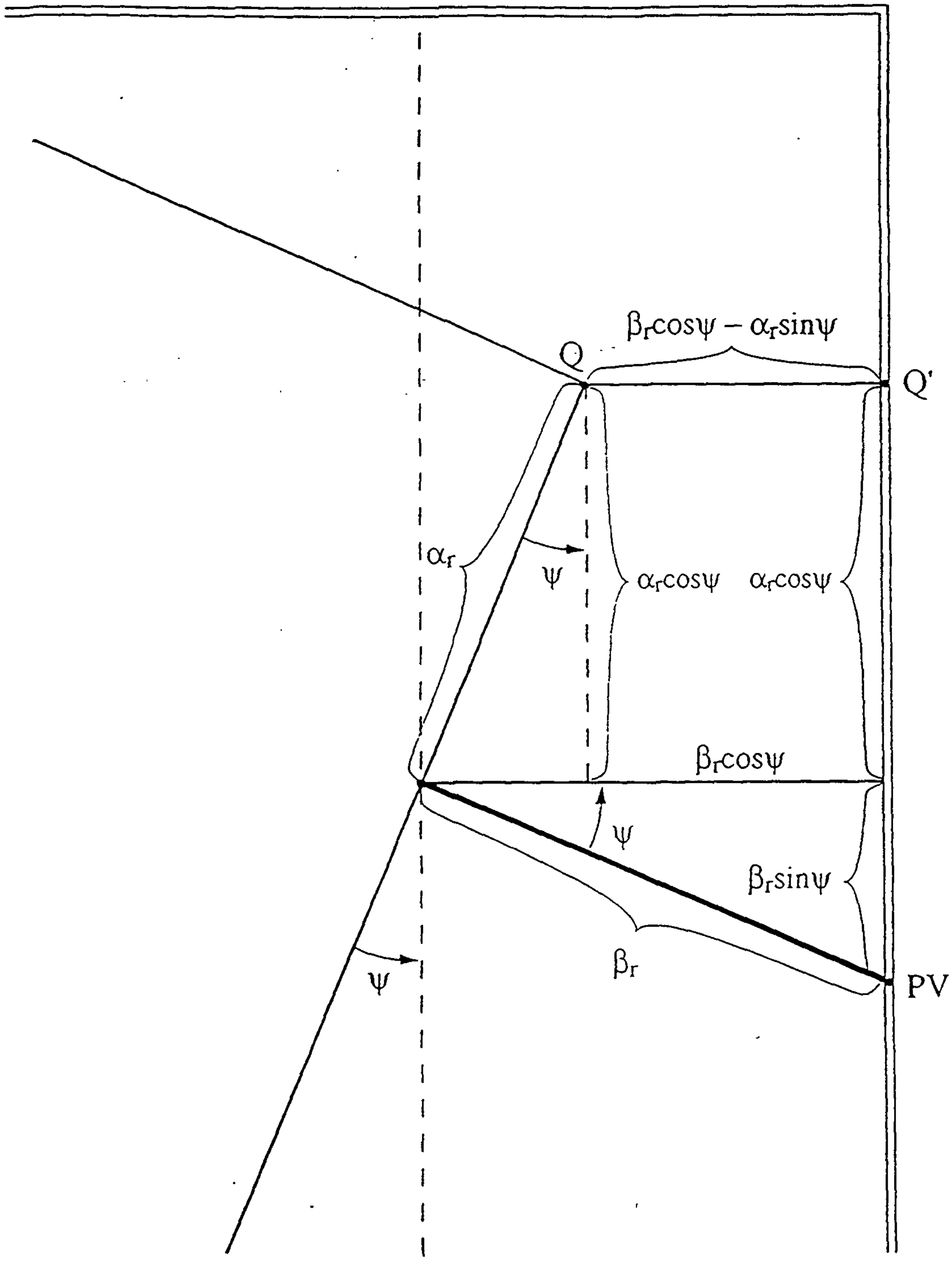

Figure 6. Geometry for the pivoting of the shaft of the hydrostatic shoe.

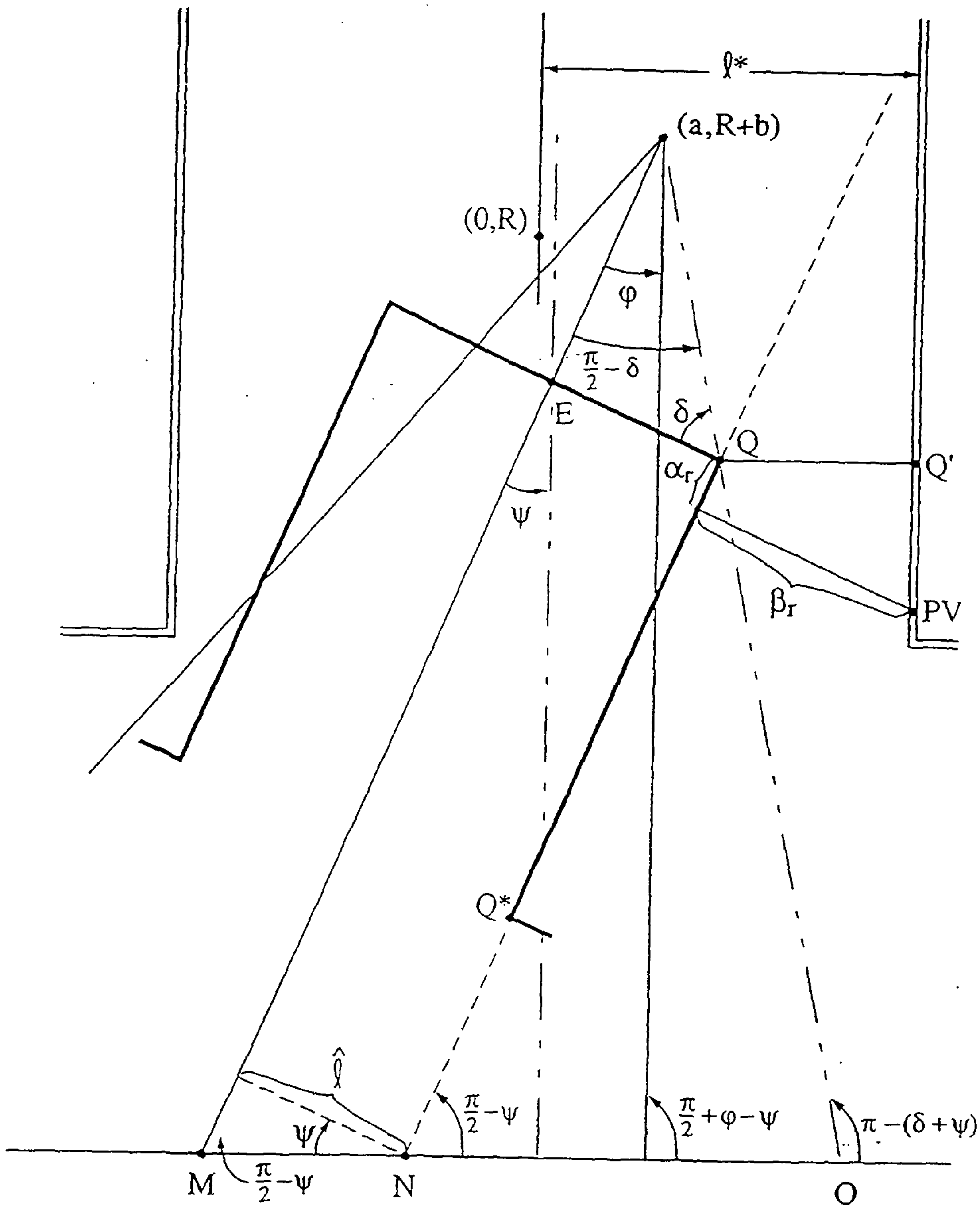

Figure 7. Determination of the coordinates of the pivot point along the wall of the confinement shaft.

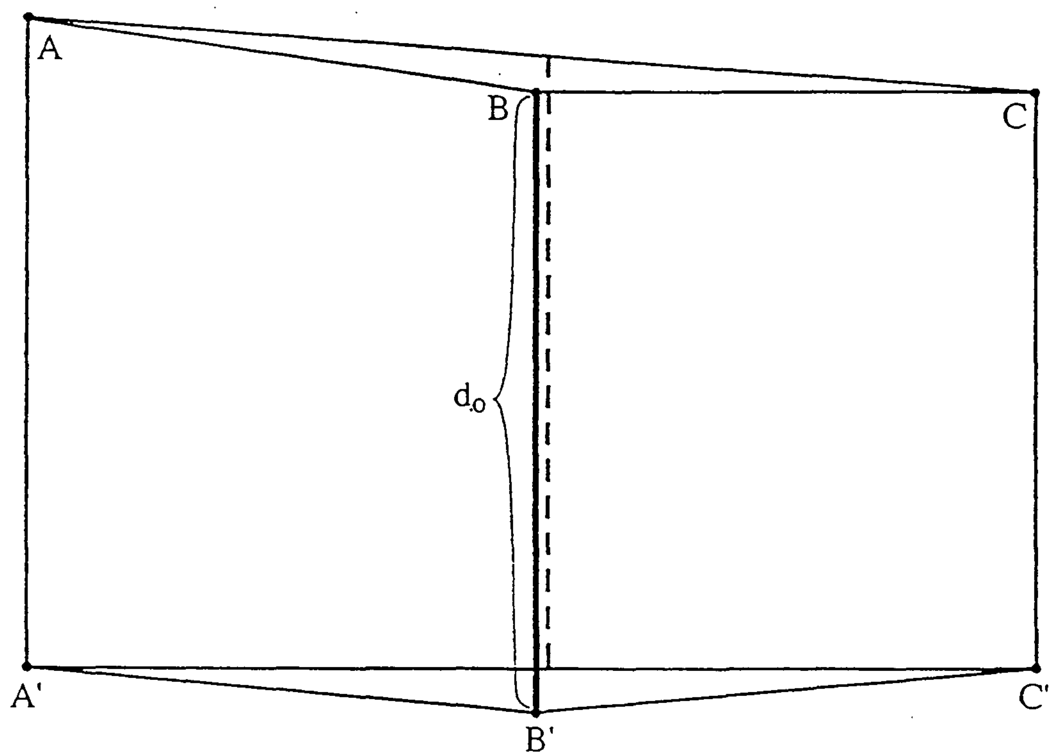

Figure 8. Approximate geometry of the lubrication channel.

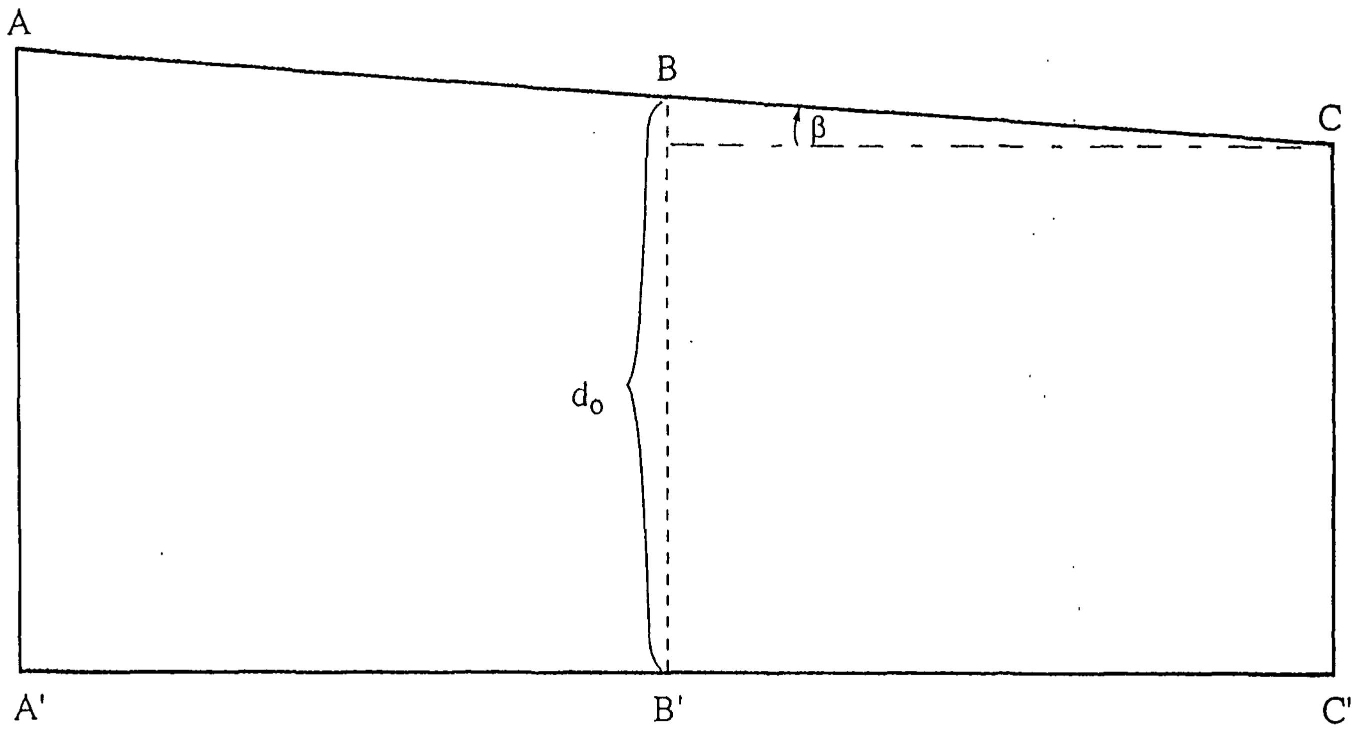

Figure 9. The approximate wedge-shaped bearing.

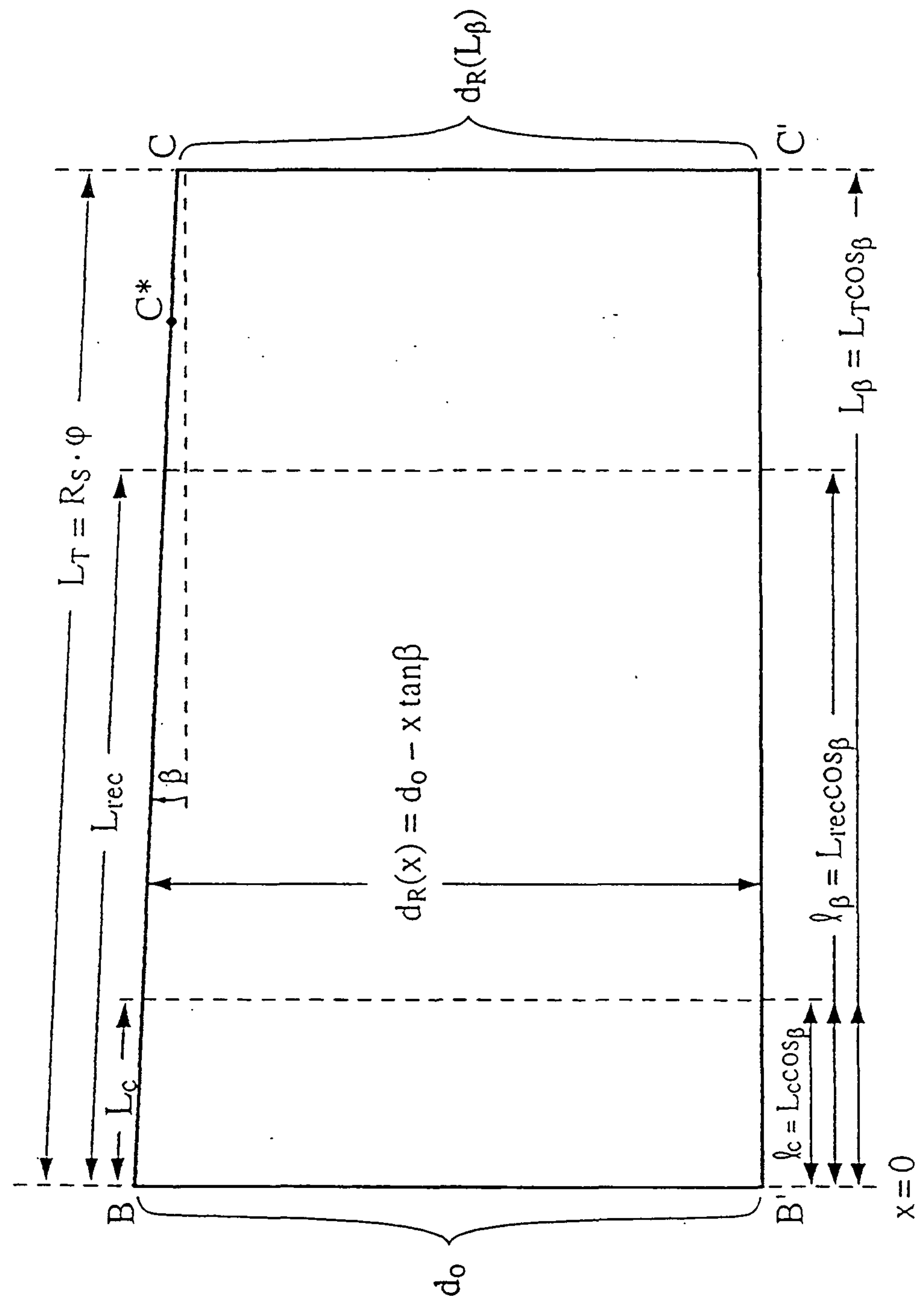

Figure 10a. The right-hand subchannel.

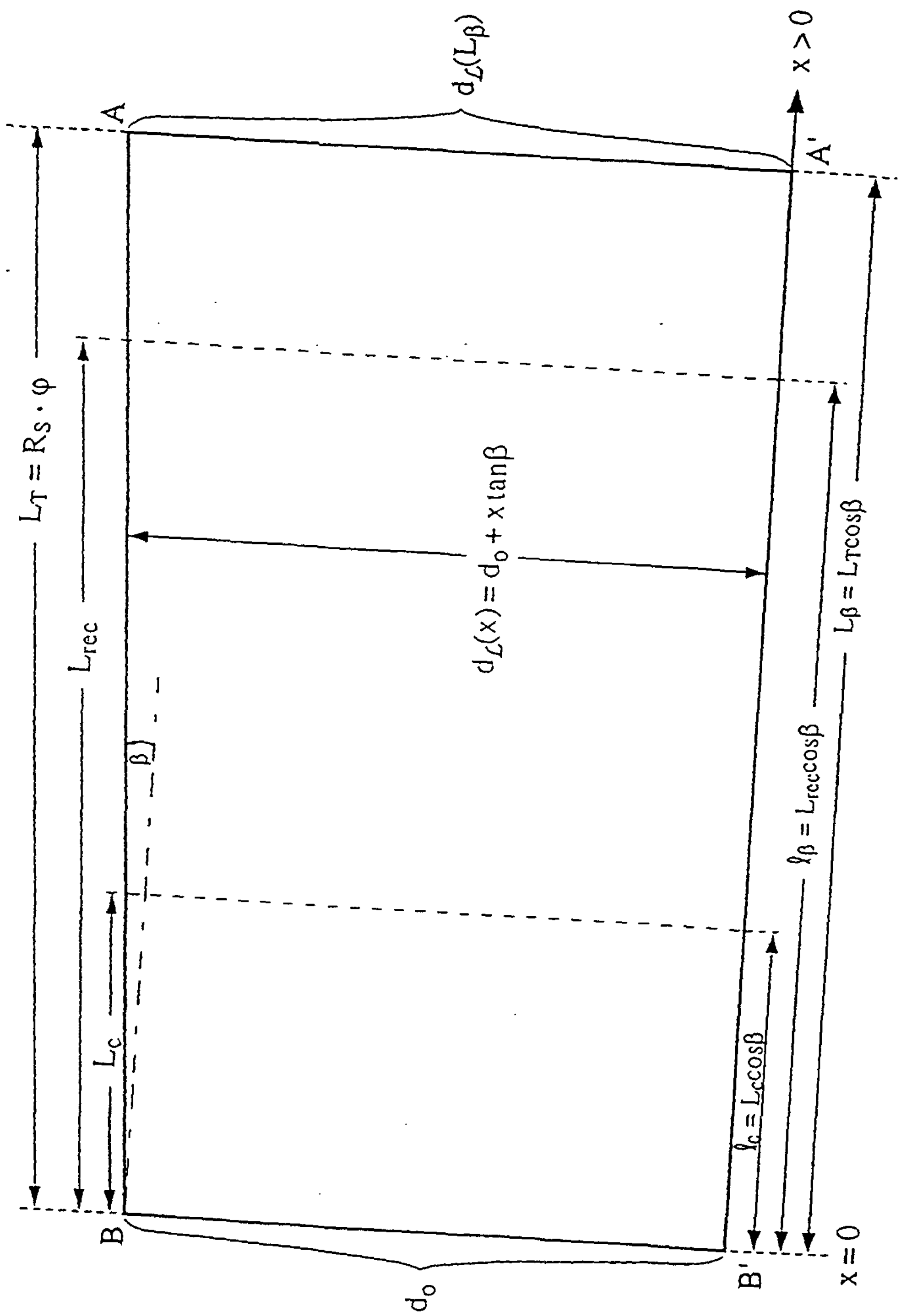

Figure 10b. The left-hand subchannel.

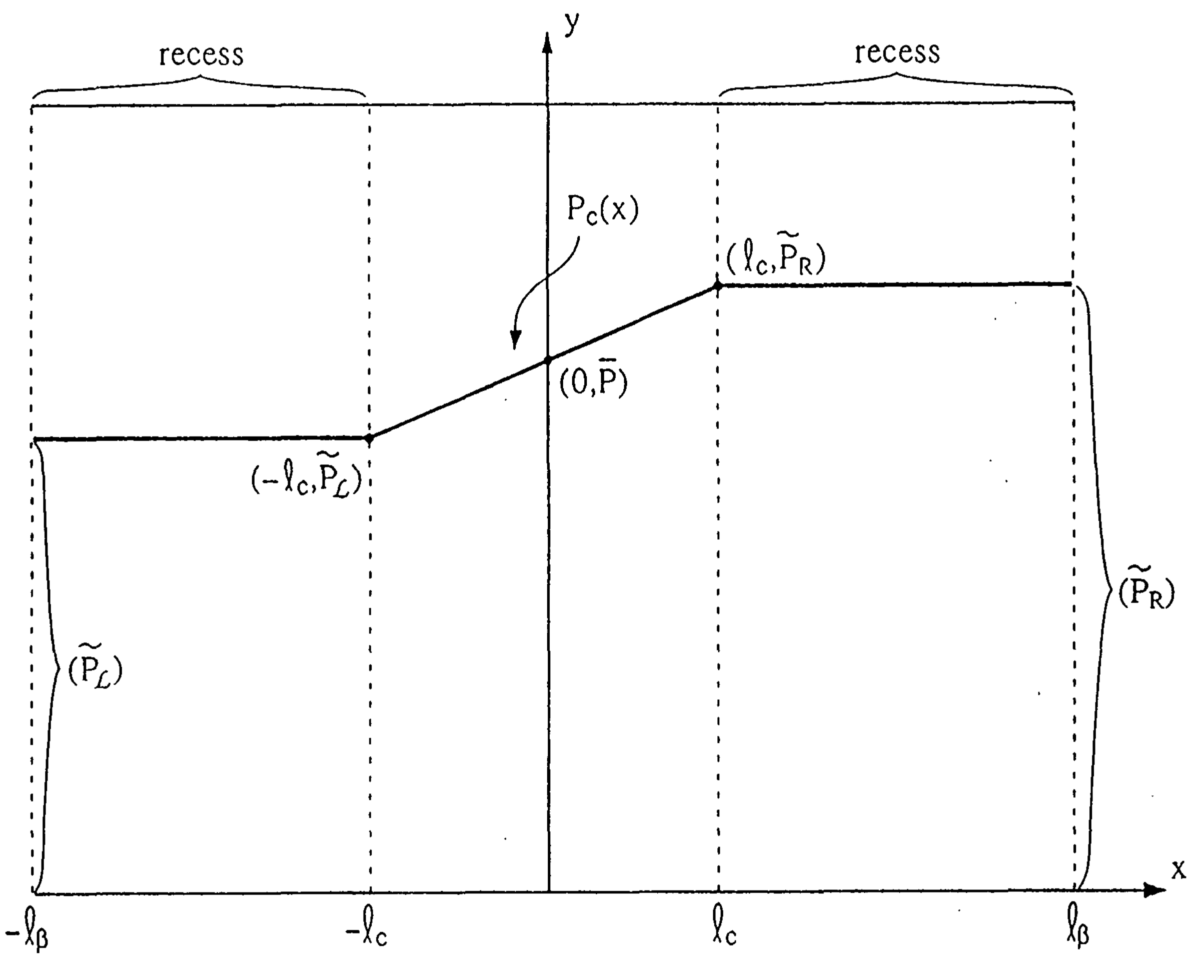

Figure 11. Pressure distribution under the recesses and in the middle channel.

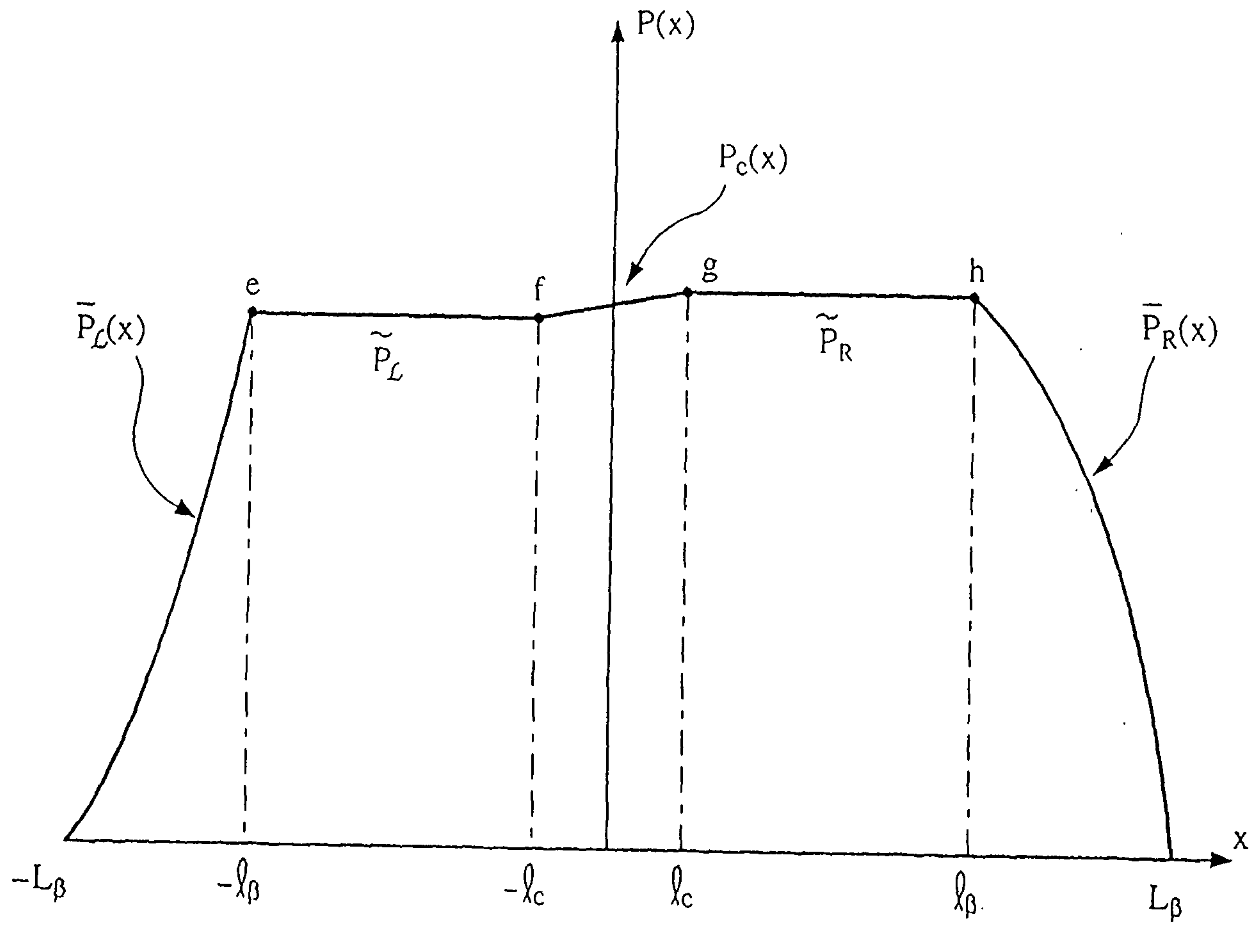

Figure 12. Pressure distribution under the internal hydrostatic shoe.

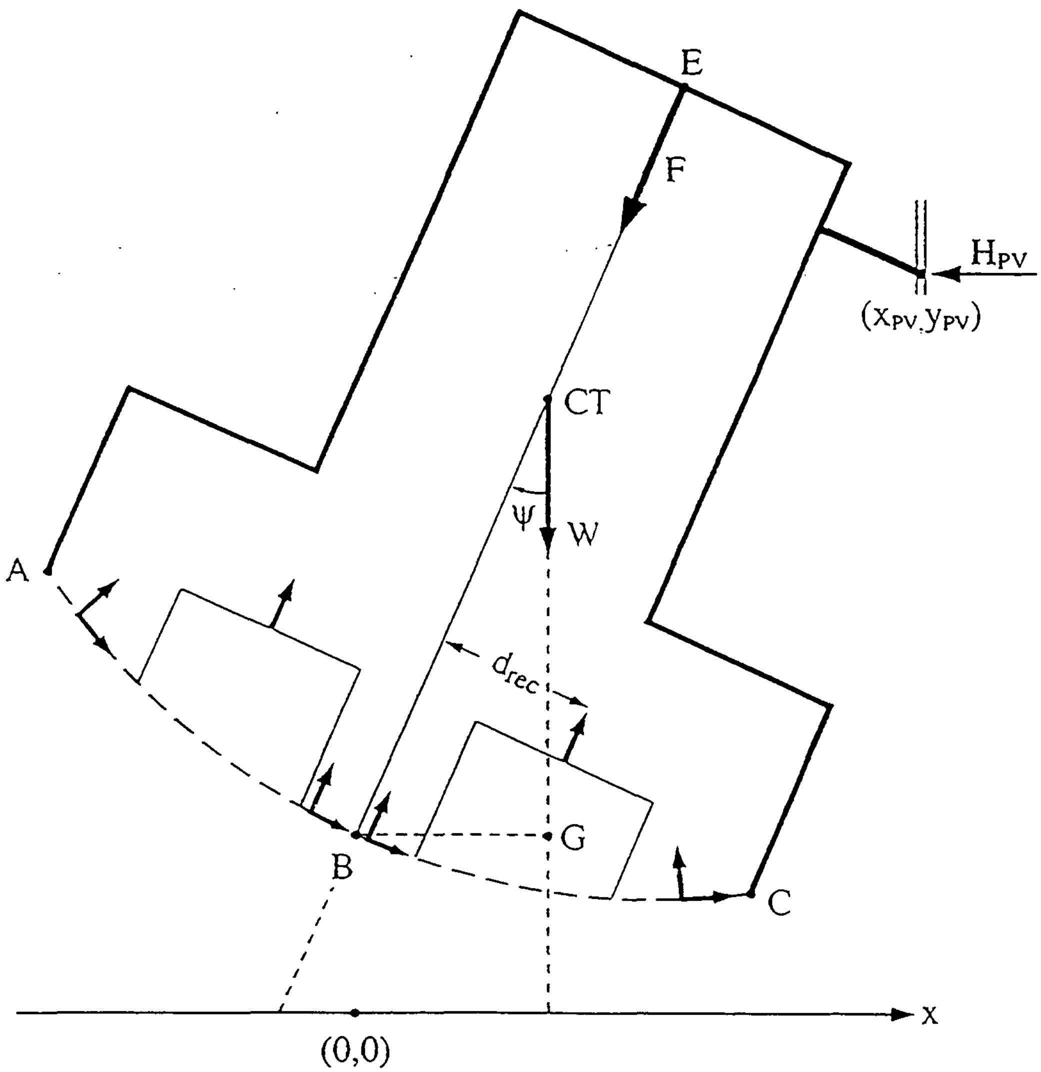

Figure 13. Forces acting on the internal hydrostatic shoe.

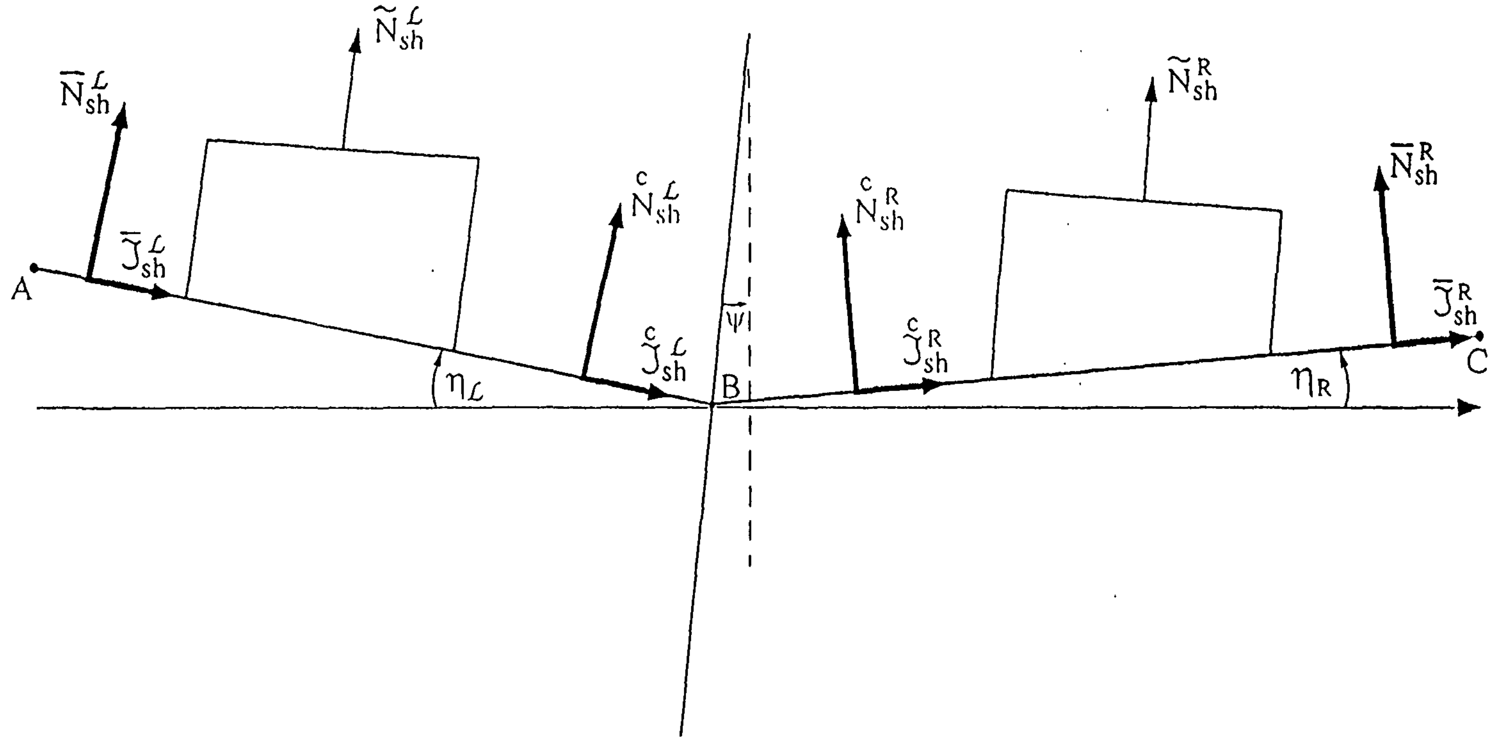

Figure 14. Forces acting on the bottom surface of the shoe.

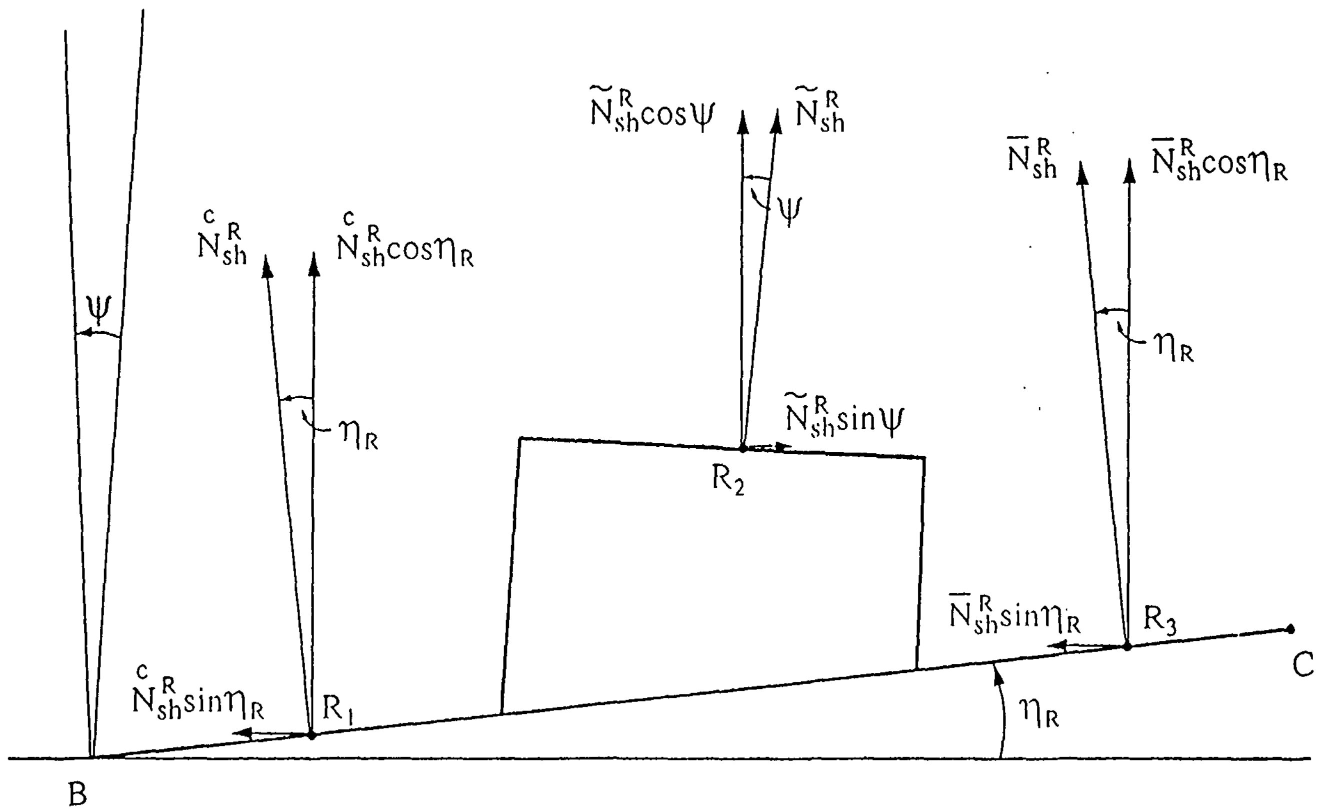

Figure 15a. Resolution of the normal forces acting on the bottom surface of the shoe in the right-hand subchannel.

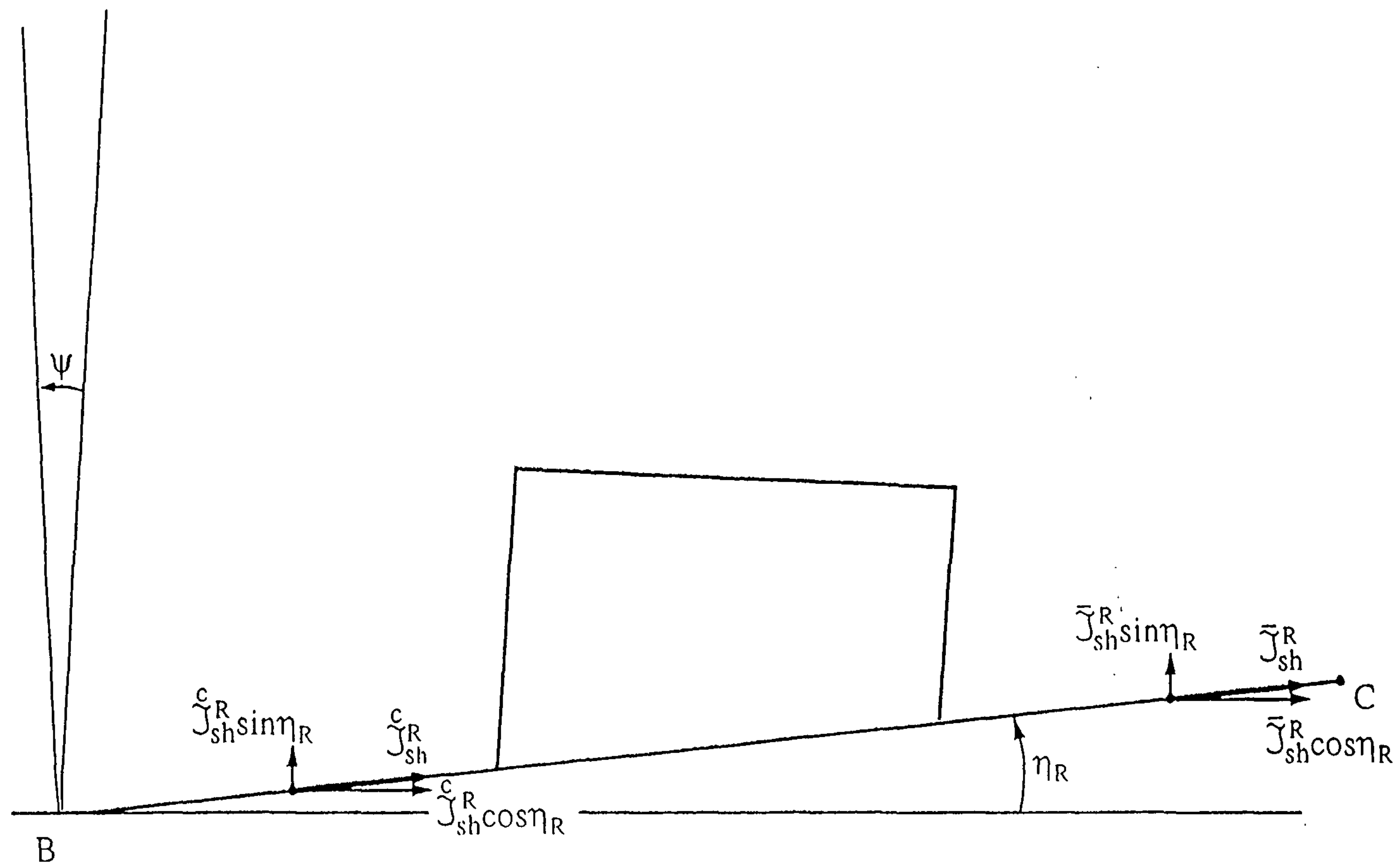

Figure 15b. Resolution of the tangential forces acting on the bottom surface of the shoe in the right-hand subchannel.

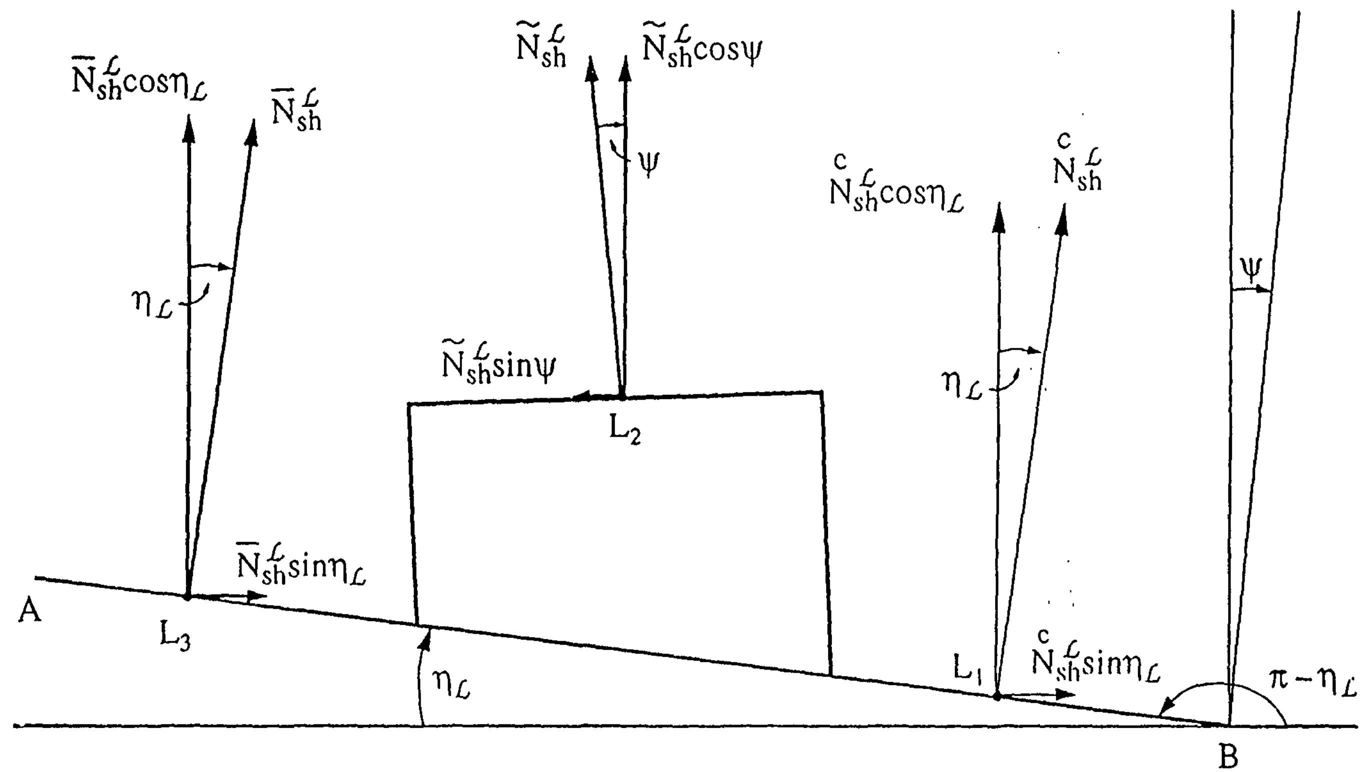

Figure 16a. Resolution of the normal forces acting on the bottom surface of the shoe in the left-hand subchannel.

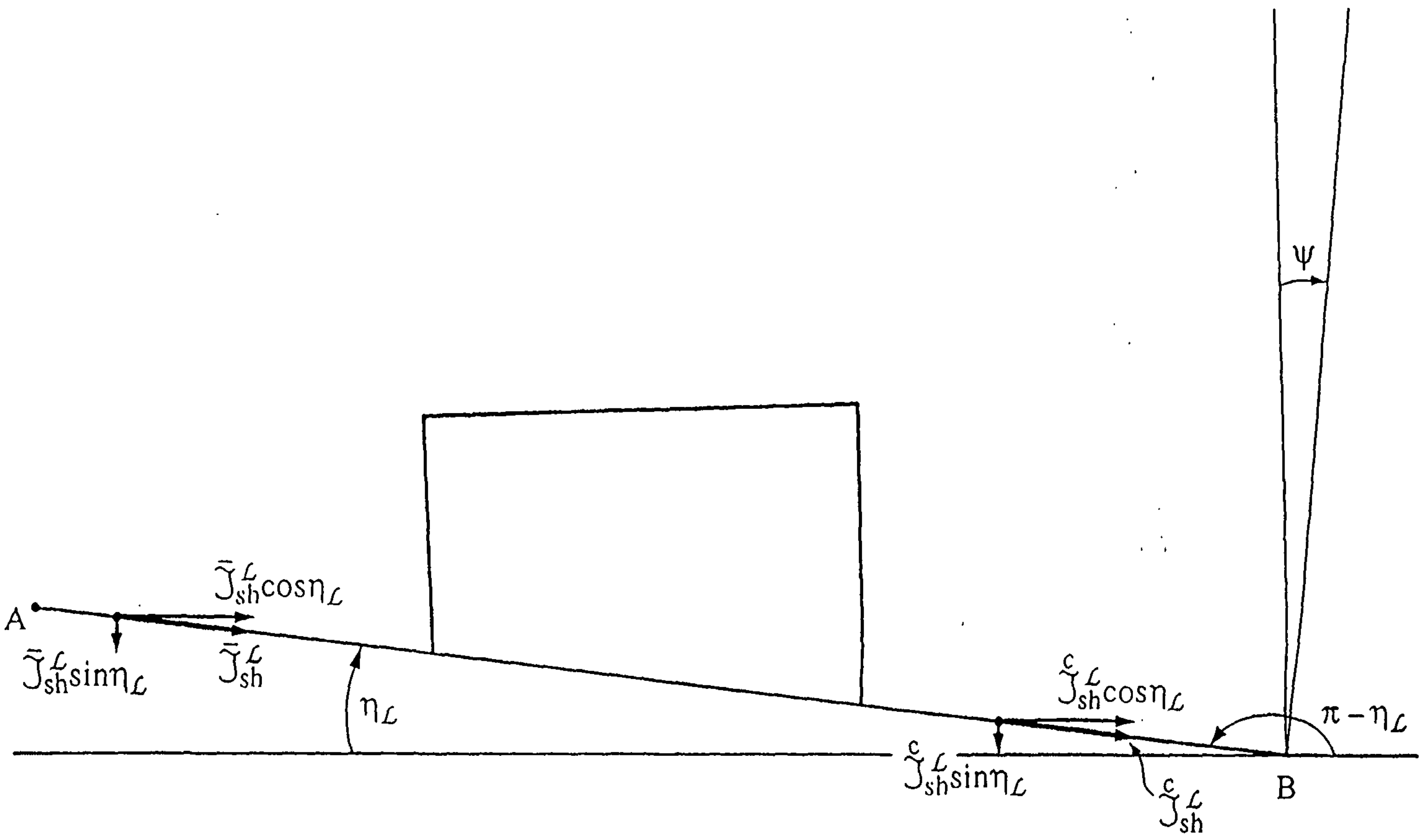

Figure 16b. Resolution of the tangential forces acting on the bottom surface of the shoe in the left-hand subchannel.

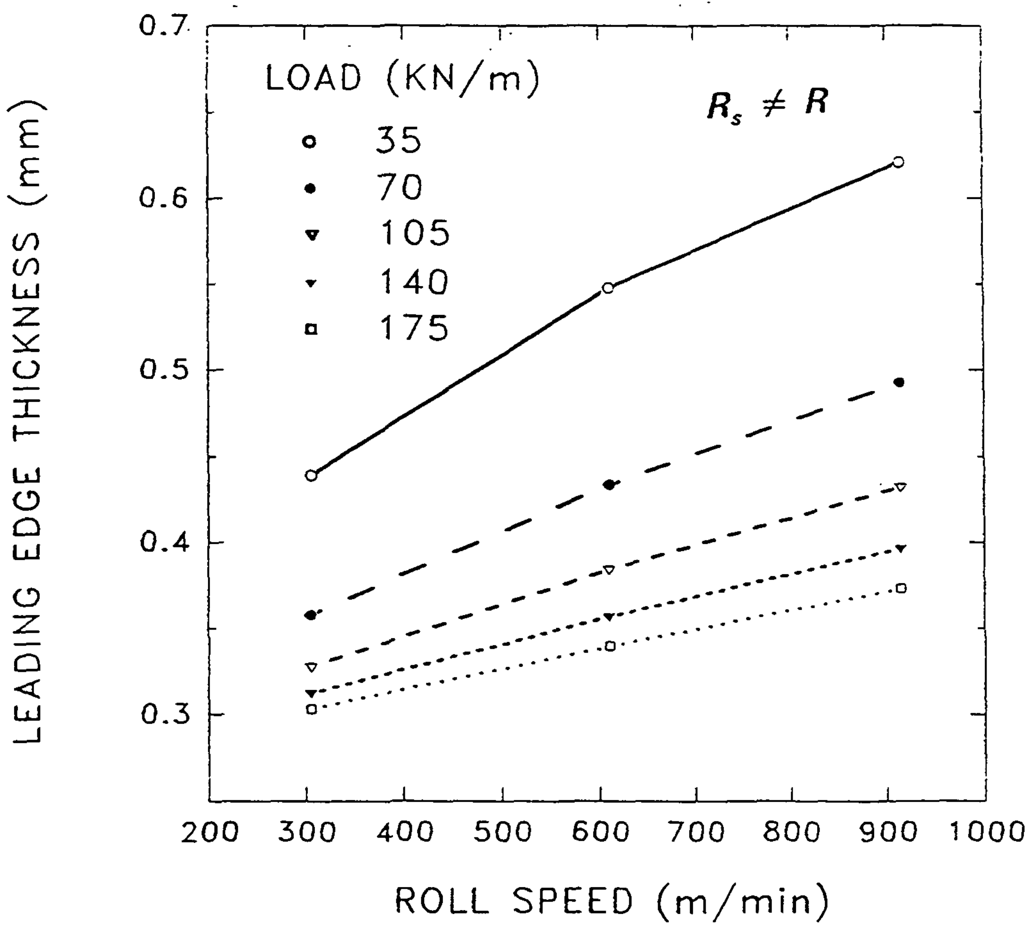

Figure 17. Lubricant film thickness at the leading edge vs. roll speed for each load applied to the "small" shoe ($R_s \neq R$).

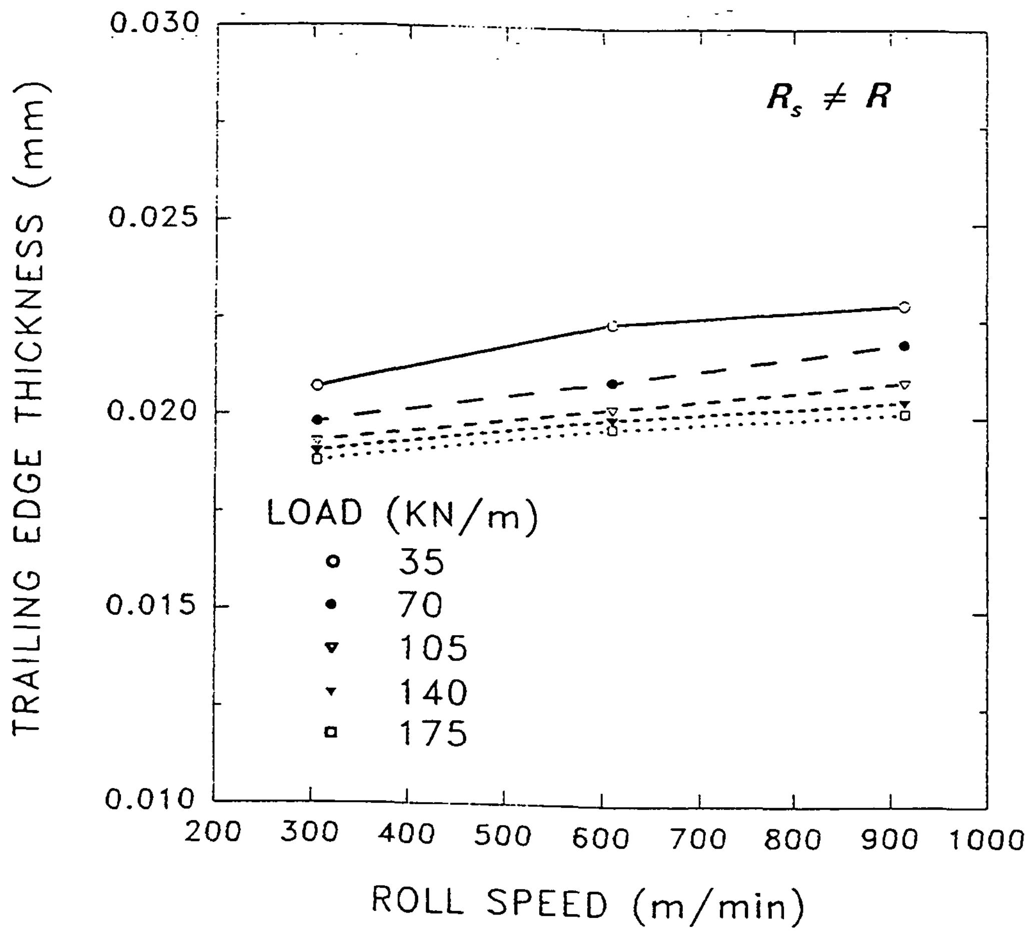

Figure 18. Lubricant film thickness at the trailing edge vs. roll speed for each applied load ($R_s \neq R$).

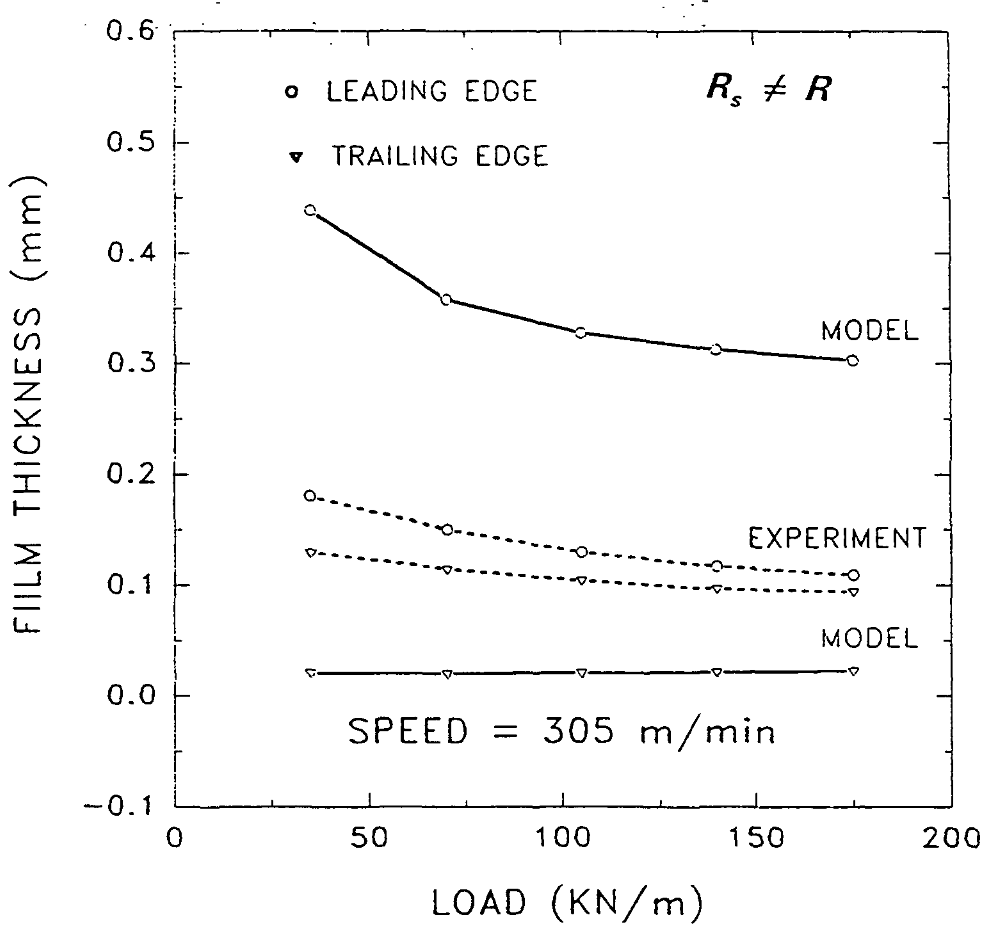

Figure 19. Comparison between the lubricant thickness predicted by the IPST model and measured by Beloit Corporation for a roll speed of 305 m/min ($R_s \neq R$).

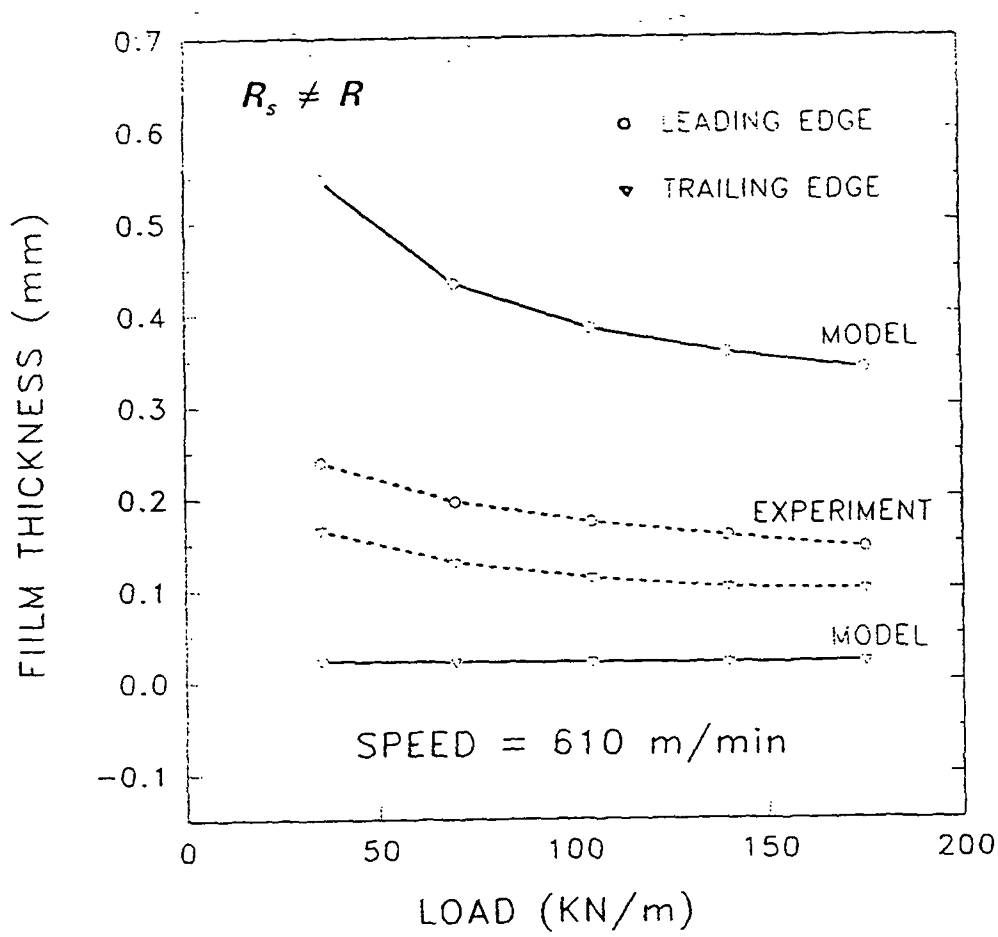

Figure 20. Comparison between the lubricant film thickness predicted by the IPST model and measured by Beloit Corporation for a roll speed of 610 m/min ($R_s \neq R$).

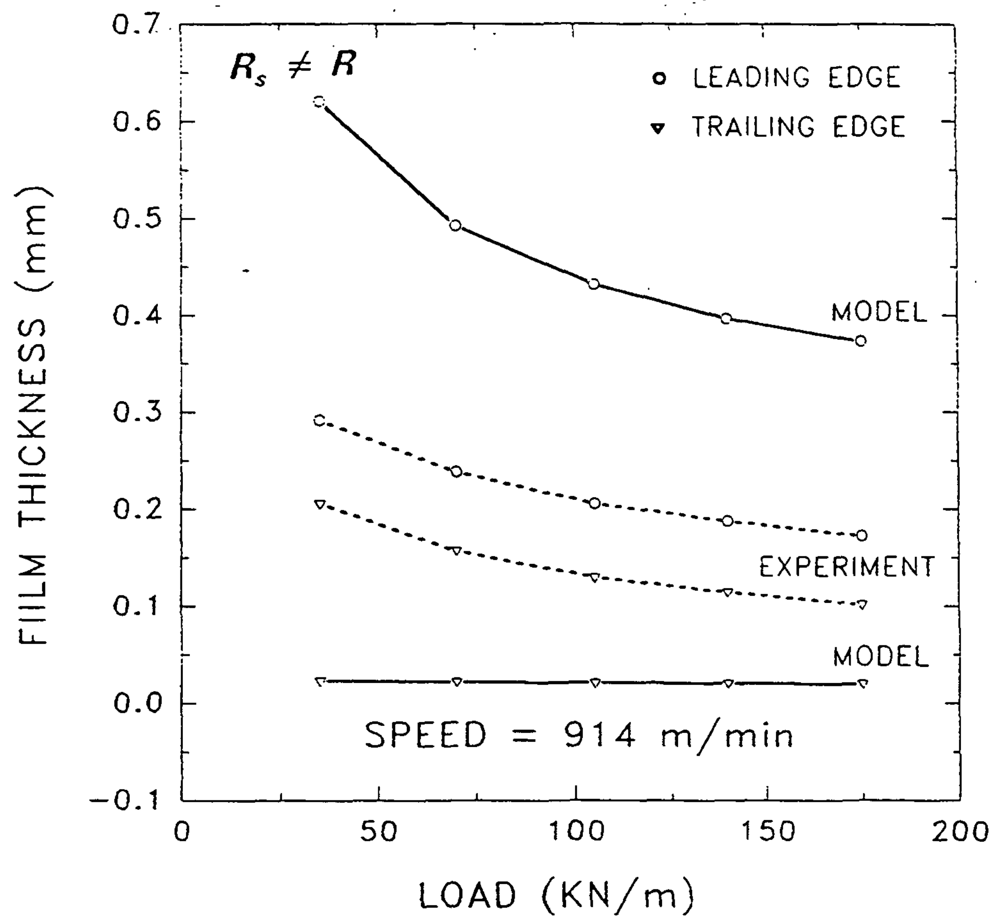

Figure 21. Comparison between the lubricant film thickness predicted by the IPST model and measured by Beloit Corporation for a roll speed of 914 m/min ($R_s \neq R$).

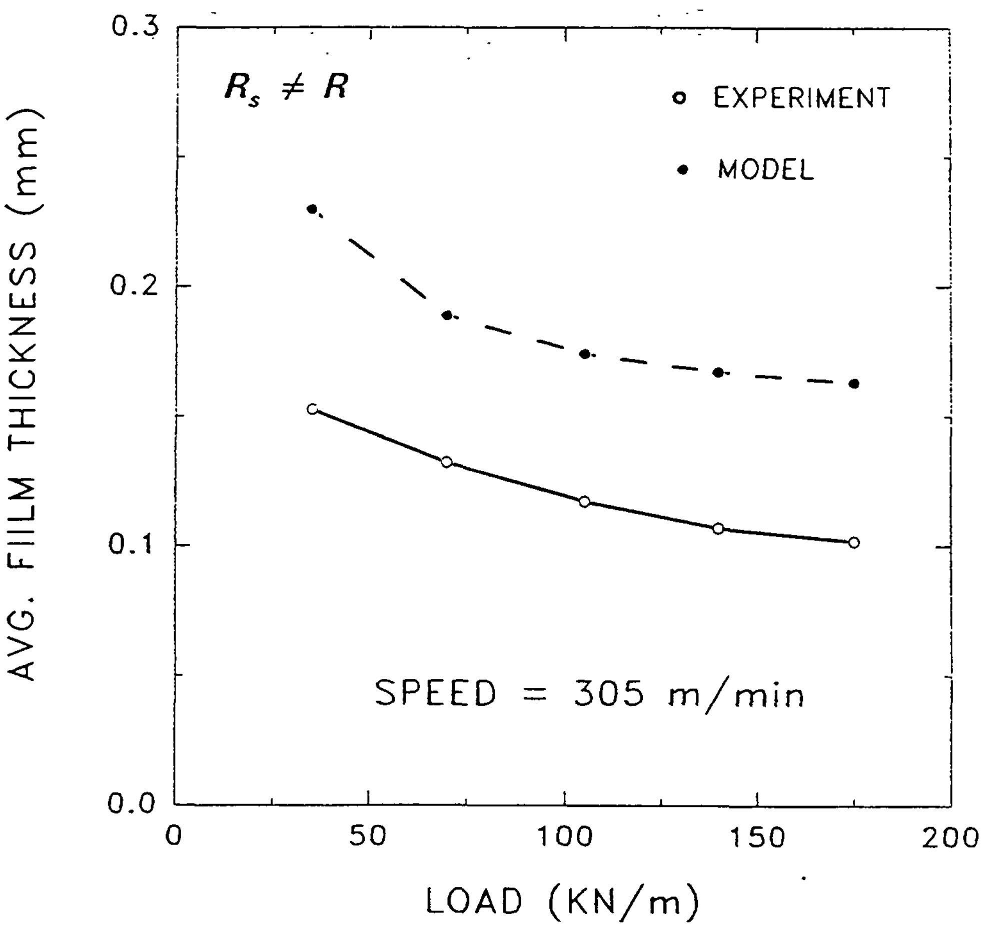

Figure 22. Comparison between the average lubricant film thickness predicted by the IPST model and measured by Beloit Corporation for a roll speed of 305 m/min ($R_s \neq R$).

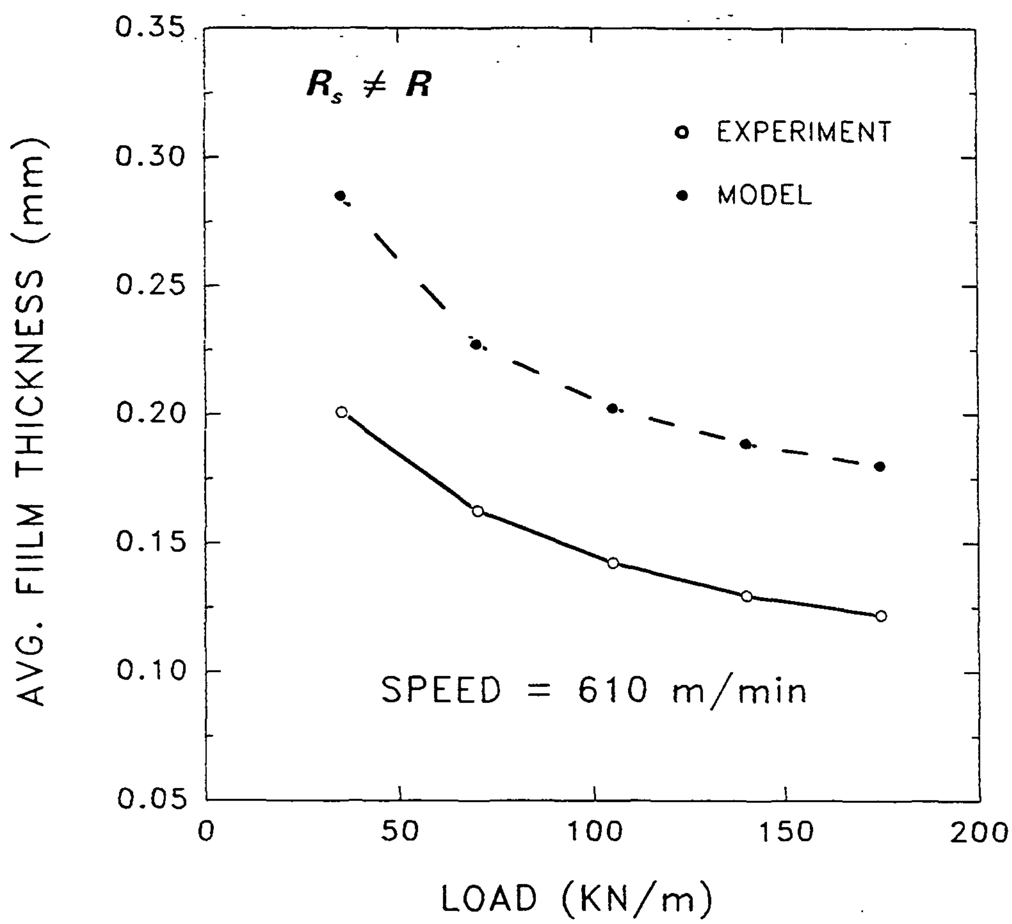

Figure 23. Comparison between the average lubricant film thickness predicted by the IPST model and measured by Beloit Corporation for a roll speed of 610 m/min ($R_s \neq R$).

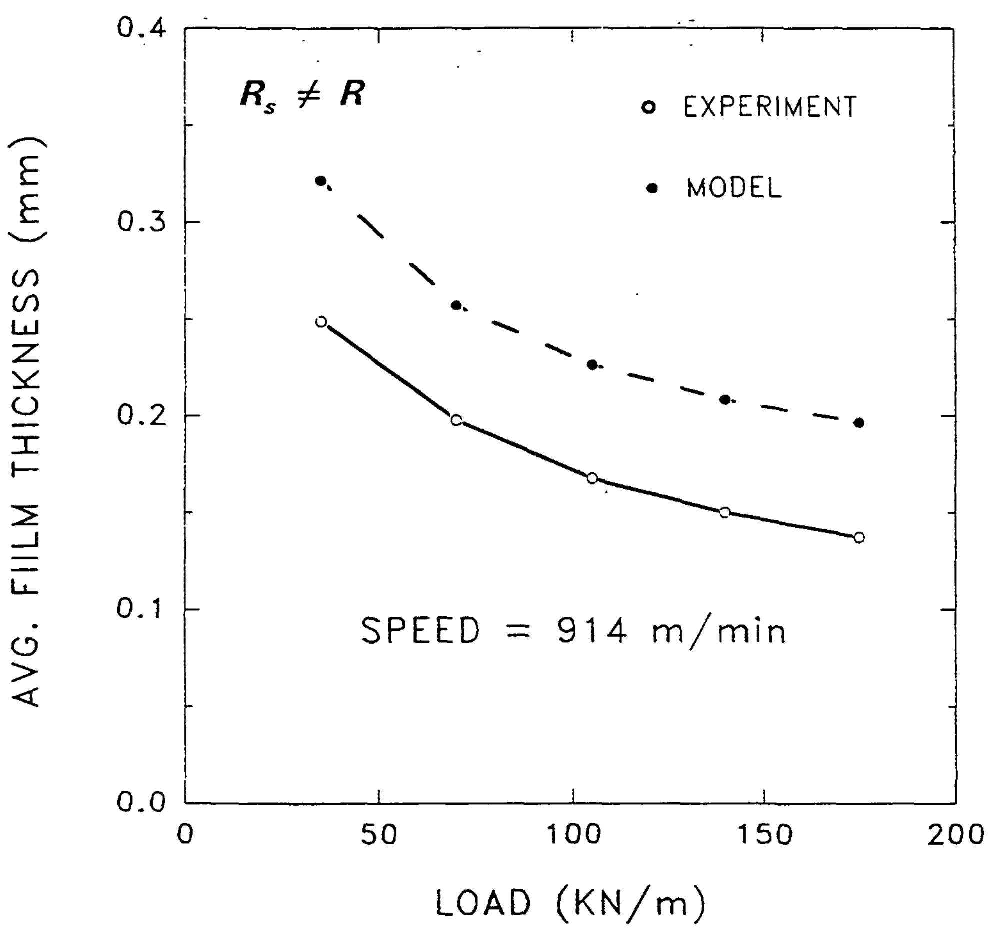

Figure 24. Comparison between the average lubricant film thickness predicted by the IPST model and measured by Beloit Corporation for a roll speed of 914 m/min ($R_s \neq R$).

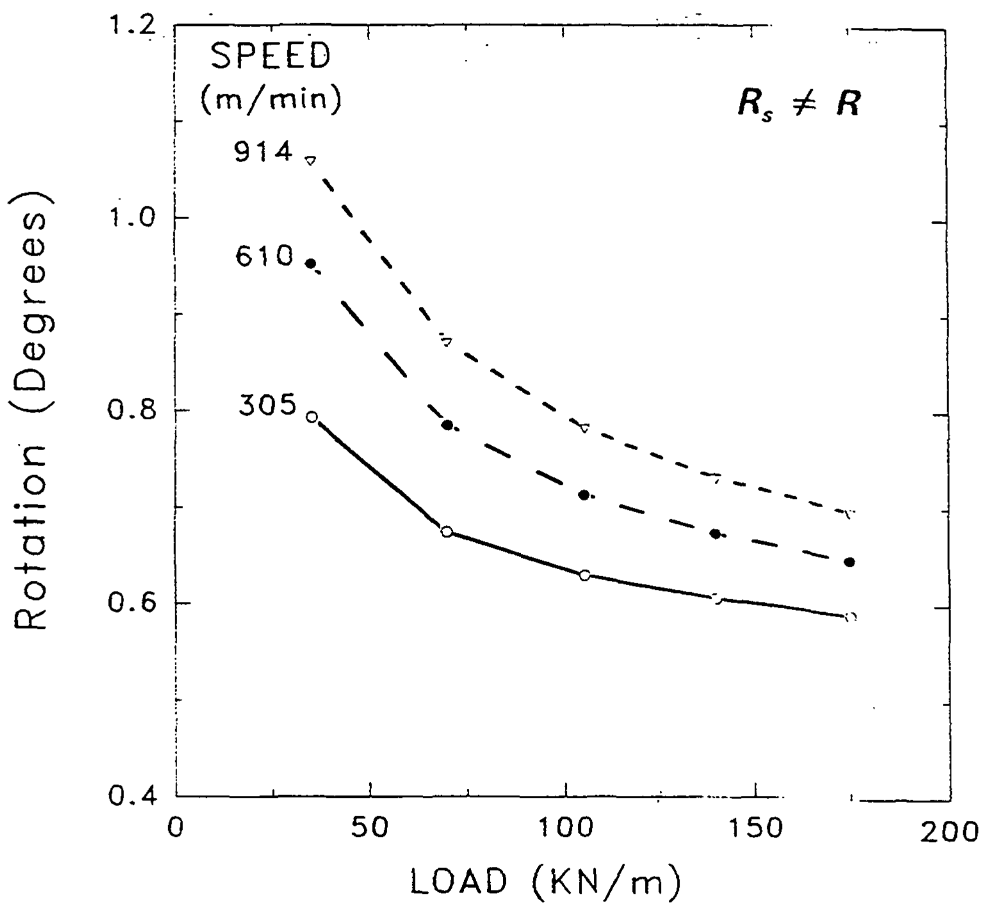

Figure 25. Angle of rotation of the shoe vs. applied load for each roll speed ($R_s \neq R$).

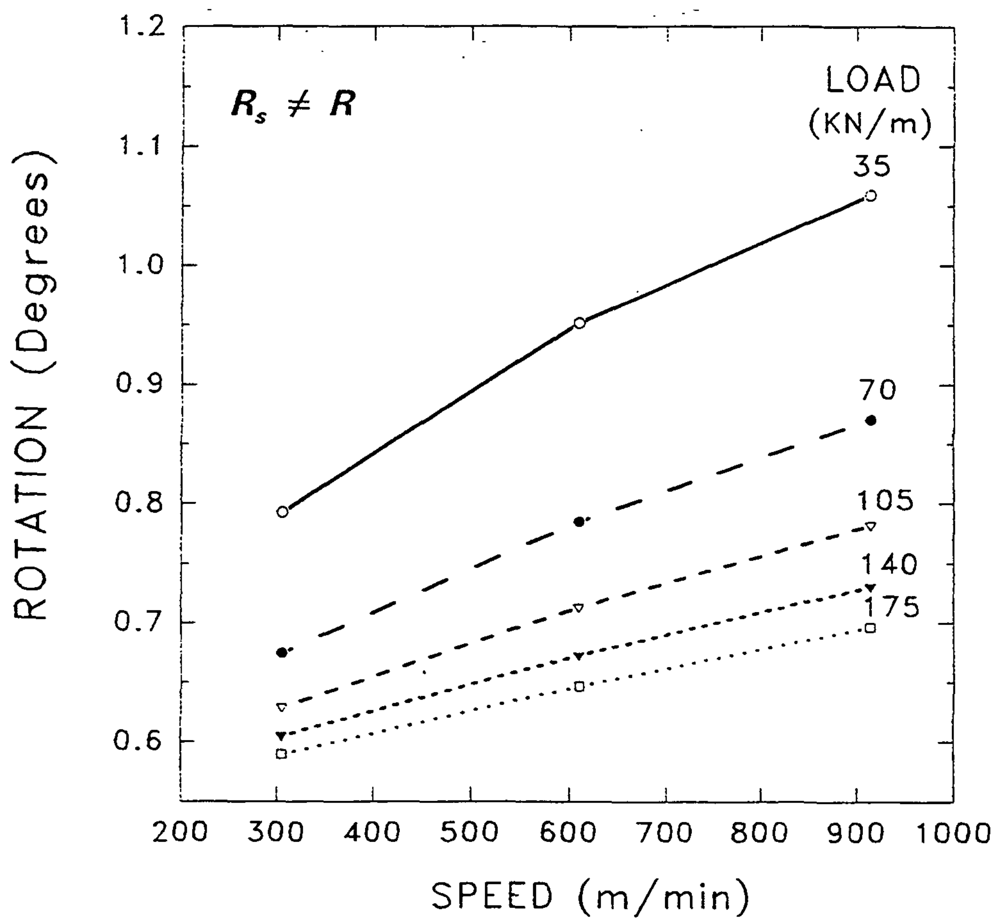

Figure 26. Angle of rotation of the shoe vs. roll speed for each applied load ($R_s \neq R$).

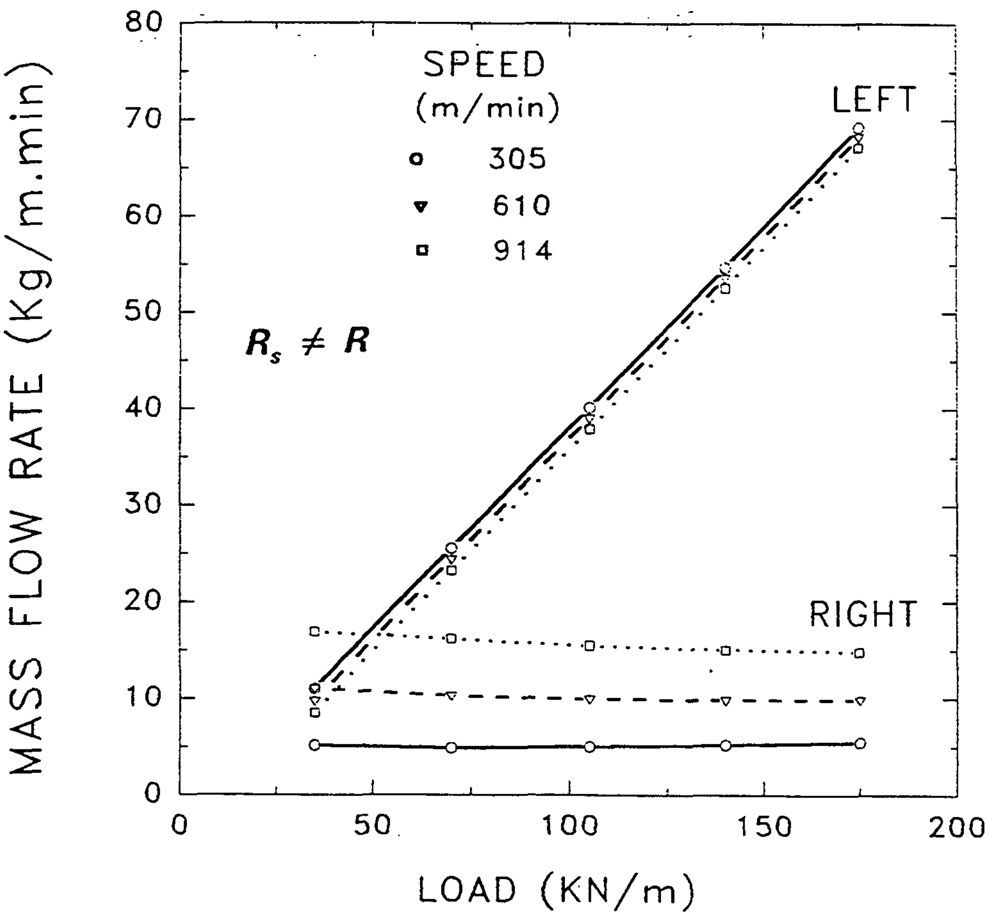

Figure 27. Lubricant mass flow rates per unit width of the roll in the left-hand and right-hand channels for each roll speed ($R_s \neq R$).

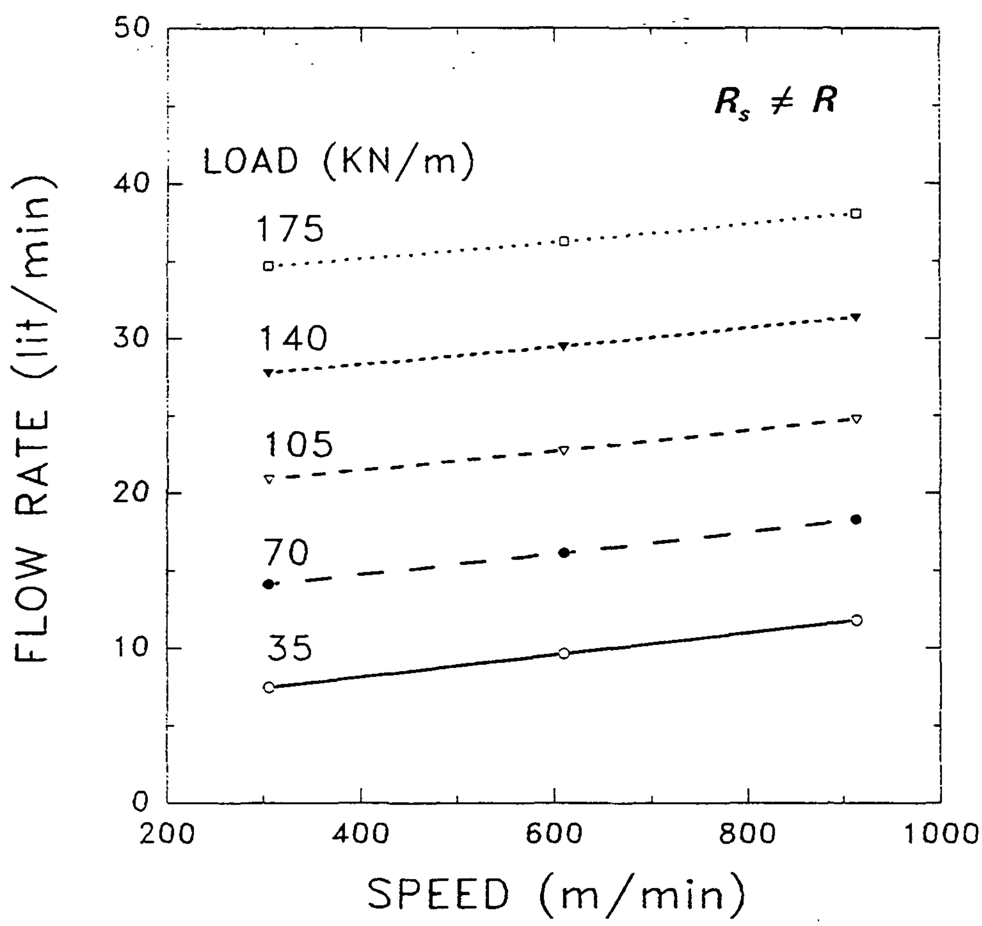

Figure 28. Lubricant total volumetric flow rate vs. roll speed for each applied load ($R_s \neq R$).

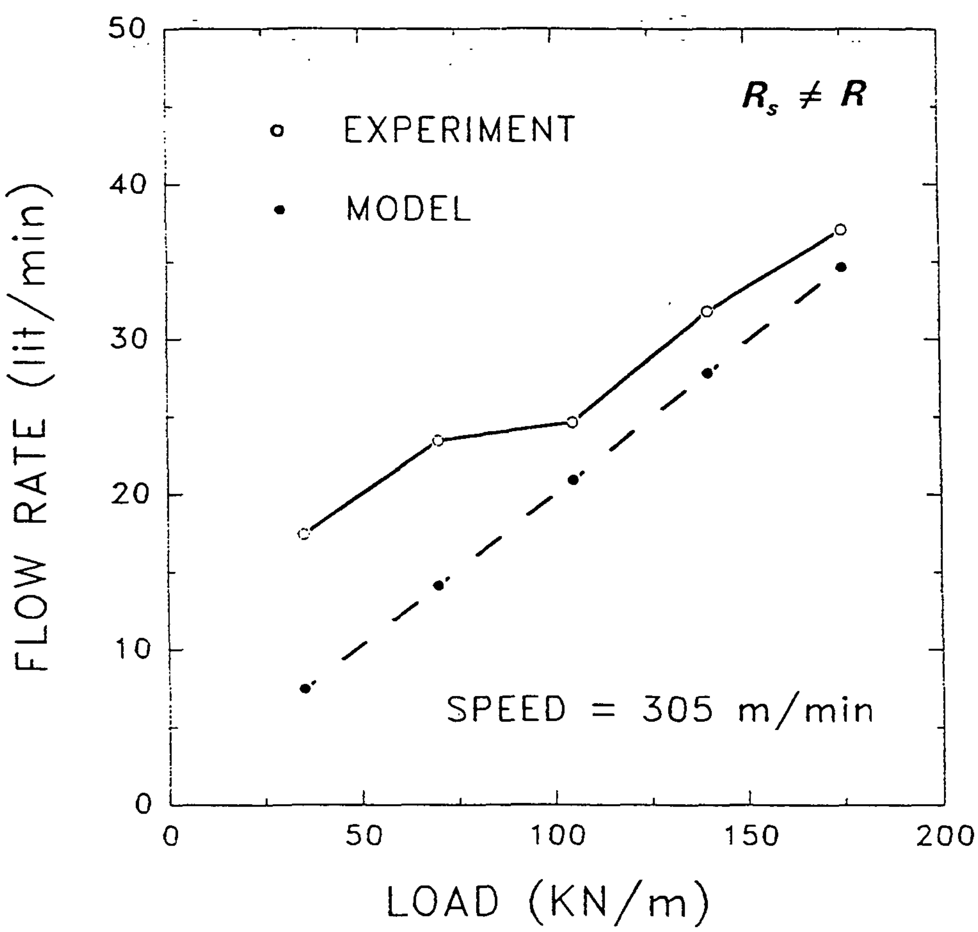

Figure 29. Comparison between the lubricant total volumetric flow rates predicted by the IPST model and measured by Beloit Corporation for a roll speed of 305 m/min ($R_s \neq R$).

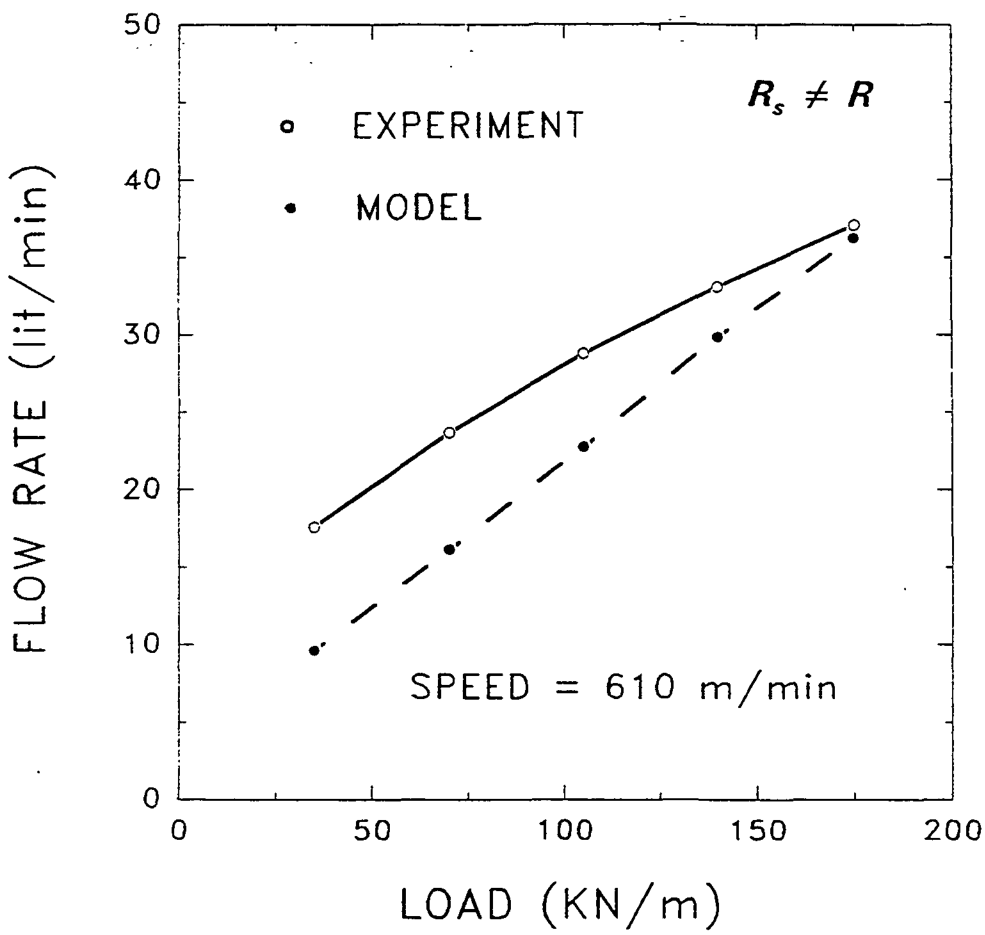

Figure 30. Comparison between the lubricant total volumetric flow rates predicted by the IPST model and measured by Beloit Corporation for a roll speed of 610 m/min ($R_s \neq R$).

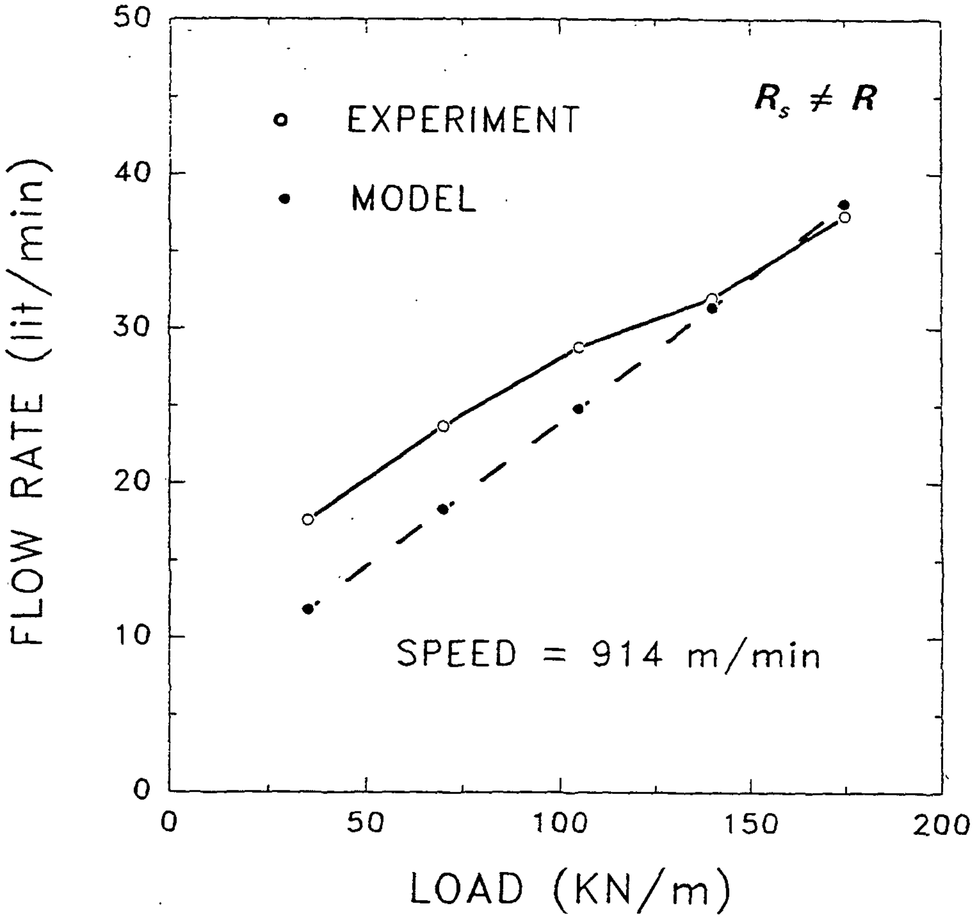

Figure 31. Comparison between the lubricant total volumetric flow rates predicted by the IPST model and measured by Beloit Corporation for a roll speed of 914 m/min ($R_s \neq R$).

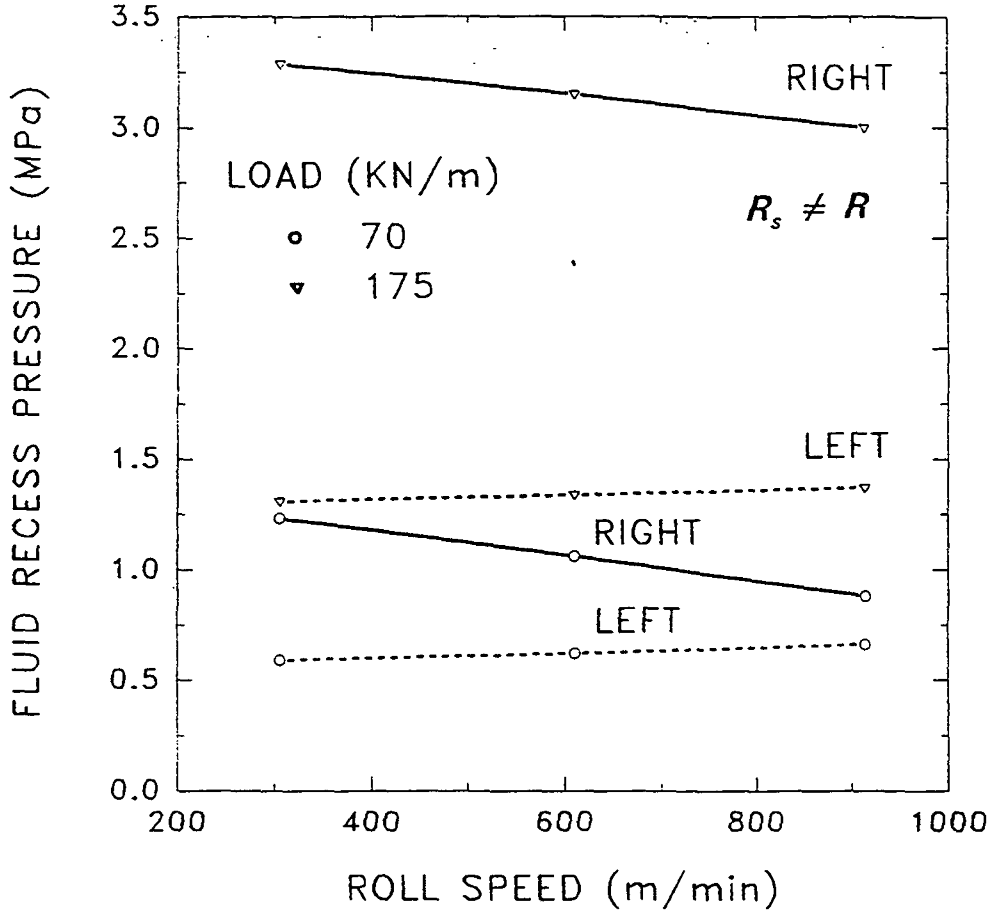

Figure 32. Lubricant recess pressures at the left-hand and right-hand channels vs. roll speed for two applied loads ($R_s \neq R$).

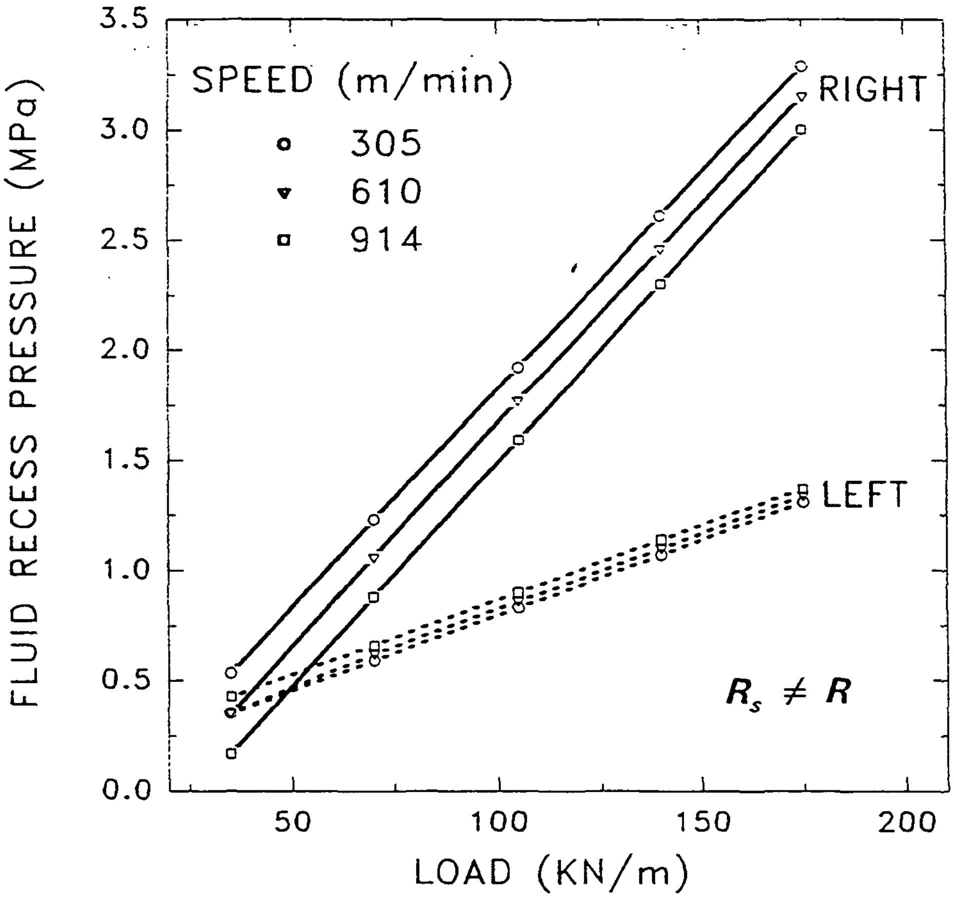

Figure 33. Lubricant recess pressures at the left-hand and right-hand channels vs. applied load for each roll speed ($R_s \neq R$).

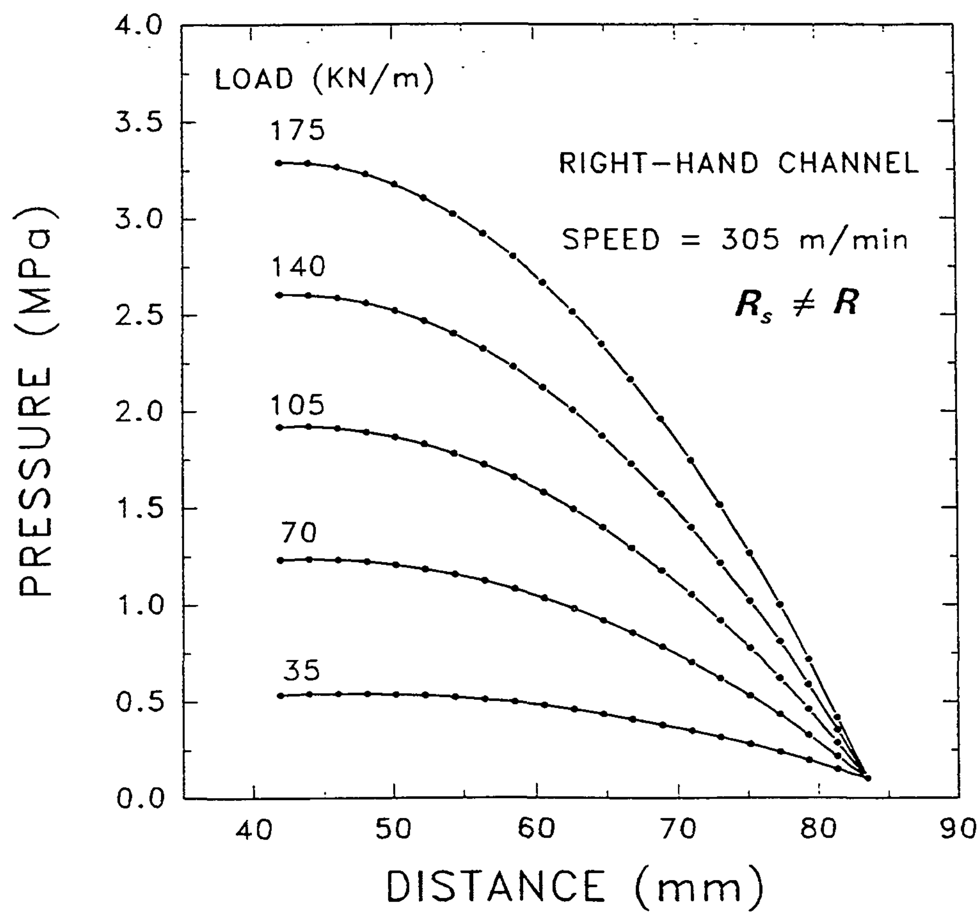

Figure 34a. Lubricant pressure distribution along the length of the right-hand channel at a roll speed of 305 m/min ($R_s \neq R$).

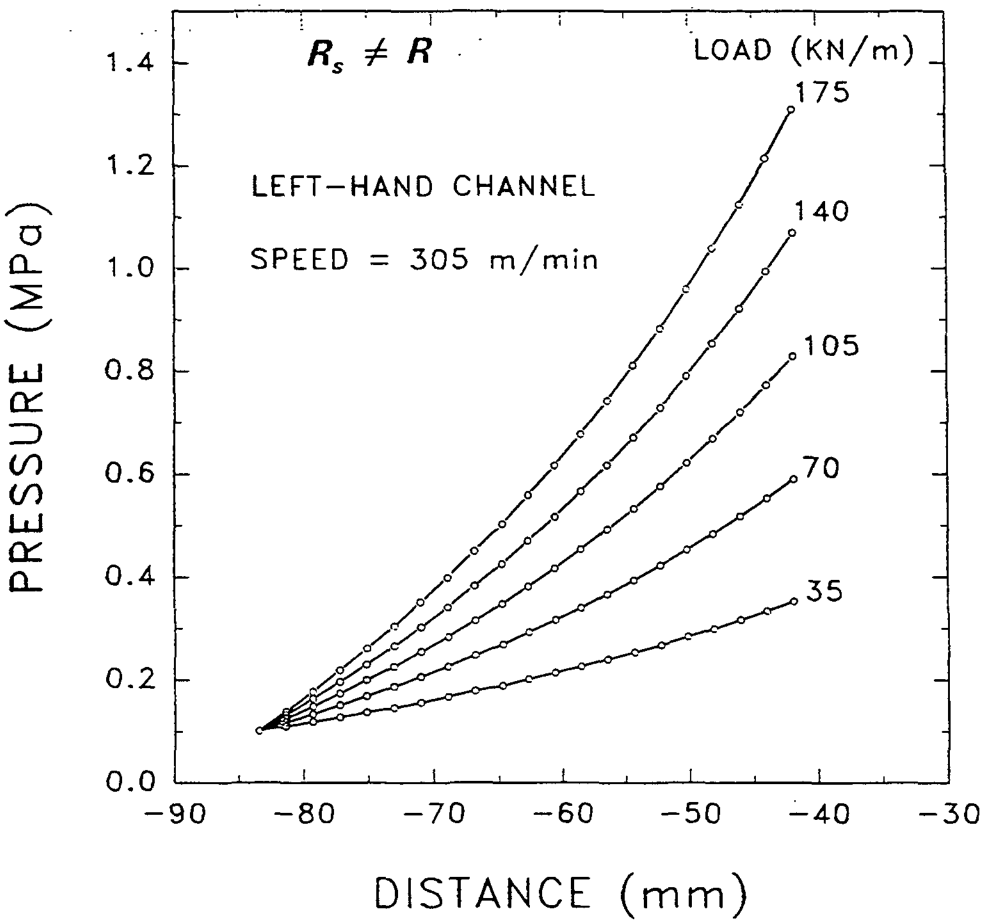

Figure 34b. Lubricant pressure distribution along the length of the left-hand channel at a roll speed of 305 m/min ($R_s \neq R$).

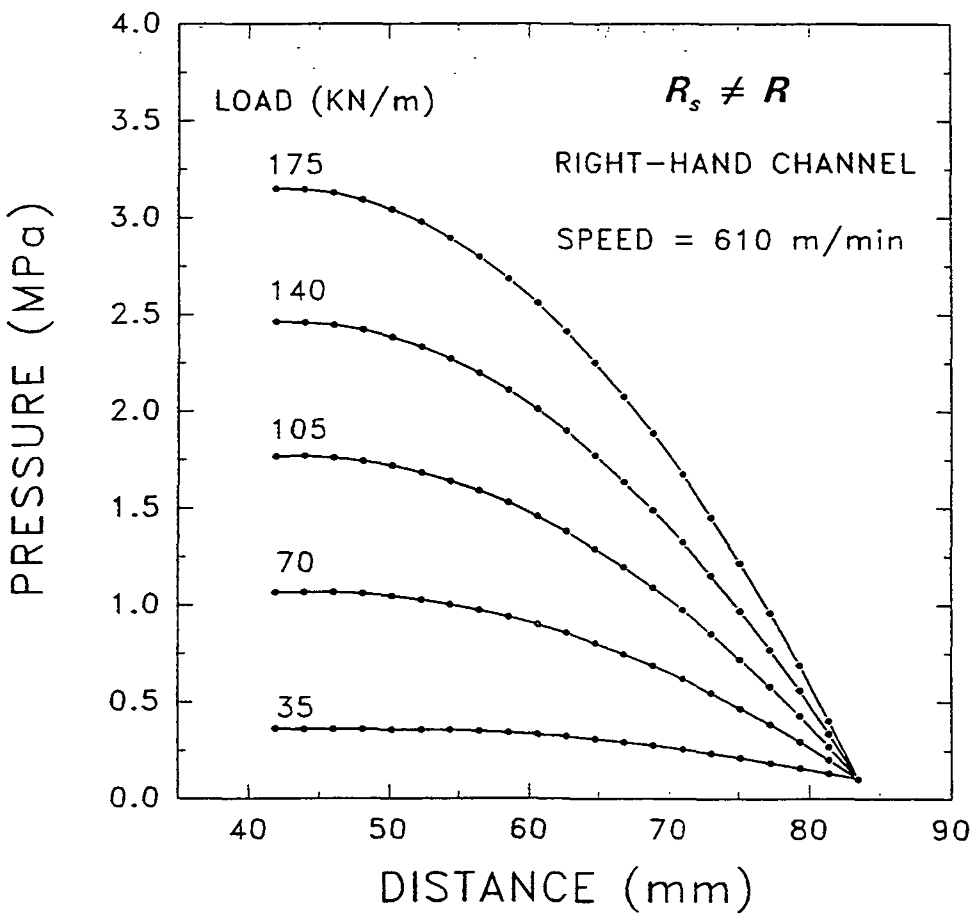

Figure 35a. Lubricant pressure distribution along the length of the right-hand channel at a roll speed of 610 m/min ($R_s \neq R$).

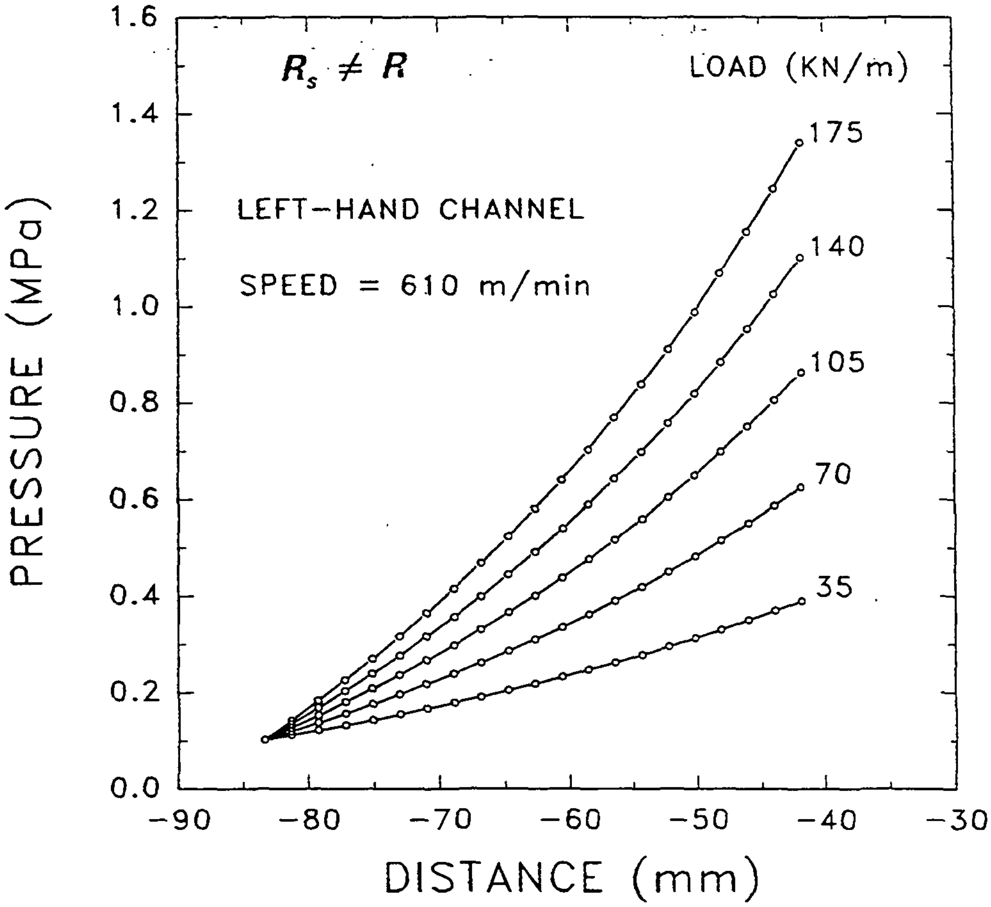

Figure 35b. Lubricant pressure distribution along the length of the left-hand channel at a roll speed of 610 m/min ($R_s \neq R$).

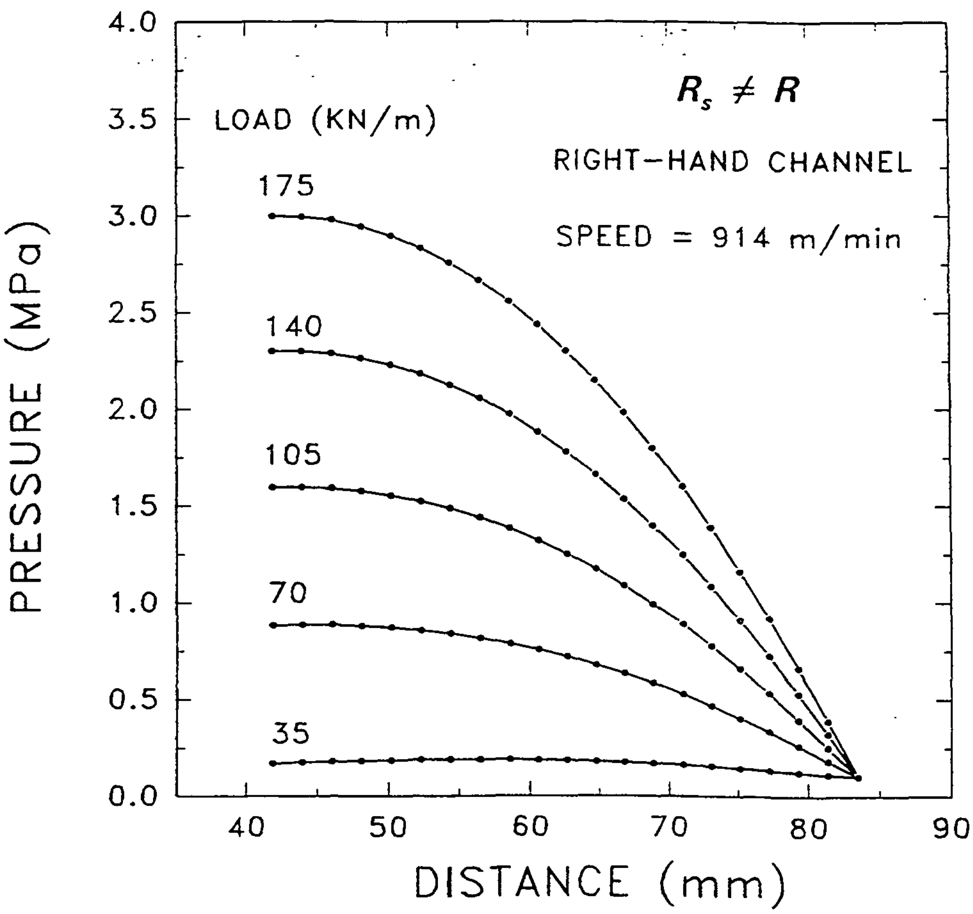

Figure 36a. Lubricant pressure distribution along the length of the right-hand channel at a roll speed of 914 m/min ($R_s \neq R$).

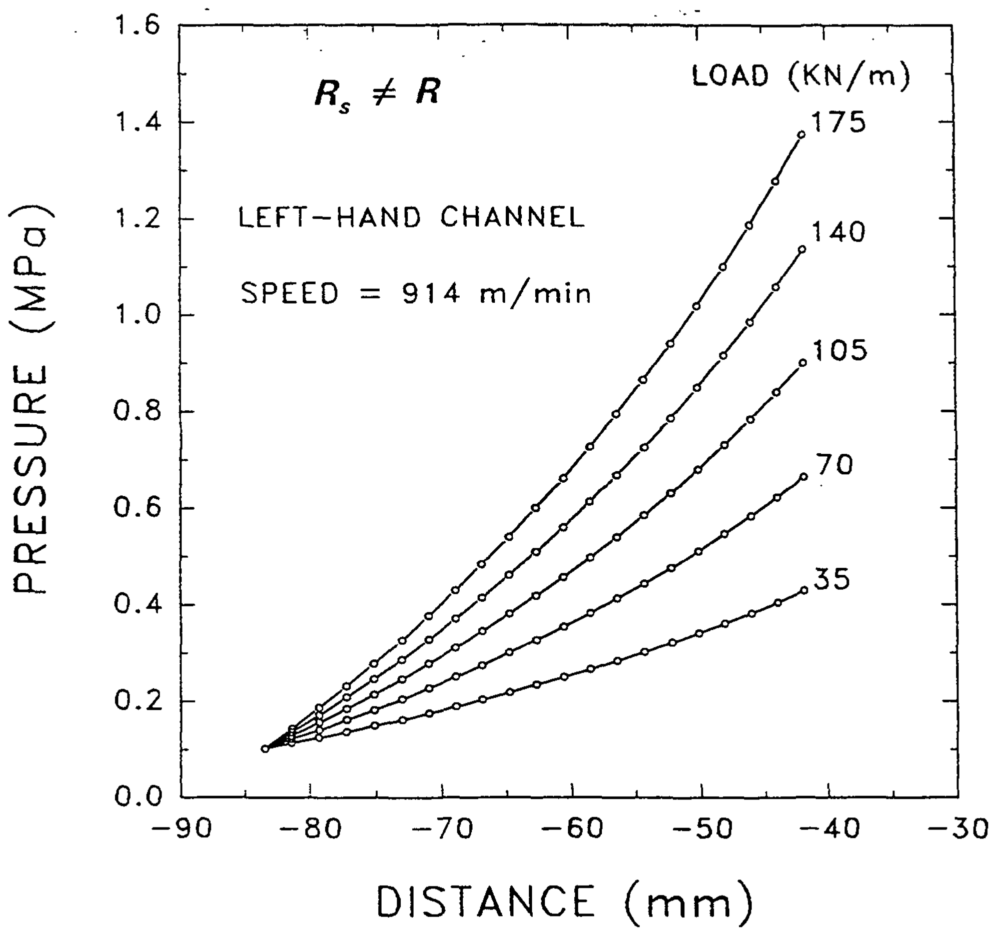

Figure 36b. Lubricant pressure distribution along the length of the left-hand channel at a roll speed of 914 m/min ($R_s \neq R$).

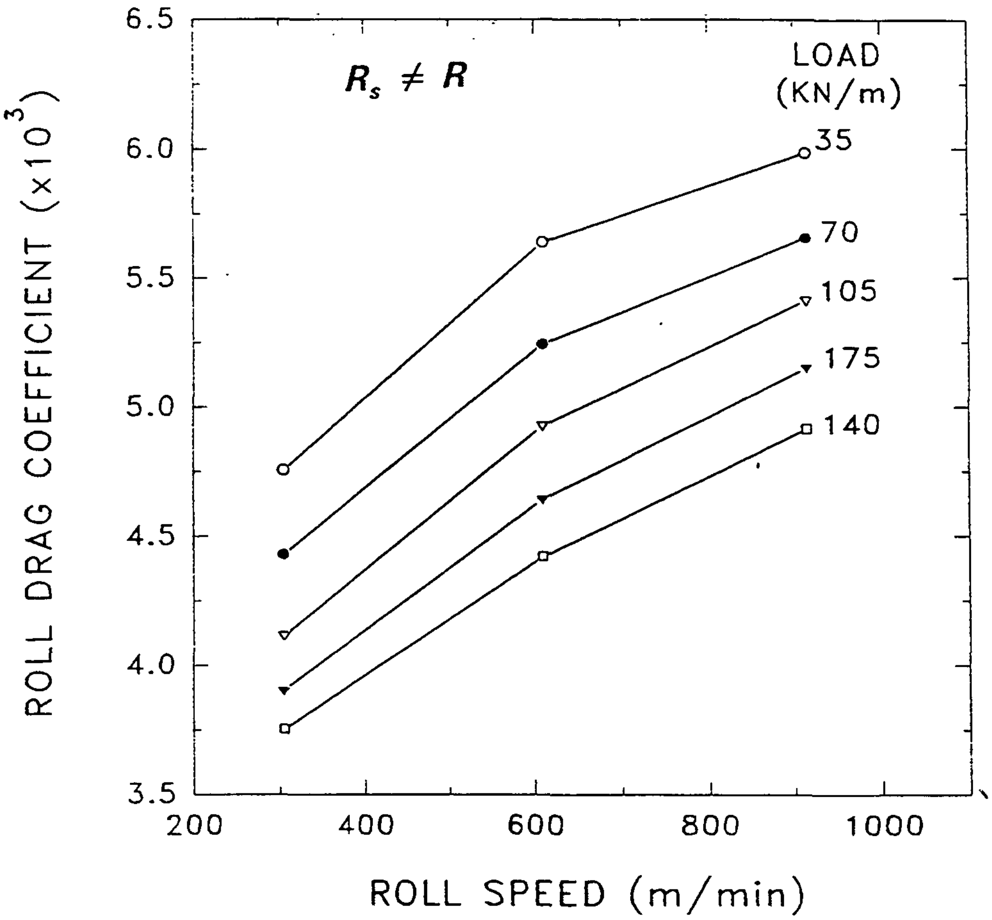

Figure 37. Roll drag coefficient vs. roll speed at each applied load ($R_s \neq R$).

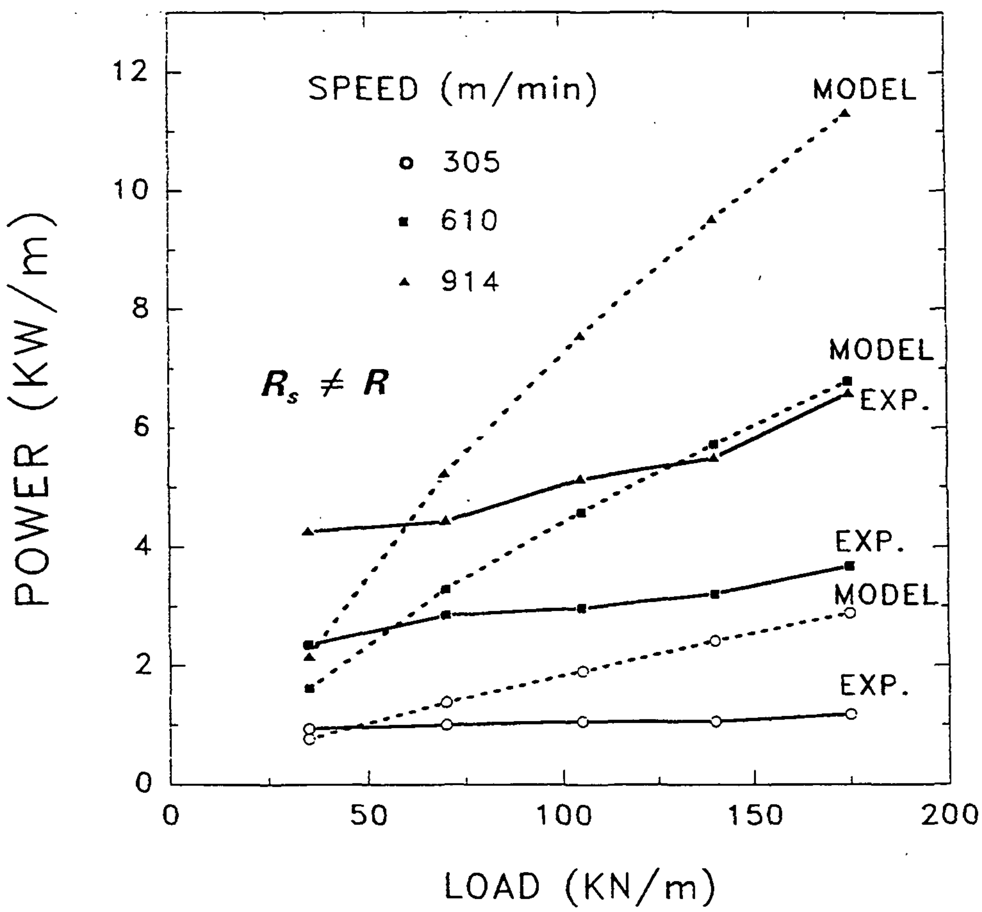

Figure 38. Comparison between the mechanical power required to operate the roll predicted by the IPST model and measured by Beloit Corporation ($R_s \neq R$).

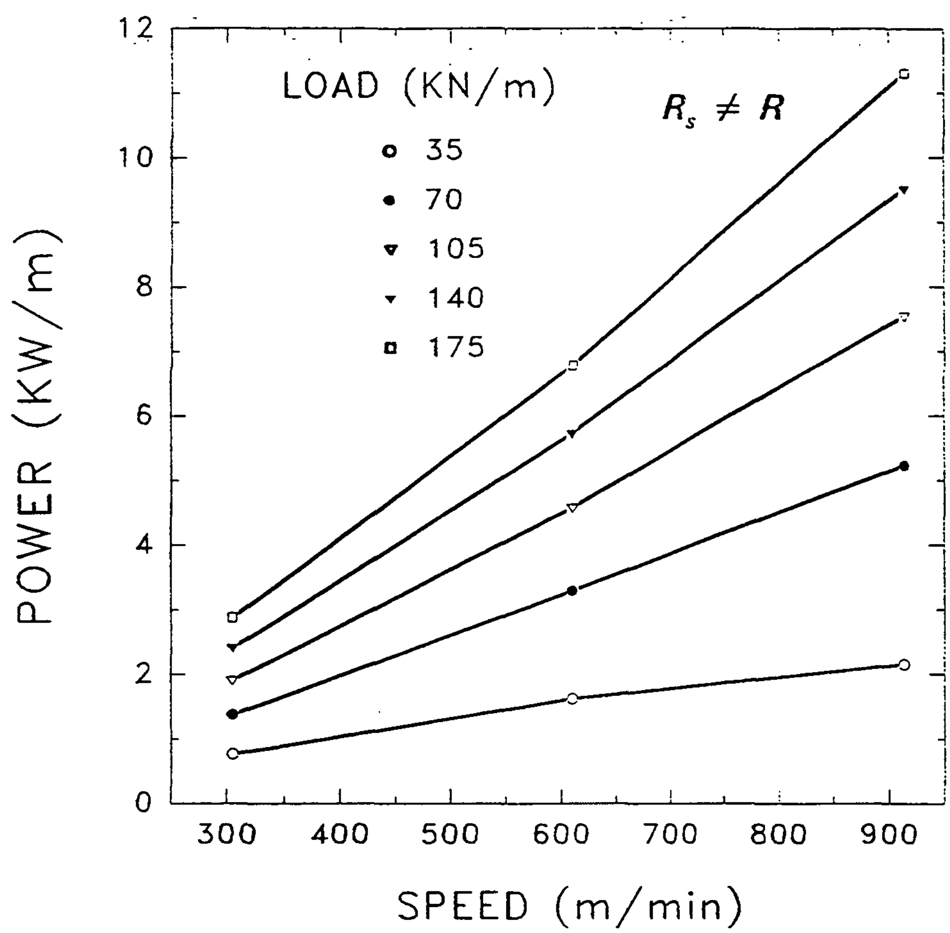

Figure 39. Mechanical power required to operate the roll vs. roll speed for each applied load ($R_s \neq R$).

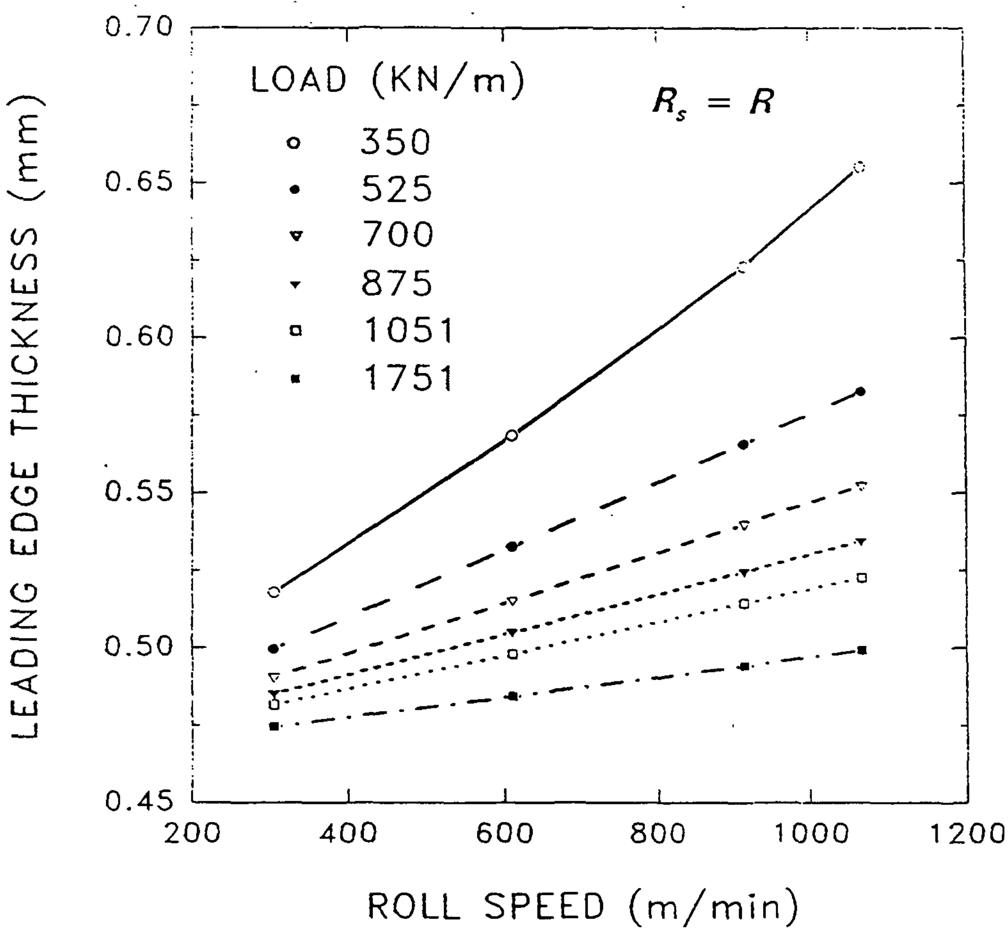

Figure 40. Lubricant film thickness at the leading edge vs. roll speed for each load applied to the "large" shoe ($R_s = R$).

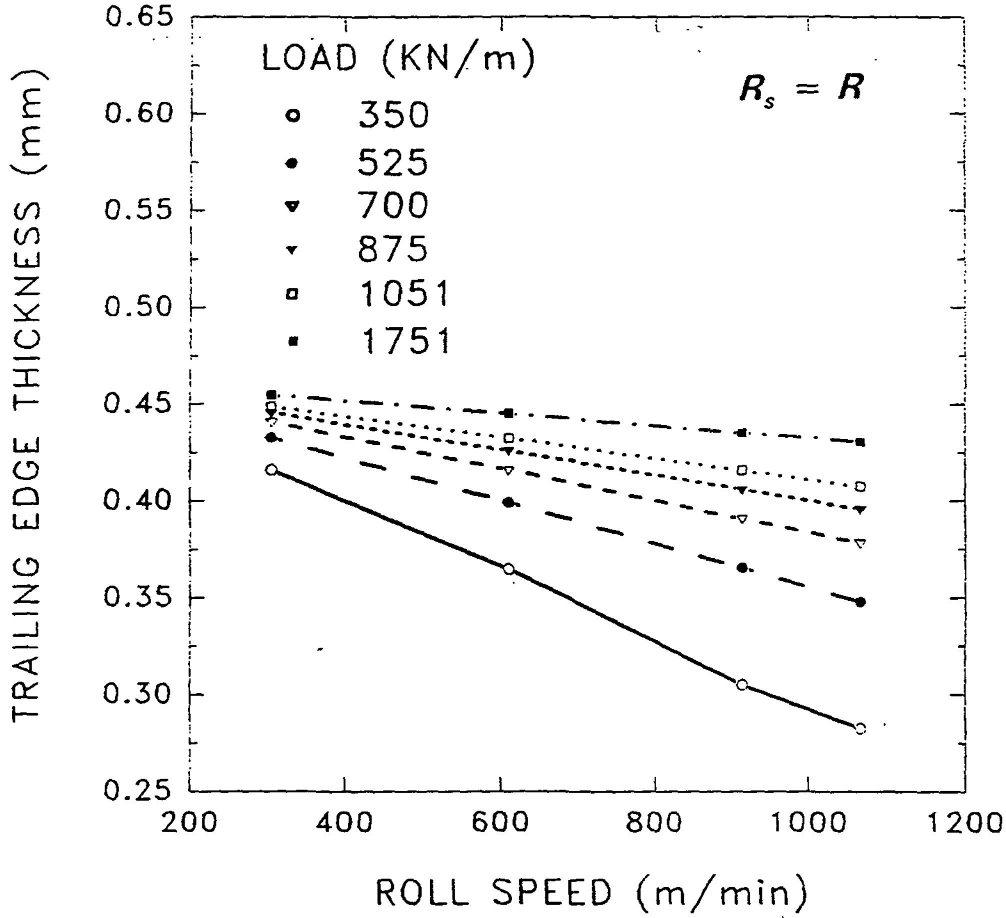

Figure 41. Lubricant film thickness at the trailing edge vs. roll speed for each applied load ($R_s = R$).

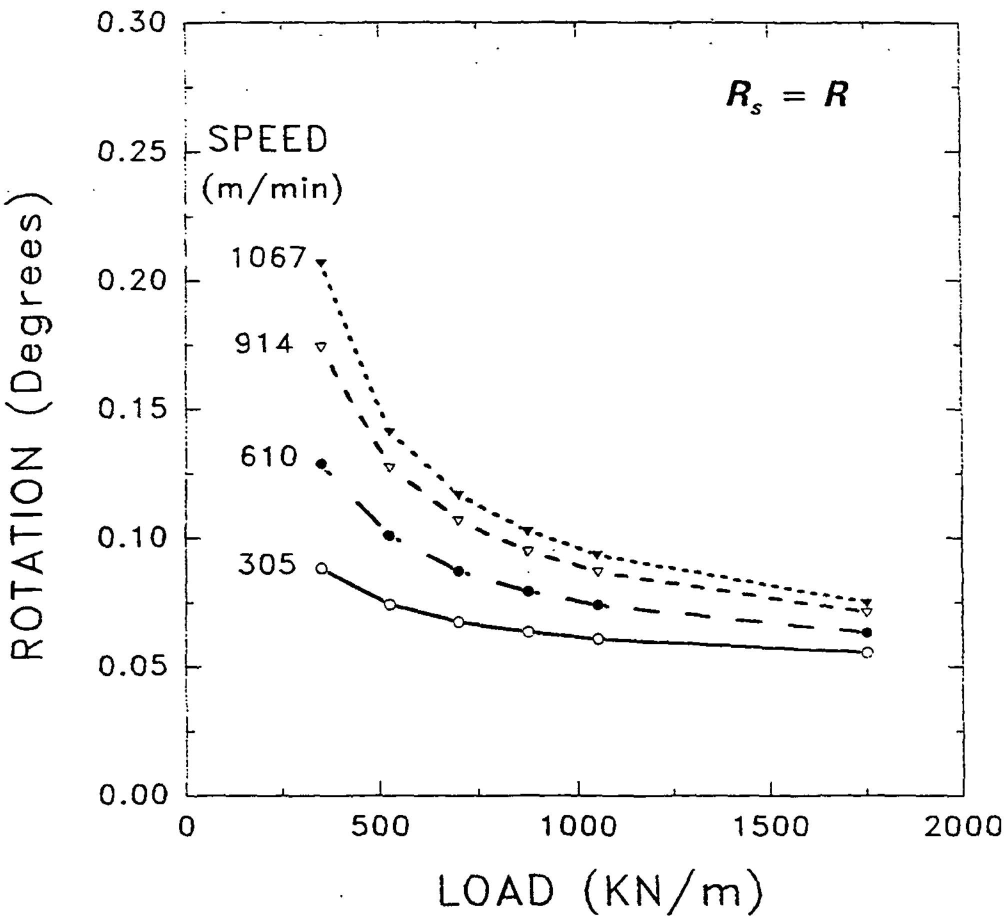

Figure 42. Angle of rotation of the shoe vs. load for each roll speed ($R_s = R$).

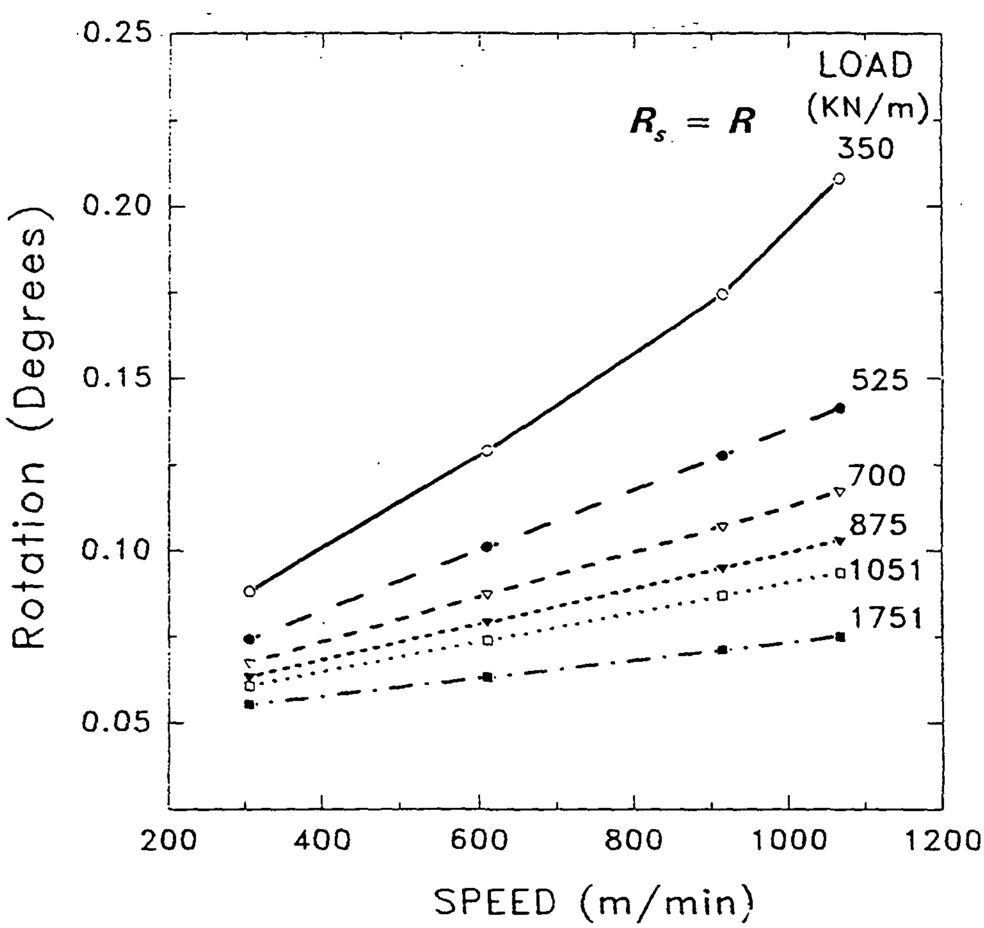

Figure 43. Angle of rotation of the shoe vs. roll speed for each applied load ($R_s = R$).

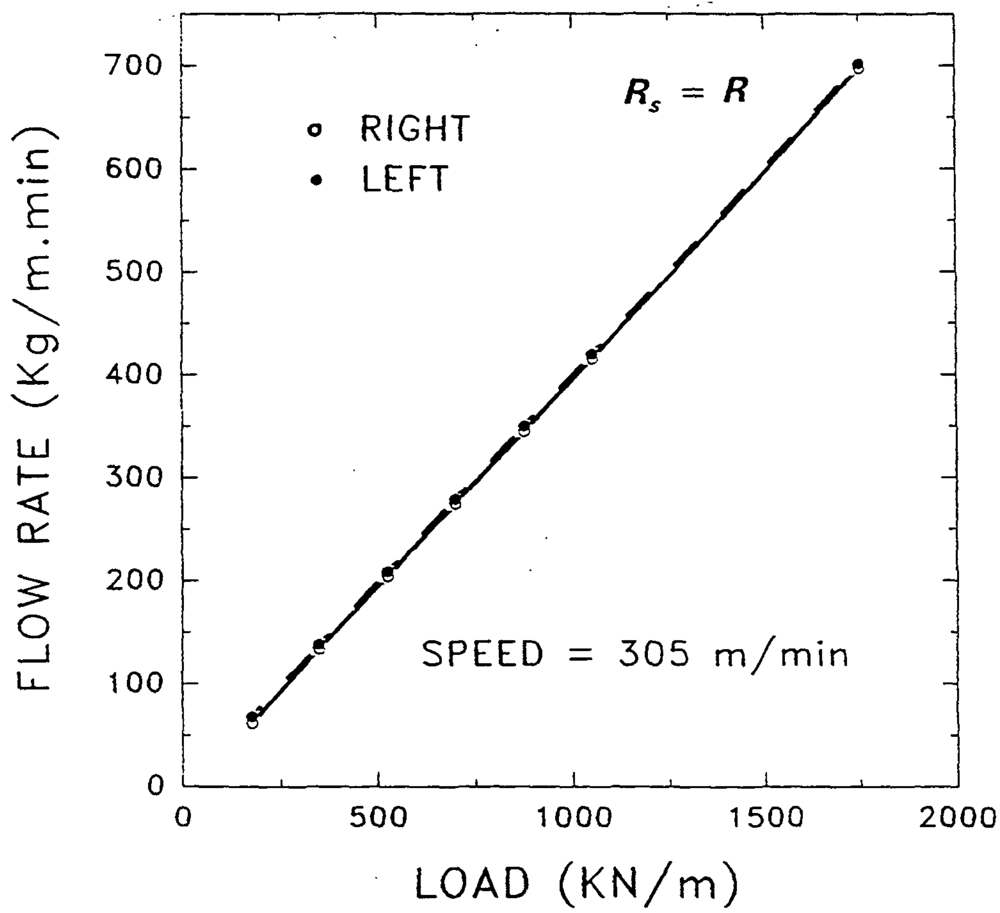

Figure 44. Lubricant mass flow rates per unit width of the roll in the left-hand and right-hand channels at a roll speed of 305 m/min ($R_s = R$).

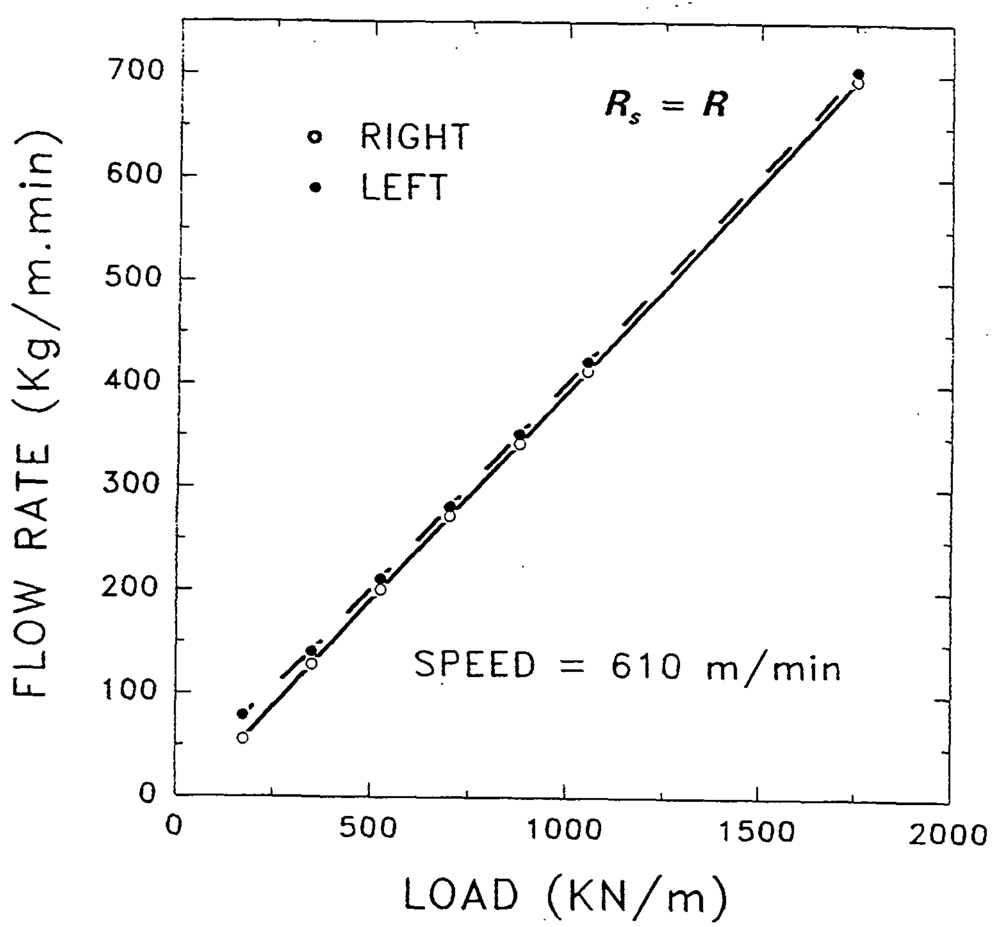

Figure 45. Lubricant mass flow rates per unit width of the roll in the left-hand and right-hand channels at a roll speed of 610 m/min ($R_s = R$).

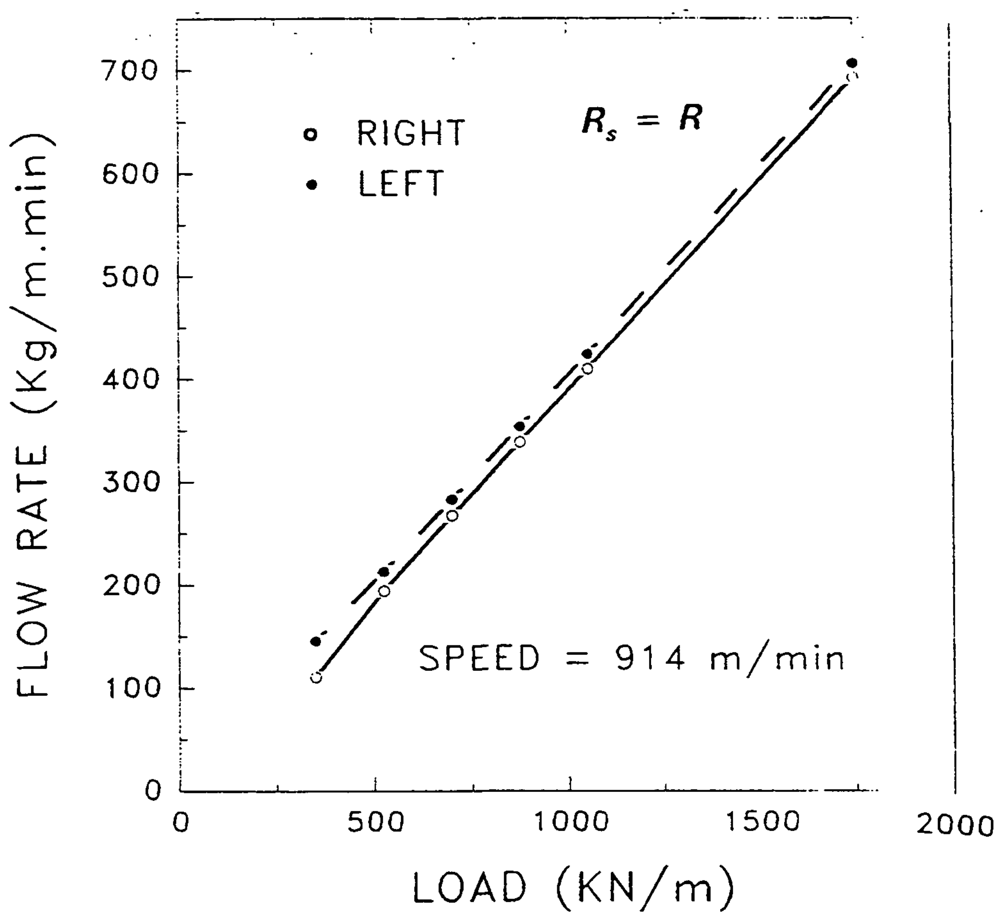

Figure 46. Lubricant mass flow rates per unit width of the roll in the left-hand and right-hand channels at a roll speed of 914 m/min ($R_s = R$).

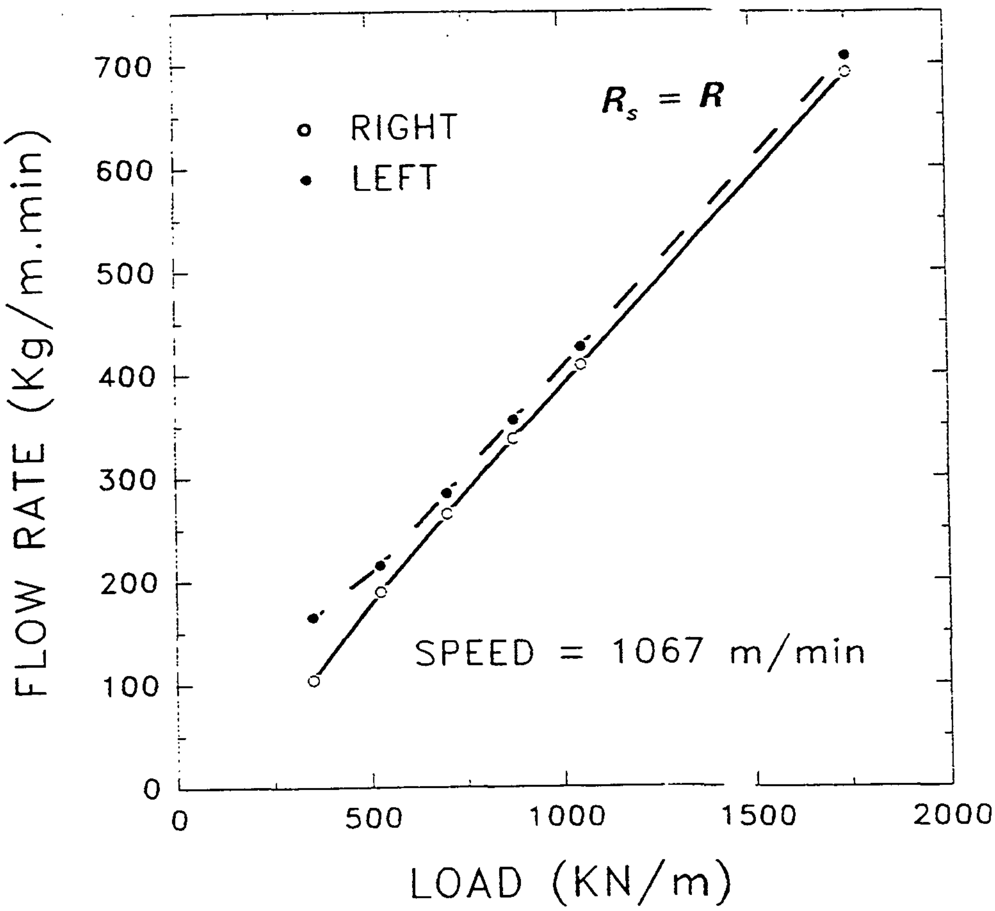

Figure 47. Lubricant mass flow rates per unit width of the roll in the left-hand and right-hand channels at a roll speed of 1067 m/min ($R_s = R$).

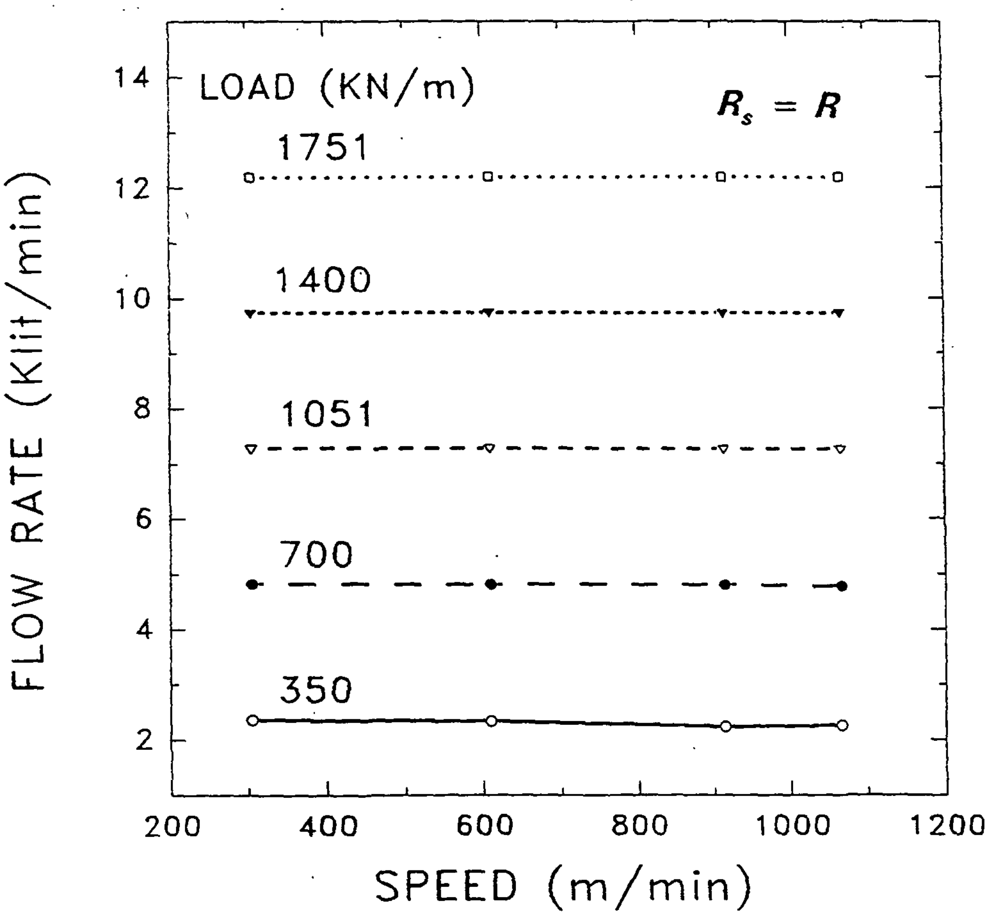

Figure 48. Lubricant total volumetric flow rate vs. roll speed for each applied load ($R_s = R$).

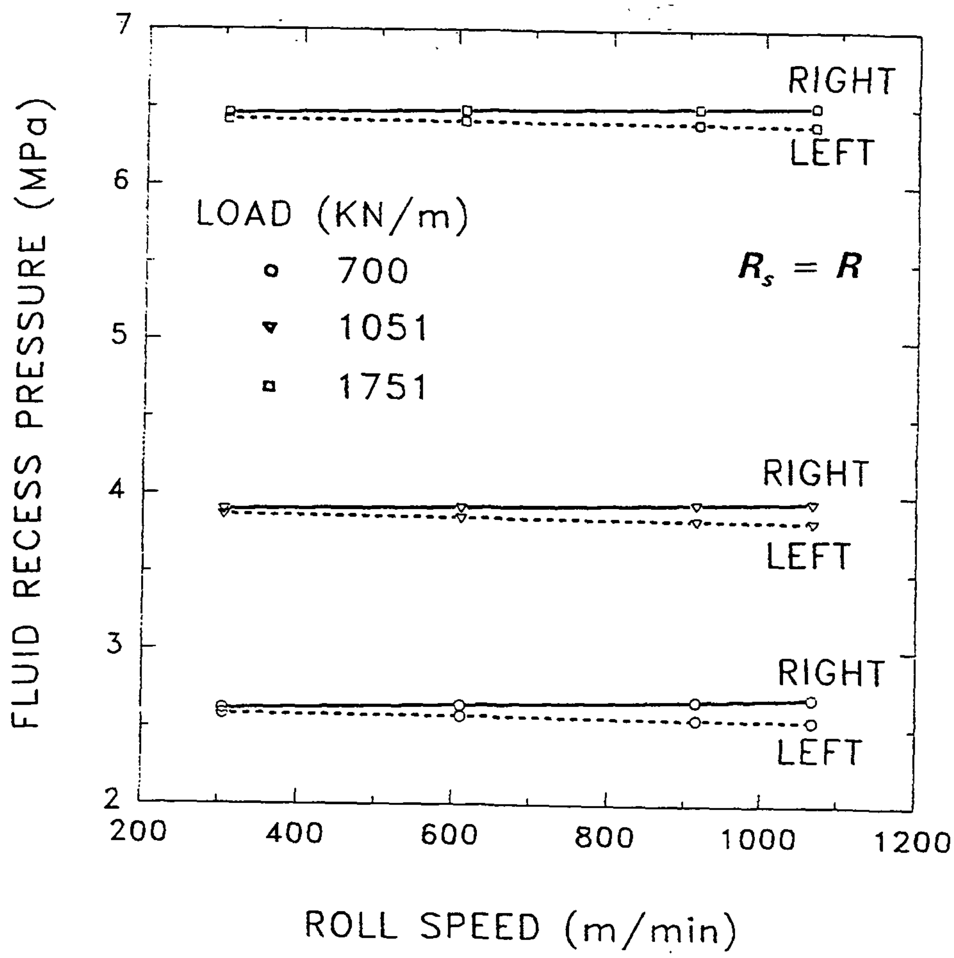

Figure 49. Lubricant recess pressure at the left-hand and right-hand channels vs. roll speed for three applied loads ($R_s = R$).

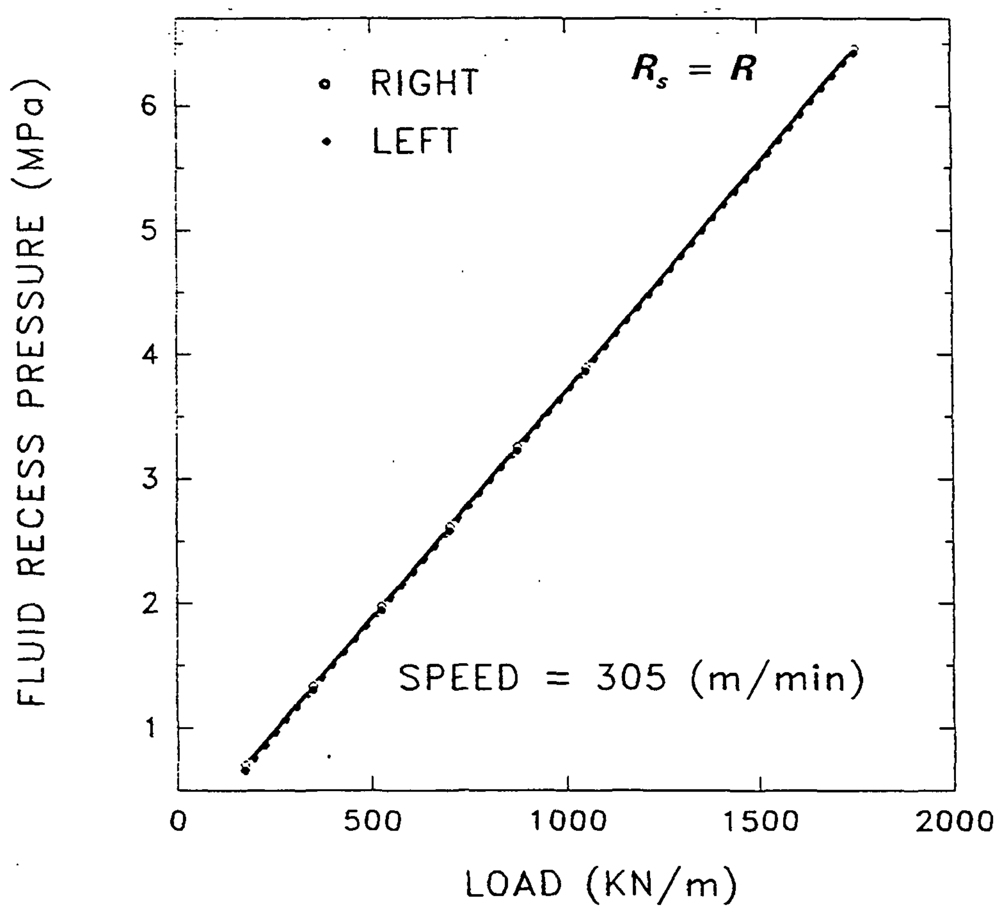

Figure 50. Lubricant recess pressure at the left-hand and right-hand channels vs. load for a roll speed of 305 m/min ($R_s = R$).

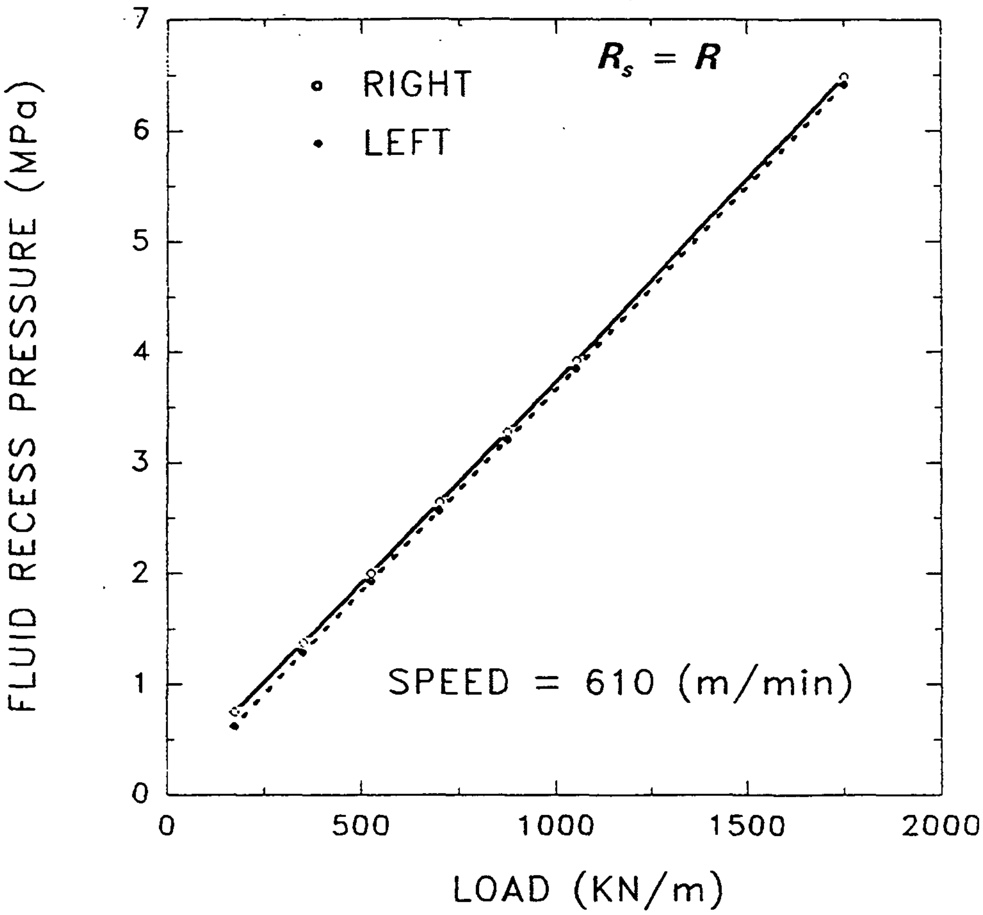

Figure 51. Lubricant recess pressure at the left-hand and right-hand channels vs. load for a roll speed of 610 m/min ($R_s = R$).

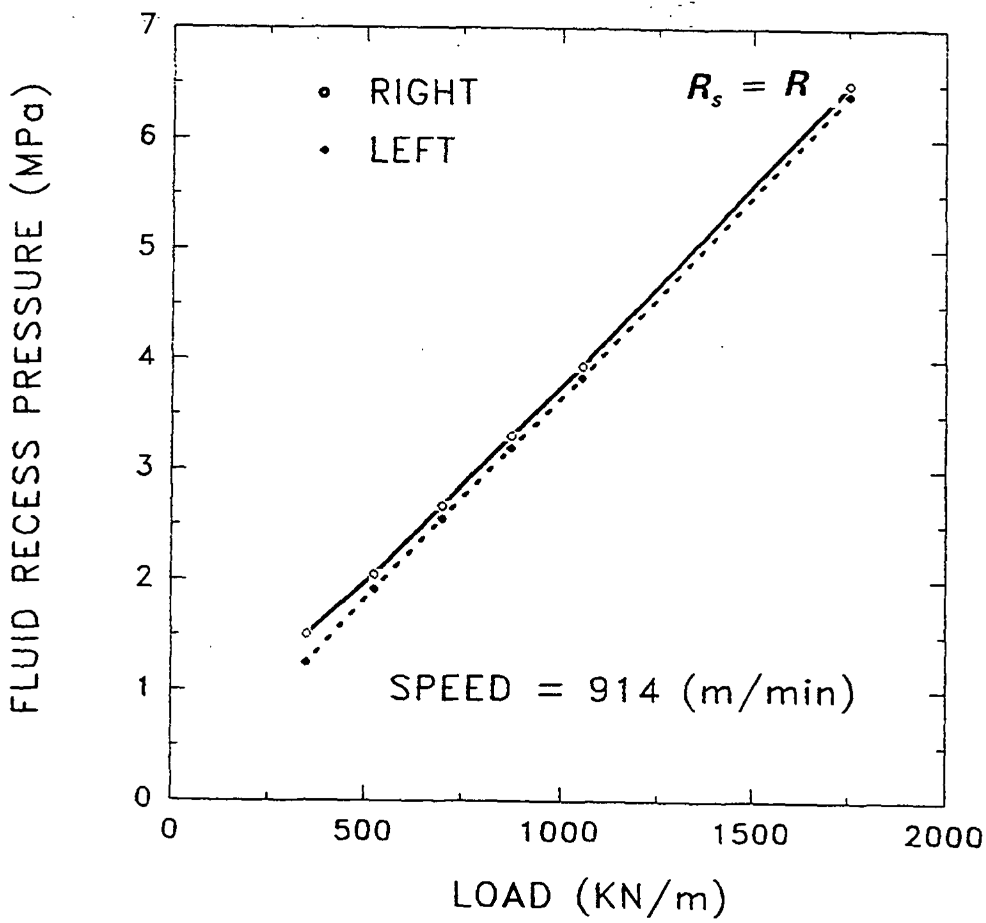

Figure 52. Lubricant recess pressure at the left-hand and right-hand channels vs. load for a roll speed of 914 m/min ($R_s = R$).

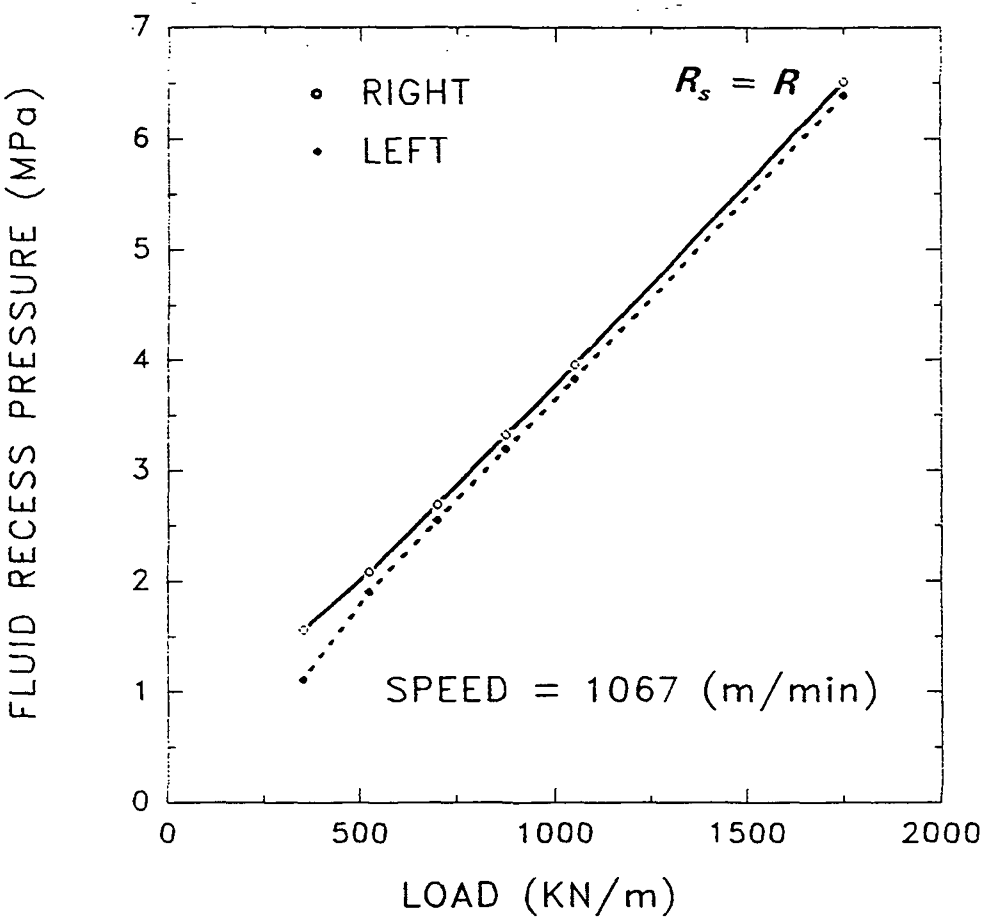

Figure 53. Lubricant recess pressure at the left-hand and right-hand channels vs. load for a roll speed of 1067 m/min ($R_s = R$).

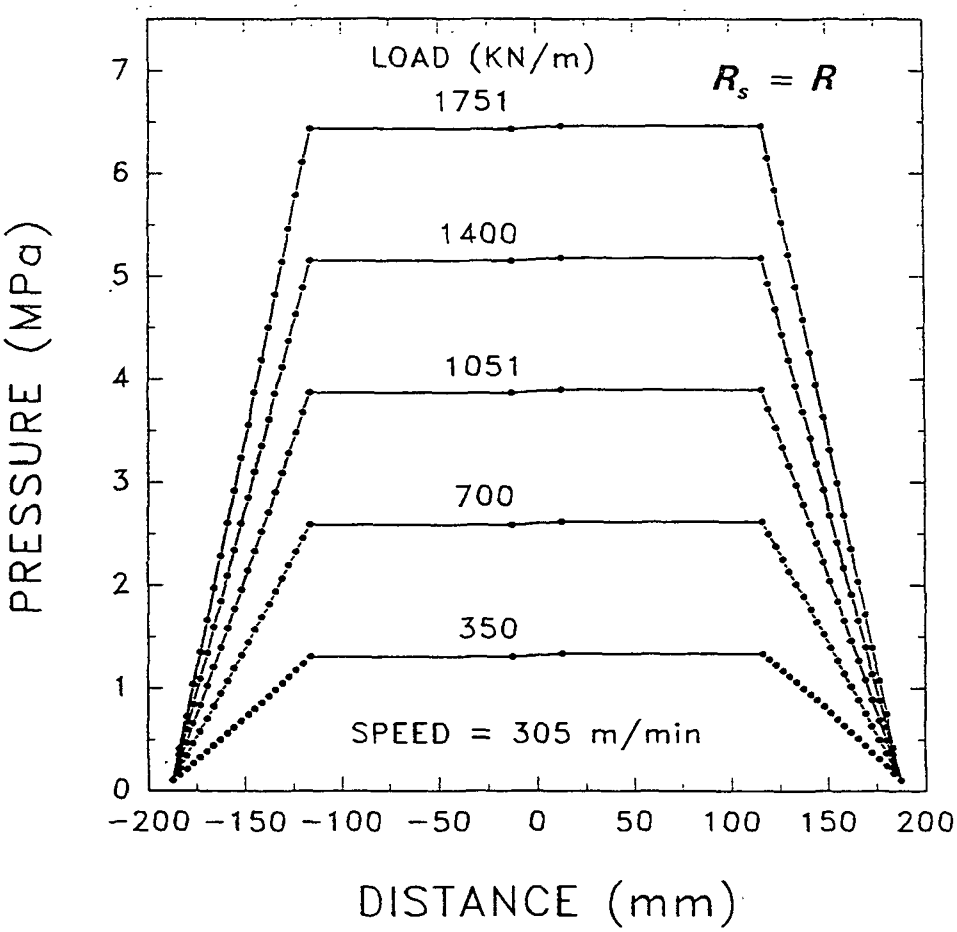

Figure 54. Lubricant pressure distribution along the length of both channels at a roll speed of 305 m/min ($R_s = R$).

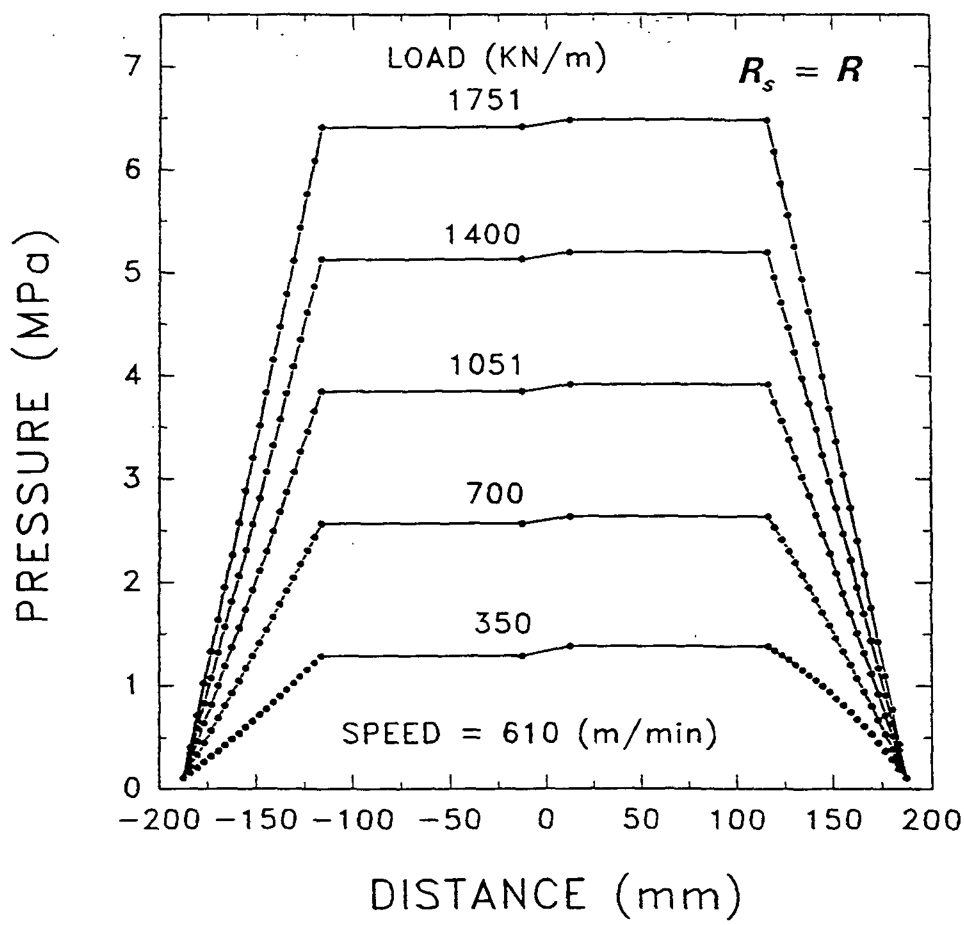

Figure 55. Lubricant pressure distribution along the length of both channels at a roll speed of 610 m/min ($R_s = R$).

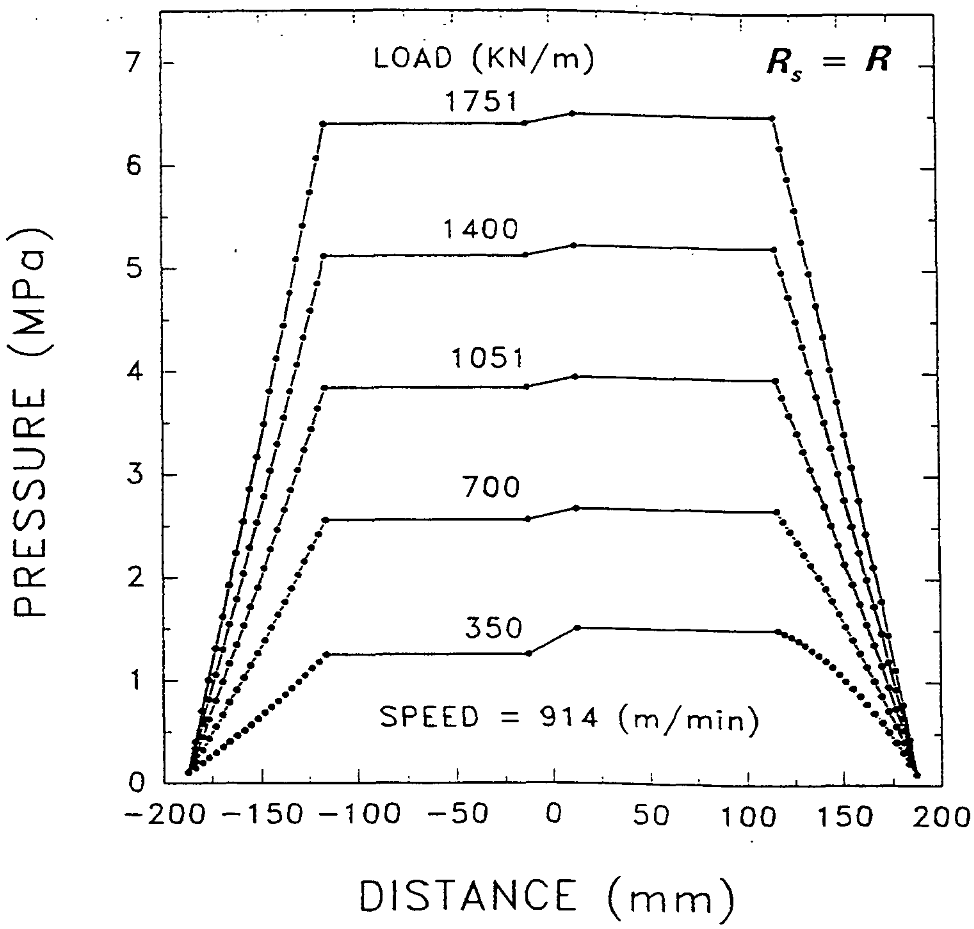

Figure 56. Lubricant pressure distribution along the length of both channels at a roll speed of 914 m/min ($R_s = R$).

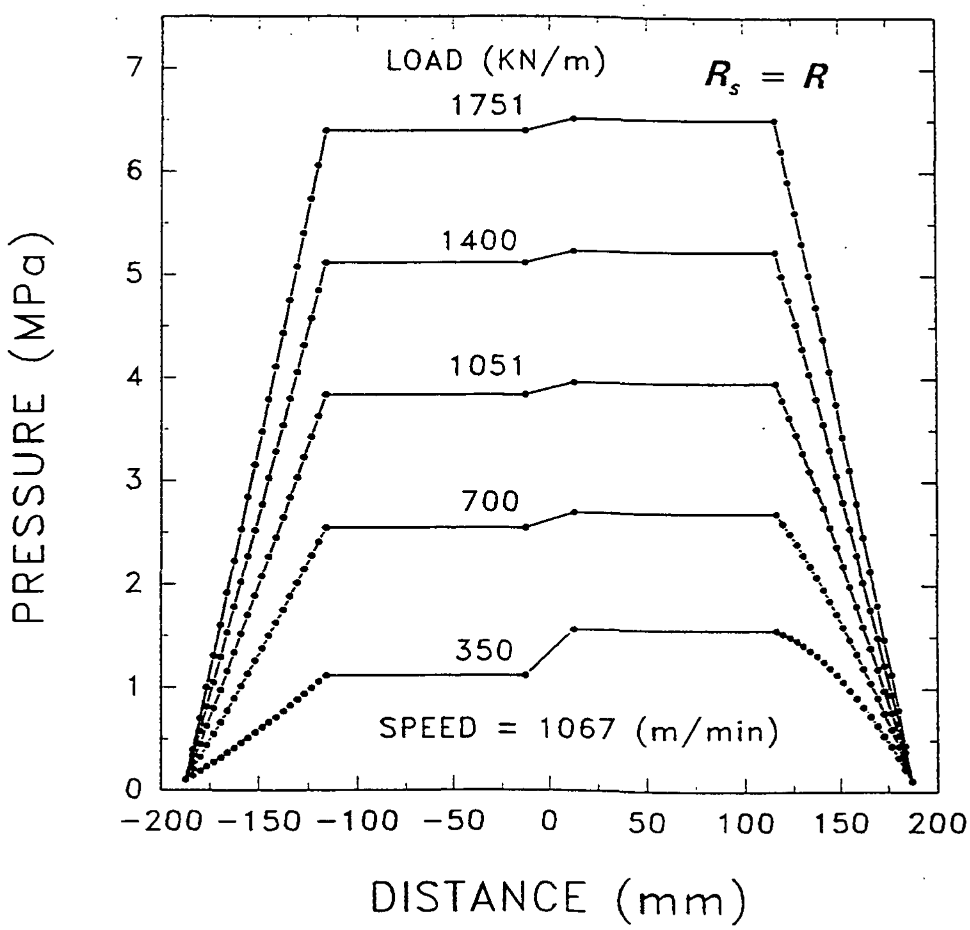

Figure 57. Lubricant pressure distribution along the length of both channels at a roll speed of 1067 m/min ($R_s = R$).

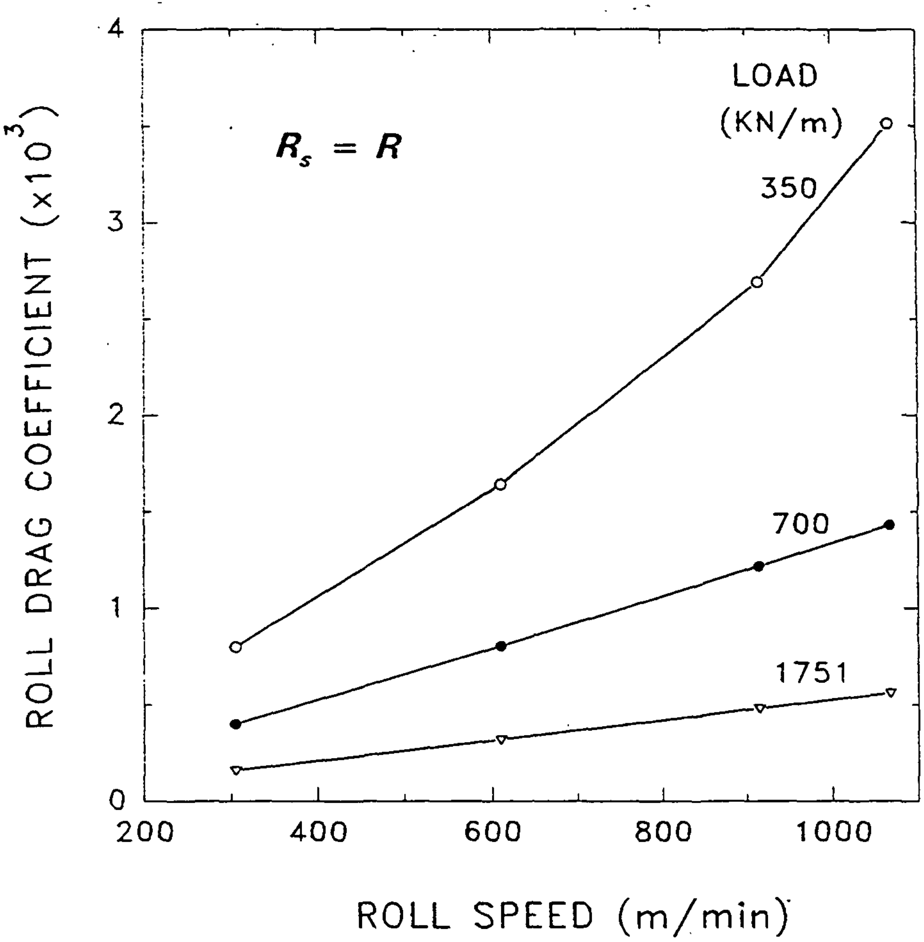

Figure 58. Roll drag coefficient vs. roll speed at each applied load ($R_s = R$).

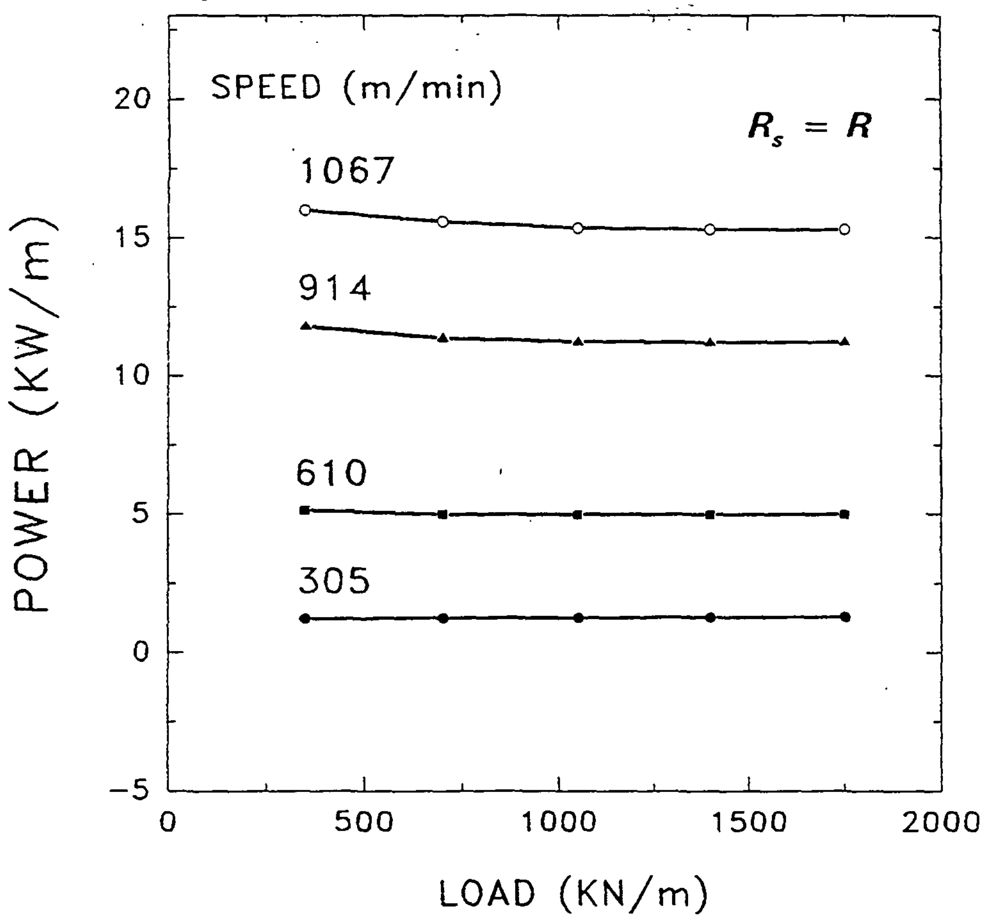

Figure 59. Mechanical power required to operate the roll vs. load for each roll speed ($R_s = R$).

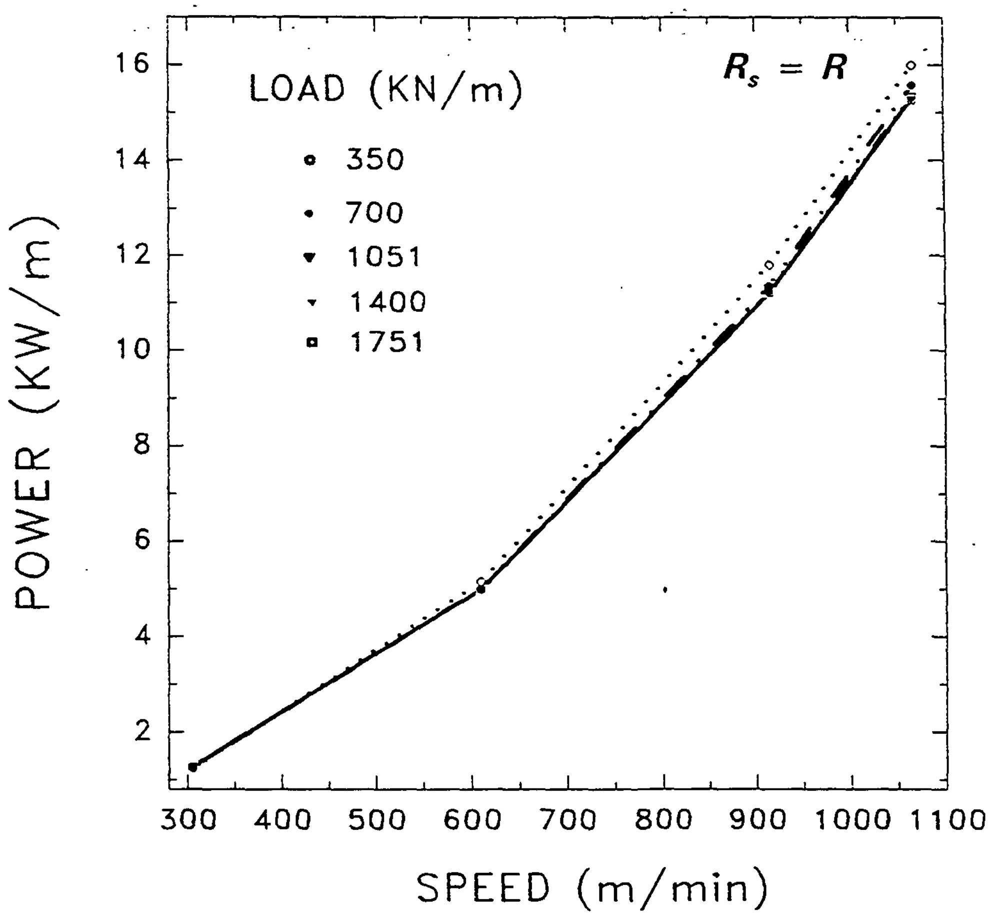

Figure 60. Mechanical power required to operate the roll vs. roll speed for each applied load ($R_s = R$).

APPENDIX IV: TABLES

TABLE 1 - Input values of the roll speed and applied load used in the computations for the small ($R_s \neq R$) and large ($R_s = R$) roll/shoe configurations.

LOAD	**(PLI)**	200	400	600	800	1000	2000	3000	4000	5000	6000	8000	10,000
	(KN/m)	35	70	105	140	175	350	525	700	875	1051	1400	1751

SPEED	**(ft/min)**	1000	2000	3000	3500
	(m/min)	305	610	914	1067

TABLE 2 - Predicted lubrication base thickness (d_o, mm) and angle of rotation (ψ, Deg) as a function of roll speed and applied load for the small roll/shoe configuration ($R_s \neq R$).

LOAD F (KN/m) ⇒	**35**		**70**		**105**		**140**		**175**	
SPEED s (m/min)	d_o	ψ	d_o	ψ	d_o	ψ	d_o	ψ	d_o	ψ
305	0.230	0.793	0.189	0.674	0.174	0.629	0.167	0.605	0.163	0.589
610	.285	0.952	0.227	0.785	0.202	0.713	0.188	0.673	0.180	0.647
914	.322	1.06	0.257	0.871	0.226	0.782	0.208	0.730	0.197	0.696

TABLE 3a - Predicted thicknesses of the leading edge ($d^L_{l\beta}$, mm) and trailing edge ($d^R_{l\beta}$, mm) as a function of roll speed and applied load for the small roll/shoe configuration ($R_s \neq R$).

LOAD F (KN/m) ⇒	35		70		105		140		175	
SPEED s (m/min)	$d^L_{l\beta}$	$d^R_{l\beta}$	$d^L_{l\beta}$	$d^R_{l\beta}$	$d^L_{l\beta}$	$d^R_{l\beta}$	$d^L_{l\beta}$	$d^R_{l\beta}$	$d^L_{l\beta}$	$d^R_{l\beta}$
305	0.439	0.021	0.358	0.020	0.328	0.019	0.313	0.019	0.303	0.019
610	0.548	0.022	0.434	0.021	0.384	0.021	0.357	0.020	0.340	0.020
914	0.621	0.023	0.493	0.022	0.432	0.021	0.396	0.020	0.373	0.020

TABLE 3b - Measured thicknesses of the leading edge (L.E., mm) and trailing edge (T.E., mm) as a function of roll speed and applied load for the small roll/shoe configuration ($R_s \neq R$).

LOAD (KN/m) ⇒	35		70		105		140		175	
SPEED s (m/min)	L.E.	T.E.	L.E.	T.E.	L.E.	T.E.	L.E.	T.E.	L.E.	T.E
305	0.180	0.129	0.150	0.110	0.129	0.104	0.117	0.096	0.109	0.093
610	0.239	0.165	0.196	0.129	0.173	0.112	0.157	0.102	0.145	0.099
914	0.292	0.206	0.239	0.157	0.206	0.129	0.188	0.114	0.173	0.102

TABLE 4 - Lubricant mass flow rates in the left-hand ($\dot{m}_L$, Kg/min.m), and right-hand channels ($\dot{m}_R$, Kg/min.m) for the small roll/shoe configuration ($R_s \neq R$).

LOAD (KN/m) ⇒	35		70		105		140		175	
SPEED (m/min)	$\dot{m}_L$	$\dot{m}_R$	$\dot{m}_L$	$\dot{m}_R$	$\dot{m}_L$	$\dot{m}_R$	$\dot{m}_L$	$\dot{m}_R$	$\dot{m}_L$	$\dot{m}_R$
305	10.94	5.09	25.6	4.86	40.1	4.95	54.7	5.17	69.2	5.43
610	9.72	10.99	24.4	10.3	39.0	9.91	53.6	9.8	68.2	9.87
914	8.50	16.9	23.2	16.1	37.9	15.5	52.5	15.0	67.1	14.8

TABLE 5a - Predicted lubricant mass flow rates ($\dot{m}_T$, Kg/min.m), and total volumetric flow rates ($\dot{Q}_T$, lit/min) exiting from both channels for the small roll/shoe configuration ($R_s \neq R$).

LOAD (KN/m) ⇒	35		70		105		140		175	
SPEED (m/min)	$\dot{m}_T$	$\dot{Q}_T$	$\dot{m}_T$	$\dot{Q}_T$	$\dot{m}_T$	$\dot{Q}_T$	$\dot{m}_T$	$\dot{Q}_T$	$\dot{m}_T$	$\dot{Q}_T$
305	16.0	7.45	30.4	14.1	45.1	20.9	59.8	27.8	74.6	34.7
610	20.7	9.6	34.7	16.1	48.9	22.7	63.5	29.8	78.1	36.3
914	25.4	11.8	39.3	18.3	53.3	24.8	67.6	31.4	82.0	38.1

TABLE 5b - Measured total lubricant volumetric flow rates (Q_T, lit/min) exiting from both channels for small roll/shoe configuration ($R_s \neq R$).

F (KN/m) ⇒ s (m/min) ⇓	35	70	105	140	175
305	17.41	23.47	24.60	31.79	37.09
610	17.60	23.60	28.77	33.12	37.09
914	17.60	23.66	28.77	31.98	37.28

TABLE 6 - Fluid pressure at the recess of the left-hand ($\tilde{P}_L$, MPa) and right-hand ($\tilde{P}_R$, MPa) channels for the small roll/shoe configuration ($R_s \neq R$).

LOAD (KN/m) ⇒	35		70		105		140		175	
SPEED (m/min)	$\tilde{P}_L$	$\tilde{P}_R$	$\tilde{P}_L$	$\tilde{P}_R$	$\tilde{P}_L$	$\tilde{P}_R$	$\tilde{P}_L$	$\tilde{P}_R$	$\tilde{P}_R$	$\tilde{P}_L$
305	0.35	0.53	0.59	1.23	0.83	1.92	1.07	2.61	1.31	3.29
610	0.36	0.35	0.62	1.06	0.86	1.77	1.1	2.46	1.34	3.15
914	0.43	0.17	0.66	0.88	0.90	1.59	1.14	2.30	1.37	3.0

TABLE 7 - Roll drag coefficient ($CD_{sl}*10^3$) as a function of roll speed and applied load for the small roll/shoe configuration ($R_s \neq R$).

F (KN/m) ⇒ s (m/min) ⇓	35	70	105	140	175
305	4.76	4.43	4.11	3.90	3.75
610	5.64	5.24	4.93	4.64	4.42
914	5.99	5.66	5.41	5.13	4.92

TABLE 8 - Calculated (calc.) and measured (meas.) mechanical power (KW/m) required to operate the press roll for the small ($R_s \neq R$) roll/shoe configuration.

LOAD (KN/m) ⇒	35		70		105		140		175	
SPEED (m/min)	calc.	meas.	calc.	meas.	calc.	meas.	calc.	meas.	calc.	meas.
305	0.76	0.94	1.38	1.0	1.91	1.06	2.41	1.06	2.88	1.17
610	1.62	2.35	3.29	2.85	4.58	2.97	5.73	3.20	6.78	3.67
914	2.14	4.27	5.23	4.43	7.54	5.14	9.51	5.49	11.30	6.58

TABLE 9 - Predicted lubrication base thickness (d_o, mm) and angle of rotation (ψ, Deg) as a function of roll speed and applied load for the large roll/shoe configuration (R_s=R).

LOAD F (KN/m) ⇒	**350**		**700**		**1051**		**1400**		**1751**	
SPEED s (m/min)	d_o	ψ	d_o	ψ	d_o	ψ	d_o	ψ	d_o	ψ
305	0.467	0.088	0.466	0.067	0.465	0.061	0.465	0.057	0.465	0.055
610	0.466	0.129	0.466	0.087	0.465	0.074	0.465	0.067	0.465	0.063
914	0.466	0.128	0.465	0.107	0.465	0.087	0.465	0.077	0.465	0.071
1067	0.483	0.208	0.465	0.117	0.465	0.094	0.465	0.082	0.465	0.075

TABLE 10 - Predicted thicknesses of the leading edge ($d^L_{1\beta}$, mm) and trailing edge ($d^R_{1\beta}$, mm) as a function of roll speed and applied load for the large roll/shoe configuration (R_s=R).

LOAD F (KN/m) ⇒	350		700		1051		1400		1751	
SPEED s (m/min)	$d^L_{1\beta}$	$d^R_{1\beta}$	$d^L_{1\beta}$	$d^R_{1\beta}$	$d^L_{1\beta}$	$d^R_{1\beta}$	$d^L_{1\beta}$	$d^R_{1\beta}$	$d^L_{1\beta}$	$d^R_{1\beta}$
305	0.518	0.416	0.491	0.441	0.482	0.449	0.477	0.453	0.475	0.456
610	0.569	0.365	0.515	0.416	0.498	0.432	0.489	0.440	0.484	0.445
914	0.623	0.305	0.540	0.391	0.514	0.416	0.502	0.428	0.494	0.435
1067	0.683	0.283	0.552	0.378	0.523	0.407	0.508	0.422	0.499	0.431

TABLE 11 - Lubricant mass flow rates in the left-hand ($\dot{m}_L$, Kg/min.m), and right-hand channels ($\dot{m}_R$, Kg/min.m) for the large roll/shoe configuration (R_s=ℝ).

LOAD (KN/m) ⇒	350		700		1051		1400		1751	
SPEED (m/min)	$\dot{m}_L$	$\dot{m}_R$	$\dot{m}_L$	$\dot{m}_R$	$\dot{m}_L$	$\dot{m}_R$	$\dot{m}_L$	$\dot{m}_R$	$\dot{m}_L$	$\dot{m}_R$
305	138	133	279	275	420	416	561	557	702	698
610	140	128	281	272	422	413	563	554	704	695
914	146	110	283	267	424	410	565	551	706	692
1067	164	104	285	264	425	408	566	549	707	691

TABLE 12 - Predicted lubricant mass flow rates ($\dot{m}_T$, Kg/min.m), and total volumetric flow rates ($\dot{Q}_T$, lit/min) exiting from both channels for the large roll/shoe configuration (R_s=R).

LOAD (KN/m) ⇒	350		700		1051		1400		1751	
SPEED (m/min)	$\dot{m}_T$	$\dot{Q}_T$	$\dot{m}_T$	$\dot{Q}_T$	$\dot{m}_T$	$\dot{Q}_T$	$\dot{m}_T$	$\dot{Q}_T$	$\dot{m}_T$	$\dot{Q}_T$
305	272	625	554	1275	836	1924	1118	2573	1400	3222
610	268	618	553	1273	835	1923	1117	2572	1117	2572
914	256	589	551	1267	834	1920	1117	2570	1399	3220
1067	269	618	549	1263	833	1918	1116	2569	1398	3219

TABLE 13 - Fluid pressure at the recess of the left-hand ($\tilde{P}_L$, MPa) and right-hand ($\tilde{P}_R$, MPa) channels for the large roll/shoe configuration (R_s=R).

LOAD (KN/m) ⇒	350		700		1051		1400		1751	
SPEED (m/min)	$\tilde{P}_L$	$\tilde{P}_R$	$\tilde{P}_L$	$\tilde{P}_R$	$\tilde{P}_L$	$\tilde{P}_R$	$\tilde{P}_L$	$\tilde{P}_R$	$\tilde{P}_L$	$\tilde{P}_R$
305	1.30	1.34	2.58	2.62	3.87	3.90	5.15	5.18	6.42	6.46
610	1.29	1.38	2.57	2.64	3.85	3.92	5.13	5.20	6.41	6.48
914	1.25	1.51	2.55	2.67	3.84	3.94	5.12	5.22	6.40	6.50
1067	1.11	1.56	2.55	2.69	3.83	3.96	5.13	5.23	6.39	6.51

TABLE 14 - Roll drag coefficient ($CD_{sl}*10^3$) as a function of roll speed and applied load for large roll/shoe configuration (R_s=R).

F (KN/m) ⇒ s (m/min) ⇓	350	700	1051	1400	1751
305	0.80	0.40	0.27	0.20	0.16
610	1.64	0.80	0.53	0.40	0.32
914	2.69	1.21	0.80	0.60	0.48
1067	3.51	1.43	0.94	0.70	0.56

TABLE 15- Predicted mechanical power (KW/m) required to operate the press roll for the large roll/shoe configuration (R_s=R).

F (KN/m) ⇒ s (m/min) ⇓	350	700	1051	1400	1751
305	1.23	1.24	1.24	1.26	1.26
610	5.14	4.99	4.98	4.98	4.98
914	11.8	11.4	11.2	11.2	11.2
1067	16.0	15.6	15.4	15.3	15.3

APPENDIX V: COMPARISON WITH THE EXPERIMENTAL DATA BASED ON RECENT INFORMATION PROVIDED BY BELOIT CORPORATION

In this appendix, we present some results that were obtained by using updated information provided by the Beloit Corporation during a meeting on August 4, 1994; this information involves more accurate dimensions, for the small shoe-roll configuration, than those that were available for most of the period during which the work on this report was in progress. The major changes include increasing the inner roll radius from its previous value of 6.750" to that of 6.760" and decreasing the angle ϕ (one-half the angular opening of the shoe) from its previous value of slightly more than 28° to 24°; the first change results from updated information from the Beloit Corporation regarding the actual radius of the shoe that was used in those experiments which have been used in this report, for the purposes of testing the numerical model, while the second change results from Beloit's [7] suggestions that as far as the hydrodynamic modeling goes, one should essentially ignore those regions in the channel which lie beneath the severely tapered ends of the shoe. We have also included now what appears to be the minor influence of the spring-like seals which are located along the shaft of the internal shoe. In general our results for the various speeds and loads that were tested are now much closer in terms of absolute magnitudes to the experimental data provided by Beloit. Whatever differences remain in magnitudes may be attributed to a multitude of factors: the simplified manner in which the portion of the channel under the tapered ends of the shoe is now being treated, the secant line approximations used for the arcs describing the bottom surfaces of the shoe and the roll, the fact that the oil which exits the channel on the right is not skimmed off but, rather, re-enters the channel on the left, the fact that all machine dimensions including the dimensions, of both the shoe and roll radii, are accurate only to within 0.002" (thus meaning that what is an extremely critical parameter in this model, namely, the difference between the roll radius and the shoe radius might be off by as much as 0.004"), and the fact that all of the results presented are based on assuming a constant oil viscosity (the viscosity at the lubricant inlet temperature). Because of viscous dissipation, at higher loads and speeds the average temperature in the oil will be higher than it is at lower speeds and loads, and at any fixed speed and load the temperature in the oil varies (spatially) throughout the lubrication channel; it is also known that the actual viscosity μ of the lubricant varies strongly with temperature, with viscosity decreasing as temperature increases. It is thus somewhat misleading to use the same viscosity when, e.g., we compare the predictions of the model at a roll speed of 1000 ft/min and loads of 1000 PLI and 800 PLI with the experimental data generated by Beloit because the viscosity will no longer be the same number in both cases. In fact, because of thermal expansion of the metal in both the roll and the shoe, it is even conceivable that neither the roll radius nor the shoe radius remains constant. Some of these difficulties will be resolved once a temperature dependent viscosity has been introduced into the model. Finally we note that the mathematical/numerical model appears to be very sensitive to changes in some measure of the relative difference $(R-R_s)/R$ where R is the roll radius and R_s is the shoe radius. The model is, also, at the same time, sensitive to some measure of the discrepancy between roll speed and load in the sense that branching of equilibrium solutions occurs, and multiple solutions appear, at relatively low loads and high speeds; this instability appears to be exacerbated by increasing this measure of the relative difference $(R-R_s)/R$. For the large "roll-shoe" configuration, where $R=R_s$, the model is very stable with respect to initial guesses, and for many operating conditions produces unique solutions (except at the lowest load and highest speed scenarios). The other extreme consist of the "small" roll-shoe configuration treated here where the ratio of $(R-R_s)/R$ is presumably large and multiple equilibrium solutions appear even in the high load cases with the situation becoming worse at higher speeds of the roll. The matter of the sensitivity of the numerical scheme to variations in some appropriate measure of $(R-R_s)/R$, and the concurrent impact on quantities of interest, i.e., lubrication thickness, horsepower, and mass flow rates, is a subject for another investigation.

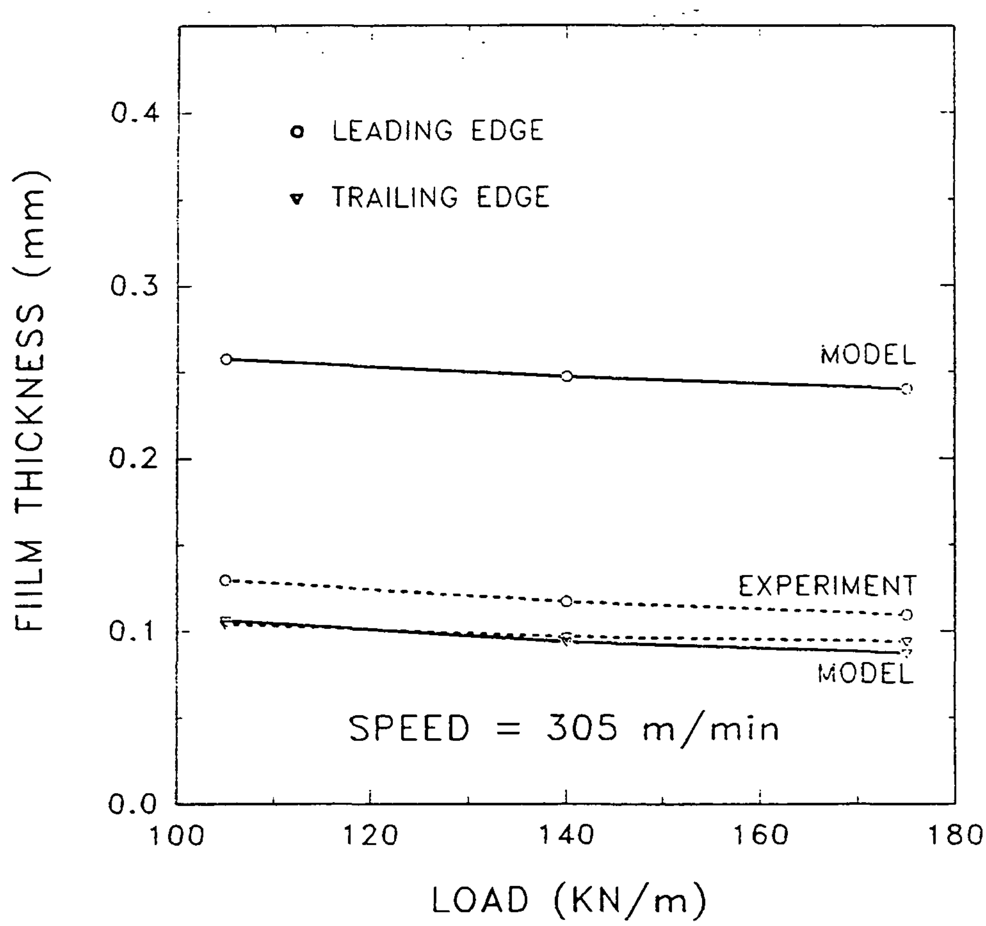

Figure A1 - Comparison between the lubricant film thicknesses at the leading edge ($d^L_{l\beta}$, mm), and trailing edge ($d^R_{l\beta}$, mm) predicted by the IPST model and measured by Beloit Corporation at a roll speed of 305 m/min for the small roll/shoe configuration ($R_s \neq R$).

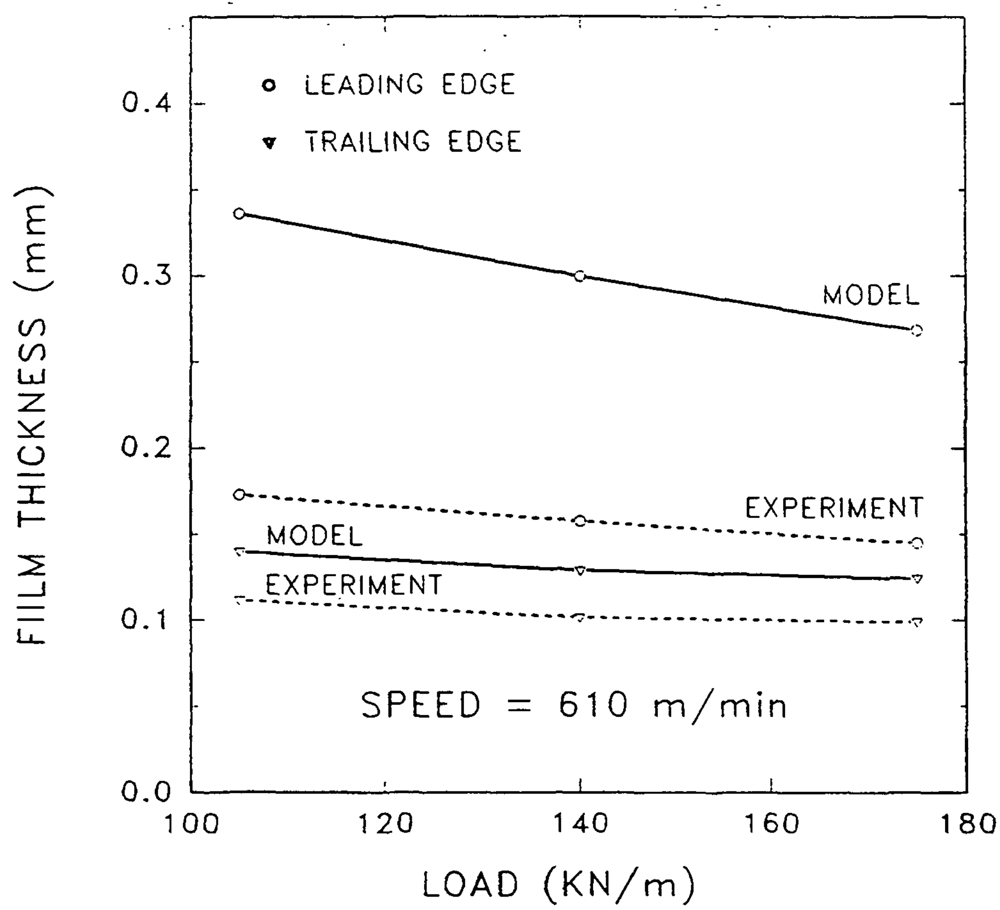

Figure A2 - Comparison between the lubricant film thicknesses at the leading edge ($d^L_{l\beta}$, mm), and trailing edge ($d^R_{l\beta}$, mm) predicted by the IPST model and measured by Beloit Corporation at a roll speed of 610 m/min for the small roll/shoe configuration ($R_s \neq R$).

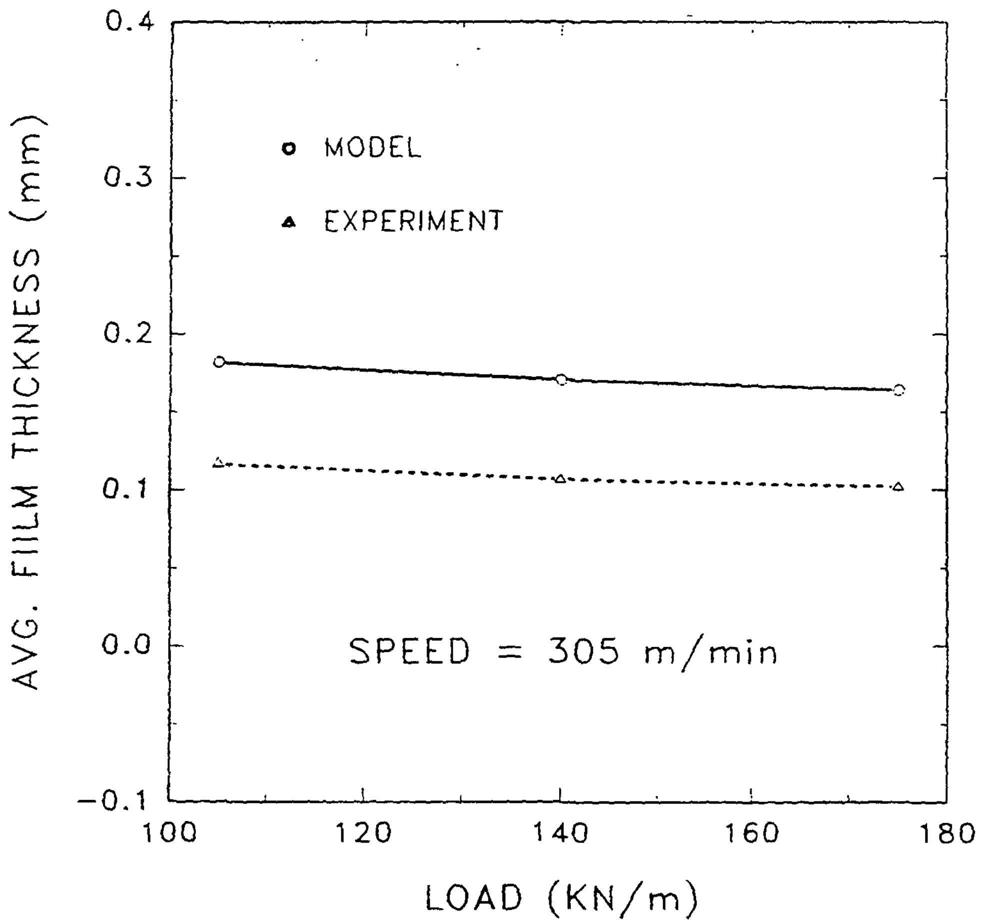

Figure A3 - Comparison between the average lubricant film thicknesses (mm) predicted by the IPST model and measured by Beloit Corporation at a roll speed of 305 m/min for the small roll/shoe configuration ($R_s \neq R$).

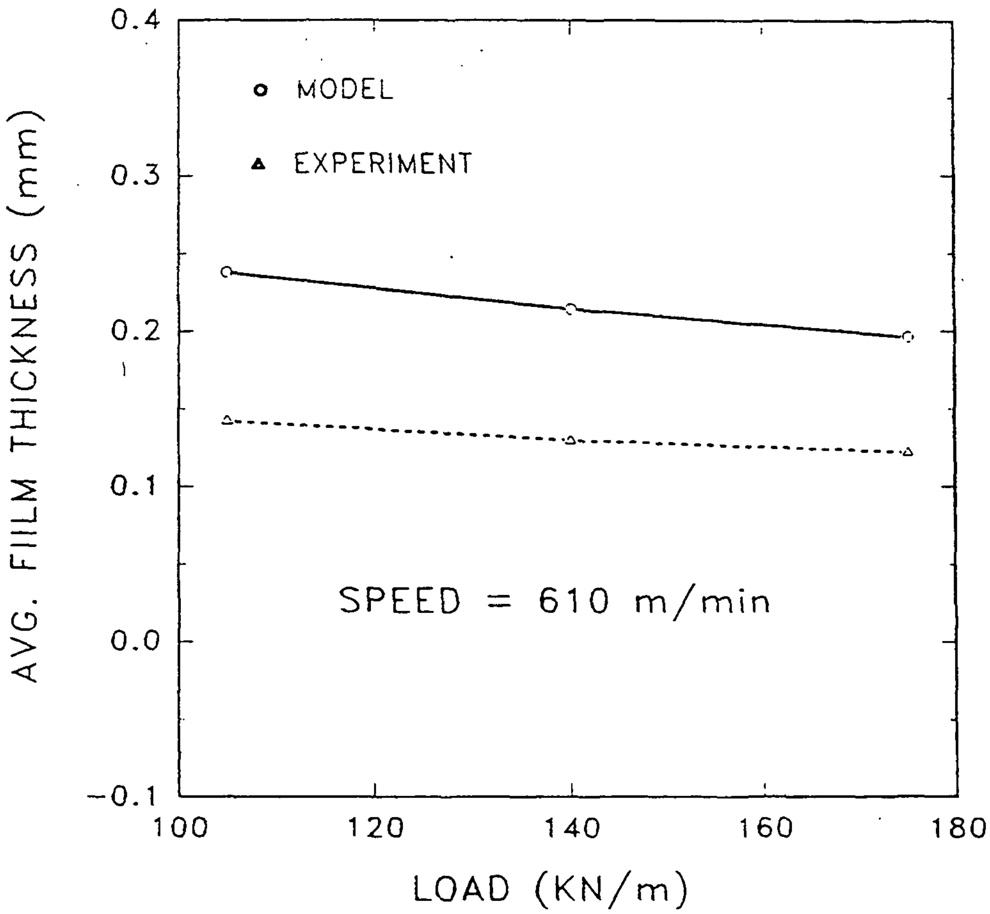

Figure A4 - Comparison between the average lubricant film thicknesses (mm) predicted by the IPST model and measured by Beloit Corporation at a roll speed of 610 m/min for the small roll/shoe configuration ($R_s \neq R$).

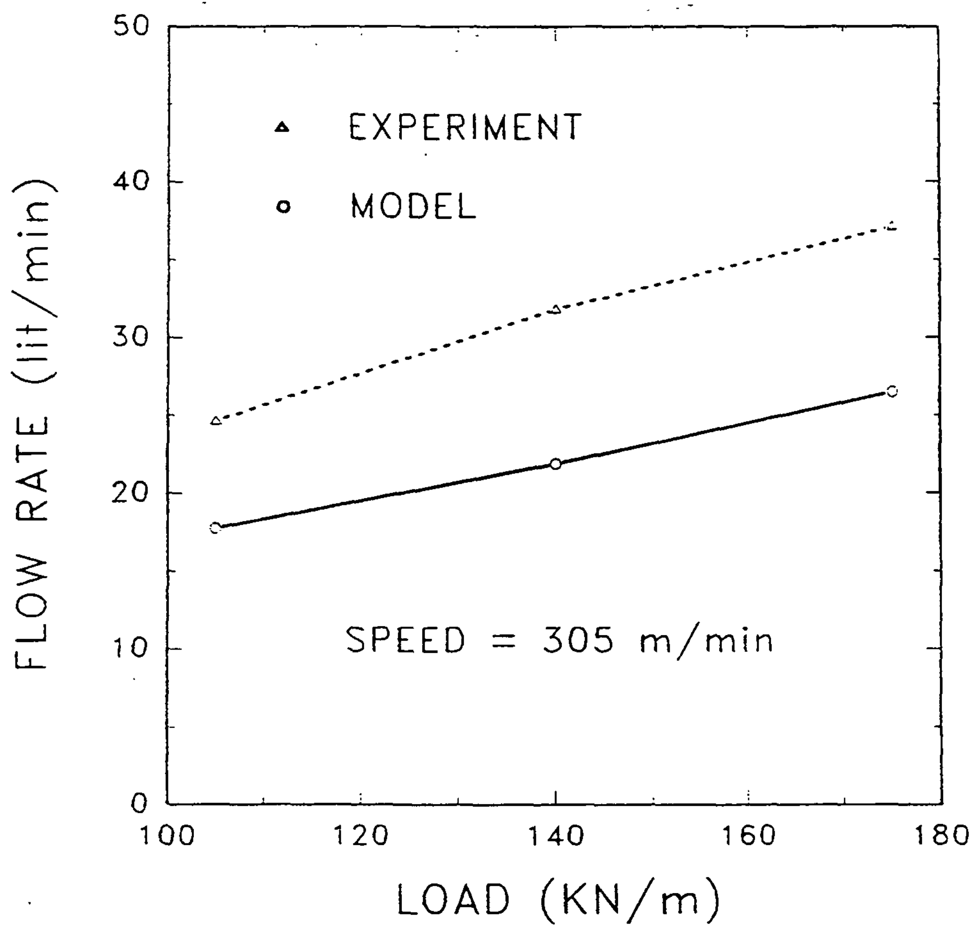

Figure A5 - Comparison between the volumetric flow rate predicted by the IPST model and by Beloit Corporation at a roll speed of 305 m/min for the small roll/shoe configuration ($R_s \neq R$).

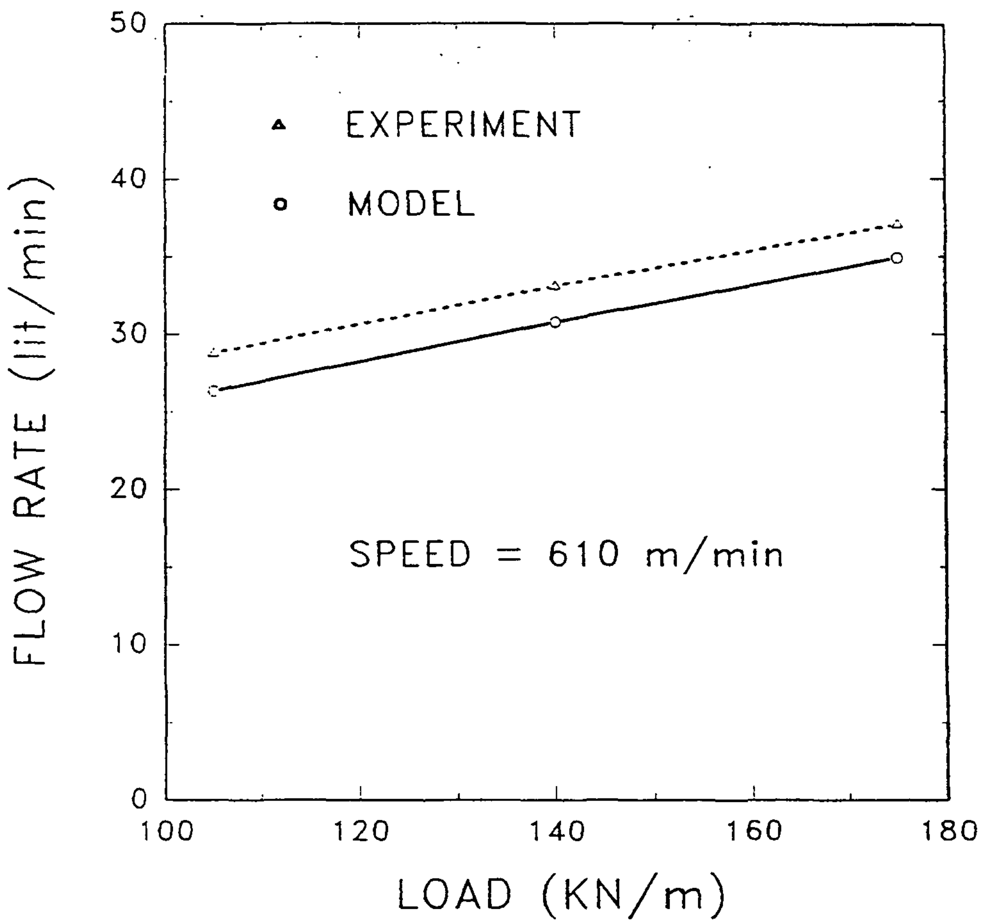

Figure A6 - Comparison between the volumetric flow rate predicted by the IPST model and measured by Beloit at a roll speed of 610 m/min for the small roll/shoe configuration ($R_s \neq R$).

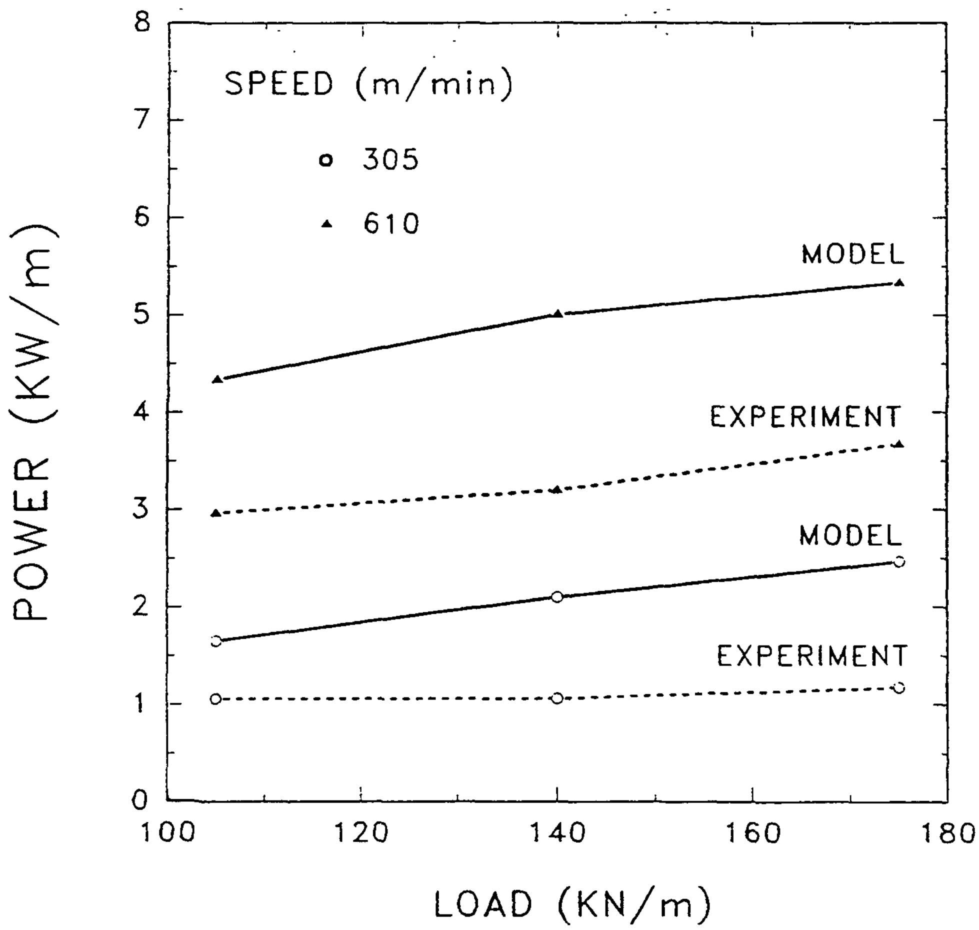

Figure A7 - Comparison between the power predicted by the IPST model and measured by Beloit at a roll speeds of 305 m/min and 610 m/min for the small roll/shoe configuration ($R_s \neq R$).

TABLE A1 - Predicted values of the leading edge thickness ($d^L_{l\beta}$), trailing edge thickness ($d^R_{l\beta}$), angle of rotation (ψ), and mass flow rates in each channel ($\dot{m}_L$, $\dot{m}_R$) at a roll speed of 305 m/min, as a function of applied load for the small roll/shoe configuration ($R_s \neq R$).

LOAD F (KN/m)	$d^L_{l\beta}$ (mm)	$d^R_{l\beta}$ (mm)	ψ (Deg)	$\dot{m}_L$ (Kg/m.min)	$\dot{m}_R$ (Kg/m.min)
105	0.257	0.106	0.391	24.65	9.46
140	0.247	0.094	0.394	34.67	7.34
175	0.240	0.087	0.393	44.43	6.41

TABLE A2 - Predicted values of the total mass flow rate ($\dot{m}_T$), total volumetric flow rate ($\mathring{Q}_T$), left recess pressure ($\tilde{P}_L$), right recess pressure ($\tilde{P}_R$), and mechanical power at a roll speed of 305 m/min, as a function of applied load for the small roll/shoe configuration ($R_s \neq R$).

LOAD F (KN/m)	$\dot{m}_T$ (Kg/m.min)	$\mathring{Q}_T$ (lit/min)	$\tilde{P}_L$ (MPa)	$\tilde{P}_R$ (MPa)	POWER (KW/m)
105	34.1	17.7	1.1	1.7	1.65
140	42.0	21.9	1.3	2.5	2.10
175	50.8	26.5	1.6	3.2	2.46

TABLE A3 - Predicted values of the leading edge thickness ($d^{L}_{1\beta}$), trailing edge thickness ($d^{R}_{1\beta}$), angle of rotation (ψ), and mass flow rates in each channel ($\dot{m}_L$, $\dot{m}_R$) at a roll speed of 610 m/min, as a function of applied load for the small roll/shoe configuration ($R_s \neq R$).

LOAD F (KN/m)	$d^{L}_{1\beta}$ (mm)	$d^{R}_{1\beta}$ (mm)	ψ (Deg)	$\dot{m}_L$ (Kg/m.min)	$\dot{m}_R$ (Kg/m.min)
105	0.336	0.140	0.453	27.42	23.20
140	0.300	0.129	0.415	35.84	23.35
175	0.268	0.124	0.381	41.46	25.60

TABLE A4 - Predicted values of the total mass flow rate ($\dot{m}_T$), total volumetric flow rate ($\dot{Q}_T$), left recess pressure ($\tilde{P}_L$), right recess pressure ($\tilde{P}_R$), and mechanical power at a roll speed of 610 m/min, as a function of applied load for the small roll/shoe configuration ($R_s \neq R$).

LOAD F (KN/m)	$\dot{m}_T$ (Kg/m.min)	$\dot{Q}_T$ (lit/min)	$\tilde{P}_L$ (MPa)	$\tilde{P}_R$ (MPa)	POWER (KW/m)
105	50.6	26.3	0.94	1.1	4.35
140	59.2	30.8	1.28	1.8	5.01
175	67.1	34.9	1.74	2.3	5.33

TABLE A5 - Measured values of the leading edge thickness ($d^{L}_{1\beta}$), trailing edge thickness ($d^{R}_{1\beta}$), total mass flow rates ($\dot{m}_{L}$), total volumetric flow rate ($\dot{Q}_{R}$), and mechanical power at a nominal roll speed of 305 m/min, as a function of applied load for the small roll/shoe configuration ($R_s \neq R$).

LOAD F (KN/m)	$d^{L}_{1\beta}$ (mm)	$d^{R}_{1\beta}$ (mm)	$\dot{m}_{T}$ (Kg/m.min)	$\dot{Q}_{T}$ (lit/min)	POWER (KW/m)
105	0.129	0.104	47.2	24.6	1.06
140	0.117	0.096	60.9	31.8	1.06
175	0.109	0.093	71.0	37.1	1.17

TABLE A6 - Measured values of the leading edge thickness ($d^{L}_{1\beta}$), trailing edge thickness ($d^{R}_{1\beta}$), total mass flow rates ($\dot{m}_{L}$), total volume flow rate ($\dot{Q}_{R}$), and mechanical power at a nominal roll speed of 610 m/min, as a function of applied load for the small roll/shoe configuration ($R_s \neq R$).

LOAD F (KN/m)	$d^{L}_{1\beta}$ (mm)	$d^{R}_{1\beta}$ (mm)	$\dot{m}_{T}$ (Kg/m.min)	$\dot{Q}_{T}$ (lit/min)	POWER (KW/m)
105	0.173	0.112	55.2	28.8	2.97
140	0.157	0.102	63.5	33.1	3.20
175	0.145	0.099	71.2	37.1	3.67